

CONTENTS

Declaration	ii
Dedication	iii
Acknowledgments	iv
Abstract	v
1. Introduction	1
1.1. Background	3
1.2. Thesis statement and research objectives	8
1.3. Approximations and limitations	10
1.4. Definitions of technical terms and abbreviations	14
1.5. Significance	16
2. Literature review	18
2.1. A brief account of metallic nanocontacts and scalar-relativistic effects	18
2.2. An account of domain-wall magnetoresistance in Ni and Fe nanocontacts	23
3. Overview of standard methods	38
3.1. Classical molecular dynamics	39
3.1.1. <i>The embedded-atom method potentials</i>	41
3.1.2. <i>Magnetic potentials</i>	43
3.2. Spin-lattice dynamics	46
3.3. Density functional theory	51
3.4. Non-equilibrium Green's Function DFT quantum transport	57
4. Extensions of standard methods and preliminary computational results	63
4.1. Emulating the experiments: cyclic loading	63
4.2. Spin-lattice dynamics with spin-orbit coupling	67
4.2.1. <i>Uniaxial magnetic anisotropy</i>	67

4.2.2. <i>Spin-lattice dynamics of ferromagnetic nanocontacts</i>	75
4.3. Vector-relativistic NEGF quantum transport	76
4.3.1. <i>Spin-orbit coupling in quantum transport</i>	78
4.3.2. <i>Non-collinear magnetism in quantum transport</i>	87
5. Relativistic effects in non-magnetic metal nanocontacts: Au, Cu and Ag	93
5.1. Classical molecular dynamics of Au, Ag and Cu nanocontacts	94
5.1.1. <i>In-contact structures and the role of the nearest neighbours</i>	95
5.1.2. <i>Scalar-relativistic quantum transport of CMD snapshots</i>	101
5.2. The role of scalar-relativistic effects in Au	104
5.2.1. <i>To what extent do CMD simulations get it right?</i>	105
5.2.2. <i>Relativistic plane-wave density functional theory</i>	106
5.2.3. <i>The effects of dispersion interactions and spin-orbit coupling</i>	110
6. The atomic configurations of Ni and Fe before rupture	113
6.1. Why theoretical conductance values for BCC Fe nanocontacts are so low	113
6.1.1. <i>CMD simulations of Fe nanocontacts: EAM vs MEAM</i>	115
6.1.2. <i>Scalar-relativistic quantum transport of Fe CMD snapshots</i>	117
6.2. Comparison with an FCC ferromagnetic metal: nickel	122
6.2.1. <i>CMD simulations of Ni nanocontacts: EAM vs MEAM</i>	123
6.2.2. <i>Scalar-relativistic quantum transport of Ni CMD snapshots</i>	127
7. The role of ferromagnetism and uniaxial magnetic anisotropy in Fe and Ni nanocontacts	129
7.1. Magnetic domain walls in (001)- and (111)-oriented Ni nanocontacts	130
7.1.1. <i>Cyclic loading of (001) Ni nanocontacts</i>	130
7.1.2. <i>Cyclic loading of (111) Ni nanocontacts</i>	132
7.1.3. <i>Vector-relativistic quantum transport of Ni SLD snapshots</i>	133
7.2. Magnetic domain walls in (001)-oriented Fe nanocontacts	136
7.2.1. <i>Cyclic loading of (001) Fe nanocontacts</i>	137
7.2.2. <i>Vector-relativistic quantum transport of Fe SLD snapshots</i>	138
8. Concluding remarks	140

1. INTRODUCTION

The quest for ever smaller transistors is an ongoing endeavour which today mainly focuses on simultaneously exploiting the electron's charge and spin, in an attempt to maximise information processing power via concrete realisations of spintronics [1]. However, the success of this venture is conditioned by the fact that, at the nanoscale, every atom and spin now counts. For this reason, understanding the physical behaviour of materials, right down to the nanoscale, is of significant technological importance, and the pursuit of such understanding, continues to pose new experimental and theoretical challenges.

Already in 1992, Professor Uzi Landman, who is famous for pioneering the field of emergent properties of materials at the nanoscale, showed through careful analysis [2], how measurable physical and chemical properties of various materials scale with size. Interestingly, he found that certain properties do not scale in a predictable manner all the way down to the nanometer-scale. That is, at the nanoscale, certain properties of materials depart from the usual scaling laws that apply to the macroscopic systems. Landman *et al.* [3] have continued their research into a growing number of nanoscale systems that exhibited emergent properties, including more recently, exotic systems that are related to the burgeoning field of molecular machines [4,5]. In fact, the 2016 Nobel Prize in Chemistry was awarded to Jean-Pierre Sauvage, Sir J. Fraser Stoddart, and Bernard L. Feringa “for the design and synthesis of molecular machines”¹.

From a practical standpoint, the non-scalability of measurable properties of *nanoscopic*² materials, poses serious challenges to the realisation of nanoscale devices for technological applications. Within this broader context, the research presented in this thesis is related to some specific questions that arise in connection with nanoscale electrical contacts between metals.

In the remainder of this chapter, I will provide some essential background information related to these *nanocontacts* (Sec 1.1), and also state which specific research questions I

¹ See <https://www.nobelprize.org/prizes/chemistry/2016/press-release/>

² For convenience, some technical terms and abbreviations used in this thesis are defined in Sec 1.4, and these terms are italicised upon first use.

have addressed (Sec 1.2). The scope of the work is outlined (Sec 1.3) and useful technical terms and abbreviations are defined (Sec 1.4). The significance of the work carried out towards this thesis is highlighted at the end of the chapter (Sec 1.5).

Chapter 2 discusses the relevant literature and is aimed to inform the reader about the context in which this work arises. First, the importance of relativistic effects in metallic nanocontacts is surveyed (Sec 2.1). Second, the effects of magnetic domain walls on the electrical resistance of ferromagnetic nanocontacts is discussed (Sec 2.2)

Chapter 3 is an overview of the standard theoretical methods employed to study the dynamic evolution of transition metal nanocontacts and calculate their transport properties. It provides a basic introduction to *classical molecular dynamics (CMD)* in Sec 3.1, *spin-lattice dynamics (SLD)* in Sec 3.2, *density functional theory (DFT)* in Sec 3.3 and, finally, *non-equilibrium Green's Function (NEGF)* quantum transport in Sec 3.4.

In Chapter 4 I describe some extensions which I have made to existing computational implementations of the methods that were introduced in the previous chapter. These modifications are aimed at improving the accuracy of existing methods for modelling ferromagnetic nanocontacts. In Sec 4.1, I describe how the dynamics of nanocontact evolution (making and breaking the contacts, or *cyclic loading*) was implemented in the model. The consequences of *spin-orbit coupling (SOC)* are then incorporated into SLD simulations through the *magnetocrystalline anisotropy energy (MAE)* in Sec 4.2. In the last section of the chapter (Sec 4.3), SOC and non-collinear magnetism are implemented in DFT quantum transport calculations.

Chapter 5 discusses the similarities and differences between gold, silver and copper nanocontacts immediately before and after contact formation. First, the role played by the first-neighbour atoms in contacts that are comprised of only a few atoms is explored (Sec 5.1.1). Then, in Sec 5.1.2, a comparison of DFT quantum transport and experimental results on few-atom gold nanocontacts provide a clue about the origin, i.e., relativistic effects, of the much stronger interaction between pure gold electrodes versus copper or silver ones, observed experimentally in the tunnelling regime. The influence of the relativistic effects is the subject of Sec 5.2, where the results of plane-wave DFT

calculations of the force-extension characteristics of monatomic gold and silver wires are presented.

Chapter 6 examines how directionality, or covalency, affects the bonding in Fe and Ni nanocontacts. A *modified embedded-atom method (MEAM)* potential is used to generate stable last-contact structures of *body-centred cubic (BCC)* Fe in CMD simulations (Sec 6.1.1). The MEAM potential adds covalency, or directionality, to the more widely-used *embedded-atom method (EAM)* potential model of bonding between the metal atoms in CMD simulations. The simulations are repeated with an EAM potential for comparison. Then, the conductance of the stable structures of Fe are calculated by DFT quantum transport in Sec 6.2.1 to compare with recent experimental results. In Sec 6.2.1, *face-centred cubic (FCC)* Ni nanocontacts are ruptured in two different crystallographic orientations, (001) and (111), in CMD simulations with a MEAM potential. Once more, the simulations are repeated with an EAM potential for comparison and the conductance of selected stable Ni last-contact structures are calculated in Sec 6.2.2.

Chapter 7 explores the role of non-collinear magnetic order in the constriction of ferromagnetic Ni and Fe nanocontacts. The results of SLD simulations of cyclic loading of (001)- and (111)-oriented Ni nanocontacts are presented in Sec 7.1.1, with the conductance of selected SLD snapshots at last contact reported in vector-relativistic DFT transport calculations in Sec 7.1.2. For comparison, results for cyclic loading of (001)-oriented Fe nanocontacts are presented in Sec 7.2.1. Vector-relativistic DFT transport calculations are also performed on last-contact structures from these simulations, and reported in Sec 7.2.2.

Chapter 8 concludes with a summary of all the results, a list of the codes used and future directions suggested for this work.

1.1. Background

Recent, groundbreaking work has shown that thermal transport is non-scalable at the atomic level: atomic-sized Au contacts were shown to transport heat in discrete quantised packets [6]. Previously, it had been known since the 1990s that charge transport is quantised in

atomic-sized contacts made of metals such as Au [7]. Initially, the quantised charge transport was attributed to conduction through discrete energy levels, i.e., waveguides, resulting from lateral confinement of electrons in the atomically narrow contacts [8]. However, the very first classical molecular dynamics (CMD) simulations of atomic-sized metallic contact formation, performed by Landman *et al.* in 1990 [9], suggested another explanation for the quantisation of charge transport in metallic nanocontacts. The grainy nature and geometry of atomic-sized contacts, in combination with the chemical valency of individual atoms within such contacts, should determine charge transport, when only a single or few atoms occupy the minimum cross-section of the contacts [10].

As experiments increasingly provide more details, and are able to quantify more properties, theoretical models must necessarily also become more accurate. Models must now take into account many more subtle quantum mechanical effects, such as, the effects of lattice motion on magnetism, and higher order relativistic corrections. The development of one such model, which can be applied not only to nanocontacts, but also to other systems, is the focus of this work.

Experimentally, extremely relevant and revealing information can be extracted about electrical contacts at the nanoscale, from methods that employ the *scanning tunnelling microscope (STM)* or the *mechanically controllable break junction (MCBJ)* technique [11]. Both these techniques permit the realisation of atomically sharp electrical contacts, as shown schematically in Fig. 1.1 below.

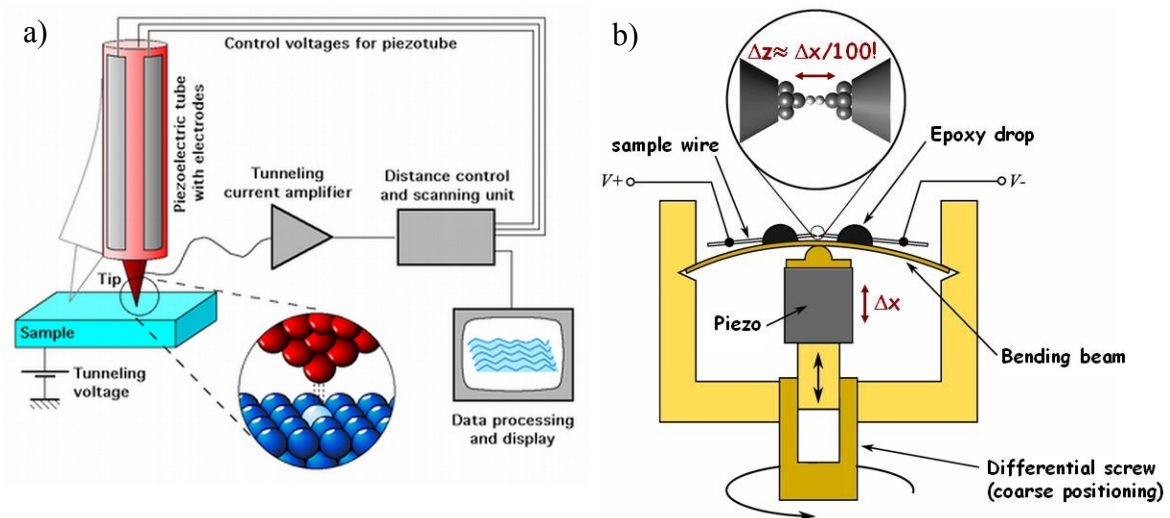


Fig. 1.1: a) Basic operating principle of a scanning tunnelling microscope³ and b) of a mechanically controllable break junction⁴. See main text for descriptions.

Figure 1.1 a) illustrates how a scanning tunnelling microscope functions. The zoom-in in the inset shows an atomically sharp metal tip (red) interacting with a sample surface (blue) below the tip. The tip can be moved, both horizontally and vertically relative to the sample surface, by tuning the voltage of the piezo actuator that is built into the tip housing. Only the STM tip moves as the piezo voltage is adjusted, while the sample surface remains stationary.

Figure 1.1 b) shows the setup in a MCBJ experiment. A metal wire (the sample) is attached to a bending beam by means of two epoxy resin droplets. The wire is very fine and a notch has been made in it, near its centre, to ensure that it ruptures in that spot. Rupture occurs when the degree of bending of the beam to which the wire is attached, is increased by the expansion of the piezo element, which is positioned directly beneath the beam. The piezo element expands upon increasing the voltage applied to the piezo actuator.

As in the case of the STM, the relative displacement between the ruptured ends of the wire is proportional to the applied piezo voltage, and the conductance can be recorded as a function of this displacement. The piezo voltage can also be tuned in such a way as to repeatedly establish and break off contact between the ruptured ends of the wire. This process is also known as cyclic loading and can be performed to sub-nanometer precision.

3 Source: Wikipedia. URL: https://en.wikipedia.org/wiki/Scanning_tunnelling_microscope#Instrumentation

4 Source: CINaM. URL: http://www.cinam.univ-mrs.fr/pro_perso/klein/index.php?page=fost

The MCBJ setup is far more stable than the STM described above. Although STM has a much greater freedom of movement, this freedom comes at the expense of stability.

Conductance traces are recorded in an STM or MCBJ experiment as a function of tip-sample or tip-tip separation, respectively. The relative displacement of the tip and sample (STM), or tip and tip (MCBJ), is proportional to applied piezo voltage [11]. It is important to keep in mind that, experimentally, conductance histograms (see Fig. 1.2 b) for an example) are usually constructed from hundreds or thousands of conductance traces, recorded during repeated cycles of formation and rupture of nanocontacts at a given location on a sample surface [12].

Through these methods the structural, electronic, thermal and magnetic properties of transition metal nanocontacts are routinely probed at the atomic scale, at very low temperatures (4.2 K) and under *ultra-high vacuum* ($< 10^{-7}$ Pa). In doing so, one encounters several manifestations of unexpected behaviour that “emerges” as the size of the system is reduced to the atomic level. These include phenomena such as:

- *Conductance* quantisation, or the variation of the conductance in a step-wise fashion when only a few atoms occupy the narrowest cross-section of the contact [7];
- Avalanche to adhesion, also known as “*jump to contact*” (*JC*), which is an abrupt jump in measured conductance when an atomic-sized contact is first formed (see the red trace in Fig. 1.2 a)) [13];
- Emergent magnetism in metals which are paramagnetic in the bulk, but become magnetic in low-coordination environments such as nancontacts, due to greater electron localisation on the atoms [14];
- *Ballistic magnetoresistance (BMR)*, or variations in measured conductance from the presence of magnetic domain walls in the nanocontacts [15,16];
- More recently, quantised thermal transport [6], in which heat transport across metal nanocontacts is quantised in discrete steps.

It is the interpretation of these experimental observations, and their underlying mechanisms at the nanoscale, which require more sophisticated modelling.

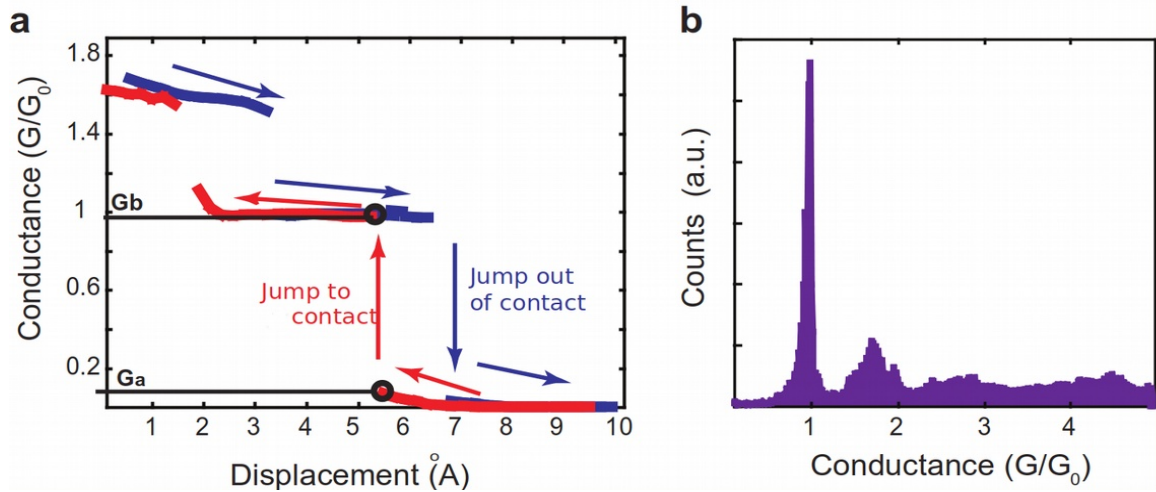


Fig. 1.2: a) Example of a conductance trace measured at 4.2 K in an STM experiment of contact formation between a gold tip and sample surface. As the tip approaches the sample (red trace, starting from the bottom right), the conductance increases exponentially until a jump to contact occurs, as the vertical red arrow shows. A second jump to a higher conductance occurs after that, but is due to an atomic rearrangement when contact has already been established. As the tip is withdrawn from the sample (blue trace, starting from the top left), the conductance decreases in a first jump, signalling once more an in-contact atomic rearrangement, followed by the moment of rupture, a jump out of contact, as the vertical blue arrow shows. Conductance values before and after contact are shown to the left of the figure. The conductance is here measured in units of $G_0 = 2e^2/h$, where e is the electron charge and h is Planck's constant. The conductance *before* contact is labelled G_a , and *after* G_b , respectively (the subscript "a" refers to initial here, and "b" to final). b) A conductance histogram for Au constructed from 1000 rupture traces, similar to the blue one in a). The main peak at exactly $1 G_0$ corresponds to the most likely atomic configuration at the moment of rupture.

Despite all the research devoted to the study of metallic nanocontacts during the last decade (see Refs. [11,17] and references therein), there are still unexplained phenomena and new emergent properties observed for these contacts. An example from the above list is the differences in the jump to contact behaviour of Au, Ag and Cu nanocontacts, not fully addressed until this work. In this thesis, the influence of relativistic effects is shown to provide the explanation (see Chapter 5, Section 5.2). Another example is the role of non-collinear magnetism in the unexpected low-conductance features of the experimental conductance histograms of ferromagnetic nanocontacts made of Fe or Ni. Are these features perhaps the result of ballistic magnetoresistance due to magnetic domain walls in the contacts [18]?

In view of the last two examples, which are described in more detail and posed as research questions in the next section, a method is needed that incorporates scalar- and vector-relativistic corrections in the standard computational toolbox that currently exists for the

study of atomic-sized point contacts, namely, that of CMD simulations of the lattice dynamics [19] and DFT quantum transport calculations [20].

1.2. Thesis statement and research objectives

In this work, a computationally efficient method is developed to explore the relative importance of relativistic effects on the emergent properties of representative *noble-metal* and ferromagnetic transition metal nanocontacts in low-temperature experiments. The emergent properties include the unusually large jumps to contact observed for Au vs Ag or Cu nanocontacts, the anomalous low-conductance peak structure in experimental conductance histograms of Ni nanocontacts, or the unusually high position of the first conductance peak of Fe nanocontacts in experimental histograms.

More specifically, this thesis seeks to address two research questions that are of fundamental importance to the understanding of bonding and electrical resistance at the atomic scale in transition metal nanocontacts.

The first question concerns the bonding strength in noble-metal nanocontacts, made of Cu, Ag or Au, respectively. Since these elements occur within the same group (11) of the periodic table, one would expect their bonding strengths to be comparable to one another. What then accounts for the much stronger bonding strength between nanoscopic surfaces made of Au –observed as a much larger jump to contact in conductance– than either Ag or Cu in STM/MCBJ experiments, as reported and partially addressed in Refs. [21–24]? Can scalar-relativistic effects, which are extremely important in *5d* metals such as Au, as most recently claimed in Ref. [17], explain this difference? In this thesis, pseudopotential and all-electron plane-wave DFT calculations are used to compare the interaction energies of infinite one-dimensional monatomic wires made of Au or Ag, as a function of interatomic separation [25–27]. Scalar-relativistic effects, spin-orbit coupling [27] and van der Waals forces [28,29], are explicitly included and excluded in order to evaluate the different contributions and highlight the central importance of (scalar) relativistic effects in gold.

The second question concerns the competing roles of the directionality of bonding between

atoms, on one hand, and (non-collinear) magnetism, on the other, in ferromagnetic 3d-metal nanocontacts. Do vector-relativistic effects, i.e., spin-orbit coupling, and the non-collinear magnetism it gives rise to in the nanocontacts, affect the latter's structural evolution and measured conductance? Or, is the distribution of atomic configurations, giving rise to peaks such as those of Fig 1.2 b), governed by the extent of covalent bonding within the materials? Clearly, it is pertinent to understand the relative importance of these two competing effects, particularly when the nanocontacts are about to form, or break. In this thesis, I will apply my model to Fe (a BCC metal) and Ni (an FCC metal), in order to shed more light on this second question.

In the case of Fe nanocontacts, a discrepancy has been observed between the first-conductance peaks of theoretical and experimental conductance histograms constructed from contact-rupture trials at 4.2 K in Ref. [30]. Is this discrepancy, as the authors contend, a fundamental limitation of the interatomic potential, of the EAM type [31], used to generate last-contact atomic structures in their CMD simulations? This conclusion was reached by the authors after trying several different EAM potentials. These potentials treat the bonding in metals as isotropic, an obvious shortcoming in the case of BCC metals, since they exhibit much greater covalent character than FCC metals. The relatively greater covalency in BCC metals is exemplified by the 4 fewer first-nearest neighbors in a perfect BCC vs FCC lattice. As an alternative theory, perhaps the formation of magnetic domain walls (DWs) at the moment the iron contacts are about to rupture, can explain the above discrepancy? DWs are known to affect conductance in ferromagnetic nanocontacts [16,18], since the atomic-sized constriction in the otherwise crystalline nanowire of some finite cross-section, effectively constitutes a different type of defect where a DW can nucleate.

Similarly, magnetic DWs have been proposed [32] as a possible explanation for the anomalous peak structure seen in conductance histograms recorded for Ni nanocontacts in STM/MCBI experiments [32–34]. Those histograms exhibit varying peak structure at first or last contact, when as few as one atom bridges the electrodes comprising the nanocontact. Most often [30,35–38], just a single broad peak centred at a conductance of $\sim 1.5 G_0$ is obtained. However, experiments have been performed in which sub-peak structure is revealed to be concealed by the single broad peak: a double-peak with a first maximum at $\sim 1.2 G_0$, and another at $\sim 1.5 G_0$ [32–34]. Once more, what is behind this

phenomenon, magnetic DWs pinned at the constriction at the moment of rupture or contact formation [39]? The peak at $1.2 G_0$ might correspond to a situation where an abrupt DW is present at the constriction, while when no DW is present, the other peak occurs. On the other hand, perhaps two different preferential last-contact structures, vertical dimers (inset of Fig. 1.1 b)) and monomers (inset of Fig. 1.1 a)), very commonly generated by EAM potentials in stretching simulations, along two different crystallographic orientations of FCC Ni [32,40–42], might correspond to the two different low-conductance peaks?

In this thesis, the second research question is explored primarily by combining, for the first time, CMD and SLD simulations, to study ferromagnetic nanocontacts made of iron and nickel. SLD is used in combination with the best available EAM potentials for these metals [43,44] to see whether or not the presence of spin-lattice coupling can affect the type of atomic arrangements that arise at the moment the contacts are about to rupture or form. As an alternative possibility, a very recent modified embedded-atom method (MEAM) interatomic potential [45], which is, as the name suggests, a modified version of the EAM potential in which the bonding has directional character, is used to explore the type of first- and last-contact structures these metals adopt in simulations.

Finally, to permit direct comparisons with the experiments, DFT electronic transport calculations, up to the vector-relativistic level of sophistication (including non-collinear magnetism), are employed to calculate the conductance of snapshots extracted from CMD and SLD simulations.

1.3. Approximations and limitations

This thesis is confined to the computational study of the noble-metal nanocontacts Cu, Ag and Au and two ferromagnetic metals, Fe and Ni. Two simulation methods are used to reproduce the dynamics of nanocontact evolution, depending on whether the metals are magnetic or not. CMD simulations are used to model the structural evolution of nanocontacts made from any of the aforementioned metals. Additionally, for the ferromagnetic metals, the SLD tools developed in this work are used to model the dynamic evolution of the spins in addition to the atomic structure. The simulations performed in this work mimic typical experimental conditions; i.e., liquid Helium temperature (4.2 K) under

ultra-high vacuum ($< 10^{-7}$ Pa).

The most severe limitation of CMD simulations is the time scale of the processes that can be accessed by this technique [17]. CMD simulations are confined to processes that occur over a few nanoseconds, at most. This means that physical processes that occur over a much longer time scale, .e.g., diffusion of atoms across the surface of the nanocontacts, are not currently within the reach of the simulations. Surface diffusion occurs on a microsecond time scale, and is thus extremely unlikely to be observed in CMD simulations that run for a thousandth of this time, and contain many fewer atoms than macroscopic systems, i.e., a few million at most. As in the past, the limitations resulting from diffusive effects have been circumvented by simulating at a very low temperature, when the barriers to diffusion are very high and these processes are thus extremely unlikely [46].

Another important limitation of CMD simulations that directly affects nanocontact evolution, is the speed at which the contacts are repeatedly ruptured and brought back into contact, in successive cycles. Previously defined in Sec 1.1, this process is also known as cyclic loading. Cyclic loading of nanocontacts is performed at ~ 1 m/s in this work, which is a standard speed in such simulations. However, this speed is several orders of magnitude faster than that used experimentally, due to the limitations in time scales discussed in the previous paragraph. Nonetheless, the nanocontacts are allowed enough time to achieve equilibrium during the elongation and compression phases of the cyclic loading because 1 m/s is still 3-4 orders of magnitude slower than the speed of sound in the metals (see Ref. [47] and references therein). As mentioned previously, simulations are performed at low temperature where diffusion is not expected to play a role.

Simulation system sizes of at most a few thousand atoms are used to model experimental nanocontact evolution in this work, since it is assumed that the ends of the nanocontacts are attached to semi-infinite electrodes with the symmetry of the bulk crystalline metal. In this sense, the system is not truly on a different scale as the bulk material but rather represents an interface between two bulk samples, connected by nanoscale “whiskers”. Two types of input structure are typically used in the simulations: (i) small, possessing only a few hundred freely moving atoms, is used in SLD simulations because they are much slower than ordinary CMD simulations; and (ii) larger, consisting of a little over a

thousand freely moving atoms, is used in ordinary CMD simulations. EAM potentials are used to describe the atomic structure of FCC nanocontacts, and where it fails, the MEAM potential is used because it takes directional, or covalent, bonding into account, which may be important for BCC metals.

The SLD models used in this thesis represent the current state of the art [48–51]. The one important limitation of these models is that the generalised Heisenberg exchange interaction in the SLD simulations, which depends on local spin-spin interactions as well as the separation between their centres, is too simple by virtue of being isotropic [48–50]. The true exchange interaction has anisotropies that are very sensitive to the exact details of the lattice positions the magnetic atoms occupy in the crystal, whether BCC or FCC [52–54]. However, given the difficulties of theoretically estimating pair-wise exchange and spin-orbit energies in vibrating lattices [55,56], and working out the elements of the anisotropic exchange tensor for arbitrary spin arrangements [54], the exchange interaction is limited to the isotropic part.

The isotropic generalised Heisenberg exchange term has an additional shortcoming. It does not guarantee conservation of total angular momentum between spin and lattice degrees of freedom. This becomes clear when only the lattice degrees of freedom are thermostatted. If the spins start out from a fully ferromagnetic state, the temperature of the spins remain zero, while that of the lattice rises to the target value quickly. The missing ingredient is spin-orbit coupling, which can be taken into account in the SLD simulations through a magnetocrystalline anisotropy energy (MAE) correction [55,56]. Given that the nanocontacts in this thesis have roughly axial symmetry, the uniaxial magnetic anisotropy correction in Ref. [55] represents an appropriate first approximation of magnetic anisotropy in ferromagnetic nanocontacts.

No external magnetic fields are applied in the SLD simulations, since domain walls (DWs) in nanocontacts in the *absence* of an applied field are of interest. Such DWs lead to (intrinsic) *domain-wall magnetoresistance* (DWMR). Hence, this work is not concerned with *anisotropic magnetoresistance* (AMR), which occurs when the angle of the applied field is varied relative to the direction of the current through the nanocontacts.

In the case of the DFT quantum transport calculations, only the *zero-bias conductance* of the nanocontacts are calculated and not the conductance at a finite bias voltage. A linear-combination-of-atomic-orbitals (LCAO) DFT quantum transport code, *ANT.Gaussian*, is used in this work to calculate the conductance of snapshots extracted from CMD and SLD simulations. These snapshots correspond to moments during the simulations when the nanocontacts are about to break or form. Unlike tight-binding (TB) calculations, which are computationally light and permit the collection of a large number of results for better statistics, DFT-based quantum transport calculations only permit the collection of a limited number of results. This is especially true of open-shell or spin-polarised calculations in the presence of even collinear magnetism, where the energy landscape is littered with local minima, which makes self-consistent convergence particularly difficult.

In order to perform conductance calculations on snapshots from SLD simulations with non-collinear spin configurations, whose origin can be traced to spin-orbit coupling, it has been necessary to modify the source code of *ANT.Gaussian* to take into account SOC [57]. Furthermore, *ANT.Gaussian* does not allow for non-collinear spin configurations, and the collinear spins resulting from a standard calculation are quantised relative to the (unknown) local atomic magnetisation axes. Therefore, in order to calculate the conductance of the non-collinear state, a unitary transformation [58–60] has been used to rotate the spins relative to the global quantisation axis along the z -direction, using the Euler angles (which measure the spin orientation relative to the global quantisation axis) from the output of the SLD simulations. This is a reasonable approach since, at low temperatures, magnetic excitations occur preferentially via transverse fluctuations of the magnetic moments, i.e., precession, and not longitudinal fluctuations (in the magnitude of the magnetic moments) [61]. Hence, employing a unitary transformation to rotate the spins should conserve the magnitudes of the magnetic moments.

It is also important to mention that the above implementation of SOC and non-collinear magnetism in *ANT.Gaussian* is not self consistent. The spin configurations are used as obtained from SLD rather than being further optimised, for instance, in unconstrained non-collinear DFT calculations, prior to doing the transport calculations in *ANT.Gaussian*. This is in contrast to the alternative approach of fully optimising spins subsequent to the SLD simulations, as is done in codes such as OpenMX [62]. Such an approach, however,

would have the well-known drawback of converging to almost any magnetic configuration [63], and thus lack predictability, and which would therefore require an arbitrary parameter, in constrained non-collinear DFT, to control the strength of constraints on spins. The latter approach is avoided in this work by using the spins from SLD as is.

Returning to the noble metals Au, Ag and Cu. The plane-wave DFT calculations reported in this work, which simulate the force-extension characteristics [29] of simple monatomic nanowires of these metals, can be performed in the presence or absence of scalar-relativistic and spin-orbit coupling corrections. Non-collinear magnetism is not allowed for in the SOC implementation in the plane-wave codes [64,65] used in this work. This is a reasonable approximation, since the noble metals are non-magnetic. Furthermore, recent experiments have failed to detect emergent magnetism in Au nanocontacts [14], which implies that anisotropic magnetoresistance (arising from SOC interactions) is not present in these systems, in turn, implying that non-collinear magnetism is not likely to be an important factor.

1.4. Definitions of technical terms and abbreviations

Adatom: A single atom adsorbed on the free surface of a mesoscopic solid material.

AMR(C): Anisotropic magnetoresistance (conductance). Difference between the resistances (conductances) across a voltage-biased ferromagnetic sample when an external magnetic field is applied perpendicular and parallel to the current flow. The phenomenon finds its origin in the spin-orbit interaction.

ANT.Gaussian: Alicante nanotransport; *ab-initio* software used to calculate conductance; interfaces seamlessly with the popular quantum chemistry software Gaussian.

Ballistic transport: The transport of electrons across a voltage-biased sample, such as a thin nanowire or constriction, in which at least one of its dimensions is smaller than the mean-free path of the electrons traversing the sample.

BMR(C): Ballistic magnetoresistance (conductance).

BCC: Refers to the body-centred cubic crystal structure.

CMD: Classical molecular dynamics

Conductance: Inverse of the electrical resistance.

Cyclic loading: The repeated contact formation and rupture of a nanocontact in a controlled manner.

DFT: Density functional theory.

Diffusive transport: The transport of electrons across a voltage-biased sample whose dimensions are larger than the mean-free path *and* phase coherence length of the electrons traversing the sample.

DWMR(C): Domain-wall magnetoresistance (conductance).

EAM: Embedded-atom method.

FCC: Refers to the face-centred cubic crystal structure.

HCP: Refers to the hexagonal close-packed crystal structure.

JC: Jump to contact.

JOC: Jump out of contact.

LAMMPS: Large-scale atomic/molecular massively parallel simulator; software used to perform CMD simulations in this work.

LCAO: Linear combination of atomic orbitals.

MAE: Magnetocrystalline anisotropy energy.

MCBJ: Mechanically controllable break junction, as described in Sec 3.1.2.

MEAM: Modified embedded-atom method.

Mechanical annealing: Cyclic loading of nanocontacts until they are stable and sharpened and undergo no further large atomic rearrangements upon continued cyclic loading.

Mesoscopic: Refers to materials whose sizes in at least one dimension range between the atomic, a few nanometers or more, and macroscopic, a few microns or less.

Nanocontact: An atomic-sized electrical junction formed between two macroscopic-sized conductors, such as those routinely created in a scanning tunnelling microscope or mechanically controllable break junction experiment.

Nanosopic: Refers to materials whose sizes in at least one dimension are smaller than a few nanometers, all the way down to the atomic limit.

Noble metal: In this thesis, the elements gold, silver or copper.

OpenMX: Open-source Materials Explorer; *ab-initio* software used to calculate conductance.

Quantum coherent transport: The transport of electrons across a voltage-biased sample, such as a thin nanowire or constriction, in which at least one of its dimensions is smaller than the phase coherence length of the electrons traversing the sample.

SLD: Spin-lattice dynamics.

Smoluchowski effect: The formation of a surface dipole at an adsorbed atom on an otherwise clean metal surface of the same element; it results from the delocalisation of the adatom's valence electrons toward the surface beneath it.

STD: Suzuki-Trotter decomposition integration algorithm used in SPILADY.

STM: Scanning tunnelling microscopy, as described in Sec 3.1.2.

Uniaxial magnetocrystalline anisotropy: Magnetic anisotropy in systems with only one high-symmetry axis, such as materials with a HCP crystal, or any system with axial symmetry.

Work hardening: See Mechanical annealing.

Zero-bias conductance: The (theoretical) conductance across a nanocontact in the limit of zero voltage applied across its ends.

1.5. Significance

Disentangling the roles of competing geometric, electronic and magnetic effects in electronic transport through atomic-sized metallic nanocontacts is both important from a fundamental point of view, since it teaches us about the importance of these phenomena in the limit of a single atom and in bonding between a few atoms. In technological applications, it is crucial to understand these effects on spin-polarised transport, i.e., in spintronics [1], one of the most active and promising research fields in quantum computing.

Relativistic effects play a central role in heavy transition metal elements such as Au, by, for example, leading to smaller than expected lattice constants for these metals, as a result of the contraction of their valence s orbitals, among other phenomena [66]. In low-dimensional systems such as nanocontacts, relativistic effects are expected to lead to even more exotic phenomena than in the bulk metals, such as the formation of suspended monatomic chains, several atoms long, when Au contacts are ruptured [67]. Studying how relativity affects the electronic transport properties of Au nanocontacts therefore leads to a better understanding of bonding between the atoms in these low-dimensional systems.

Ferromagnetic nanocontacts have never been modelled by SLD with spin-orbit coupling

before, which provides a unique opportunity to study how (non-collinear) magnetism and atomic structure interact when the nanocontacts evolve dynamically under cyclic loading.

Two important challenges, therefore, arise in the modelling undertaken in this work: the coupling between the lattice and the atomic spins, which implies making use of combined CMD and spin dynamics, or spin-lattice dynamics, and the inclusion of spin-orbit coupling and non-collinear magnetism in DFT transport calculations. As a result, modifications of the source code of widely used simulation software, e.g., the *Large-scale atomic/molecular massively parallel simulator (LAMMPS)* [50] and *spin-lattice dynamics (SPILADY)*, as well as ANT.Gaussian [68], or of their parameters, have been developed as part of the work presented in this thesis.

These newly-developed tools, far from being applicable to only the systems studied here, can be applied to other exciting low-dimensional materials of current interest, such as ferromagnetic thin films and nanowires. These materials are promising candidates in non-volatile memory applications [69]. Hence, the tools developed in this work can be extended to study, for example, the stability and dynamics of mobile Skyrmions [70] on thin films, and transverse domain walls [71] in ferromagnetic nanowires, in the presence of defects and temperature shocks and gradients. In summary, the new tools open a whole new avenue of research into low-dimensional systems where magnetic and structural degrees of freedom are intimately coupled.

2. LITERATURE REVIEW

Below follows a discussion of the literature related to the research questions that have been posed in this thesis.

Section 2.1 briefly discusses the literature on the emergent properties of the noble-metal nanocontacts, Au, Ag and Cu, which manifest themselves in electronic transport measurements immediately before and after contact has been established.

Section 2.2 provides survey of the literature related to electrical resistance arising from the existence of magnetic domain walls in atomic-sized ferromagnetic Ni and Fe nanocontacts.

2.1. A brief account of metallic nanocontacts and scalar-relativistic effects

Since the early 90s, and with the discovery of quantisation of conductance in nanocontacts [72], there has been an important research effort devoted to understanding traces of conductance such as the one shown in Fig. 1.2 a), including the conductance histograms (Fig. 1.2 b)) that are obtained from measuring thousands of these traces [11]. The conductance histograms have some characteristic features that are different for different materials and contain information about the atomic structure of the contact as it narrows and breaks.

Many of the studies described in the comprehensive review of the “Quantum properties of atomic-sized conductors” in 2003 by Agraït *et al.* [11], have focused on understanding the behaviour right after contact, that is, the first peak in the histograms of conductance. In most cases, this peak can be understood from the electronic structure of the last atomic contact and the geometry of the contact. Classical molecular dynamics simulations together with *ab initio* based electronic transport calculations, have been able to explain most of the existing experimental histograms of conductance [11,40,41,73–75]. For example, the three metals, Au, Cu and Ag, which are studied in this work, are found to behave very similarly

to each other, in that they, generally, form the same types of first- and last-contact structures (immediately after contact is made, or just before the contact is broken). These structures are monomers (a single atom forming the contact, as shown in Fig. 2.1 a), dimers (two atoms making the contact, Fig. 2.1 b)) and double- or higher contacts with more than 2 atoms in the constriction (Fig. 2.1 c)).

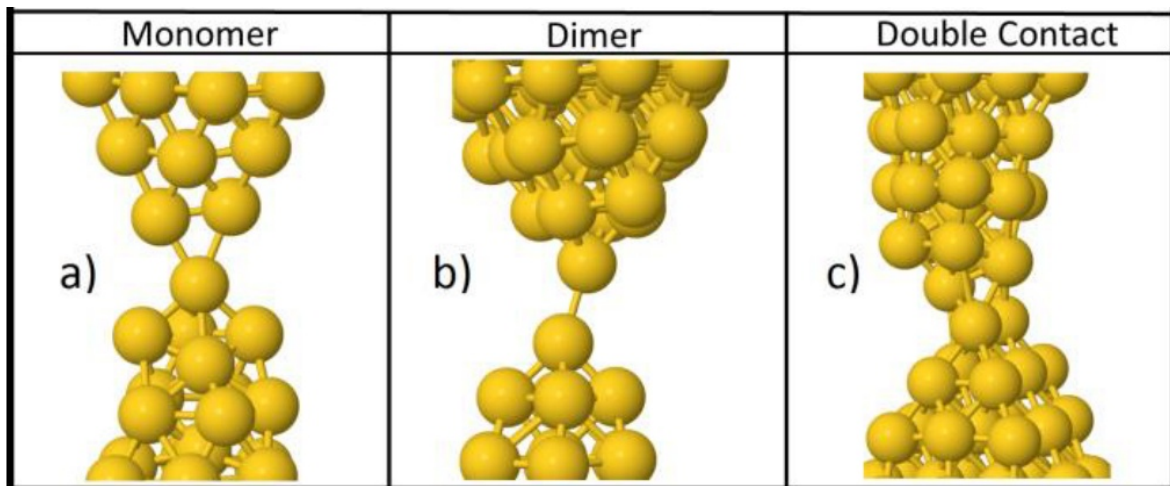


Fig. 2.1: Typical last-contact structures obtained from CMD simulations of cyclic loading of (111)-oriented Au nanocontacts at 4.2 K [76]: a) A “4-1-2” monomer, b) a “4-1-1-5” vertical dimer and c) a “6-2-6” double contact.

As an example, note that a monomer and a monatomic chain of Au atoms, including the dimer, both exhibit conductance quantisation of around $1 G_0$, which in this case is the signature of electronic transport through a single, fully open, transmission channel: the $6s$ orbital of the gold atom(s) [77]. In this way, electronic transport through a monomer or monatomic chain of Au atoms gives rise to the the largest, left-most peak in the histogram of Au as we saw in Fig. 1.2 b). However, in general, the atoms in the constriction have different numbers of nearest neighbours, and these neighbours may adopt different geometrical arrangements, leading to variations in the measured conductance, and hence a broadening of the peaks that can be seen in the conductance histograms. In the case of monomers, for example, this variation can be as much as 20% about the central value of $1 G_0$.

As we have seen, the electrical properties of single-atom contacts are strongly influenced by their coordination to the leads. The coordination ultimately determines the geometry of

the structure, and both the coordination and geometry clearly depend on the mechanical properties of the material at hand.

The accuracy with which molecular dynamics models can replicate material properties, and hence the geometry and coordination of nanocontacts, depends crucially on the interatomic potentials that are used in the models. In the present work, for our CMD simulations of cyclic loading of metal nanocontacts, we make use of embedded-atom method (EAM) interatomic potentials [78], which are currently considered to be the most well-suited potentials for modelling metals [79].

To date, most of the features of experimental histograms of conductance have been explained but, by no means, all of them. It is particularly difficult to understand the behaviour of magnetic nanocontacts, since, as discussed by Jacob *et al.* [15], not only the electronic structure of the last contact and the geometry of the contact play a role, but also the presence of inhomogeneous magnetic profiles, such as magnetic domain walls. The latter phenomenon will be described in more detail in the next section since the study thereof is also one of the objectives of this thesis.

But even when considering non-magnetic materials there remain unresolved questions.

Most of the work done on nanocontacts has been focused on the atomic structure right before or right after contact. A few studies have also focused on the peculiar behaviour of some materials that exhibit a jump to contact (JC), or a jump *before* physical contact, in the measured conductance, as is the case of Au, also shown in Fig. 1.2 a). Here, large differences between Au and Ag or Cu nanocontacts have been noticed. Until very recently, it had only been speculated or, at best, shown qualitatively, that the observed larger bonding strength between nano-electrodes made of Au, as opposed to those made of Ag, are the result of the stronger relativistic effects in this *5d* metal [17]. Recent evidence compiled by experimental colleagues show that the larger bonding strength manifests in the experiments as a much larger JC in measured conductance, when pure gold point contacts, instead of copper or silver ones, are made [24]. The focus of this work is on explaining these differences and proposing a relativistic effect as the underlying cause. Even though relativistic effects are often not explicitly included or excluded in *ab initio*

calculations of the conductance of nanocontacts, it is known that these effects can explain significant differences between Au versus, for example, its iso-electronic analogue, Ag, immediately above it in the periodic table of the elements (see Ref. [17] and references therein).

As the atomic mass of an element increases, relativistic effects begin to modify the electronic structure of atoms, and change the properties of especially heavy-element crystals and compounds (See Ref. [80] for a very thorough review). One consequence is the simultaneous contraction of the outer $6s$, and expansion of the $5d$, orbitals of Au, as well as an enhanced hybridisation of these valence $s-d$ orbitals [80].

Indeed, relativistic first-principle calculations in 1987 showed that the abovementioned $s-d$ hybridisation explains why the lattice parameter of Au (4.08 Å) is slightly smaller than that of Ag (4.09 Å) [66]. In the same year, and also via relativistic first-principles calculations, the missing-row reconstruction of exposed (011) surfaces of Au was explained as originating from the same hybridisation of the outer valence orbitals [81].

This phenomenon of surface reconstruction was later used to explain the formation of monoatomic chains, more than two atoms long, during the rupture of Au, Pt, and Ir nanocontacts [67]. Several prior and follow-up theoretical studies corroborate this experimental finding [25,82,83]. However, until the present work, the role of relativistic effects during the formation and rupture of transition metal nanocontacts in STM and MCBJ experiments, had been confined to the formation of monoatomic chains [26,27,67,84].

In the past, the bulk elasticity along various crystallographic orientations of the lattice, was proposed as an explanation for the differences in JC between different metals [23,24]. In this case, CMD simulations were used. Given that the parameterisations of the interatomic potentials used in the CMD simulations can capture scalar-relativistic effects at least to some extent, this is not surprising (the potentials are typically fitted to data obtained from scalar-relativistic *ab-initio* calculations as well as experiments [85].)

Instead of scalar-relativistic effects, another effect that may be considered to account for

the larger jump to contact in gold is dispersion or van der Waals (vdWs) forces [29,86]. Such forces are usually ignored in the theoretical approach described above, but have been included in DFT calculations to more accurately describe the longer-range interaction tails between atoms and molecules in low-dimensional environments (when they are surrounded by vacuum slabs) [87]. Furthermore, even in the bulk noble metals, adding vdWs corrections in DFT calculations has resulted in better estimates of their lattice constants [86]. Nevertheless, in Ref. [29], it is claimed that vdWs interactions have only a minor quantitative effect on the force-extension characteristics of nanocontacts. For this reason, they were excluded from the calculations described there. However, to be thorough in its exploration of the competing effects on gold's unusual JC characteristics, in this work, vdWs interactions have been included in the DFT force-extension calculations carried out on monatomic wires made of noble metals.

Finally, vector-relativistic effects, i.e., those arising from spin-orbit coupling, may also be expected to affect the interaction potential felt by noble-metal nanocontacts in the tunnelling regime, especially in the case of gold [26,88]. In ferromagnetic metallic nanocontacts, for example, SOC leads to a magnetocrystalline anisotropy energy (MAE), which produces preferential magnetisation axes in, e.g., infinite monatomic wires [49]. But in the non-magnetic noble-metal nanocontacts, magnetism is absent even in strongly relativistic gold nanocontacts, and SOC is not seen to play an obvious role [14]. It is thus not clear how important a role SOC plays during the formation or rupture of noble-metal nanocontacts. To clarify the role of SOC, it has been included, in this thesis, in the force-extension calculations carried out on monatomic noble-metal wires (See Chapter 5, Sec 5.2).

In conclusion, the influence of the above competing effects (scalar-relativistic, vdWs forces, spin-orbit coupling) on noble-metal nanocontacts *before* first contact, are, in this thesis, explored by means of plane-wave DFT calculations of the force-extension characteristics of infinite monatomic wires consisting of Au or Ag atoms (see Chapter 5).

2.2. An account of domain-wall magnetoresistance in Ni and Fe nanocontacts

Understanding the behavior of magnetic nanocontacts presents numerous challenges. Complex coupling between lattice dynamics, electronics and spins are difficult to take into account in a single, accurate, model. However, the possibilities that can be opened by understanding and controlling the properties of magnetic nanocontacts, in particular for applications in spintronics, as well as understanding magnetism down to the atomic level, make this challenge worth the effort.

Histograms of conductance of magnetic materials show a complex and varied behavior [89]. In Ni, for example, just one broad peak centred at $\sim 1.5 G_0$ is observed in most cases [30,35–38] (see Fig. 2.2 a) for one recent example), while in some cases this peak can be resolved into two low-conductance peaks, centered at ~ 1.2 and $\sim 1.5 G_0$ [32] (see Fig. 2.2 b)), a phenomenon already observed in 1997 [33]. In fact, the position of these peaks change slightly from one experiment to another and, interestingly, can be shifted with increased bias voltage [32].

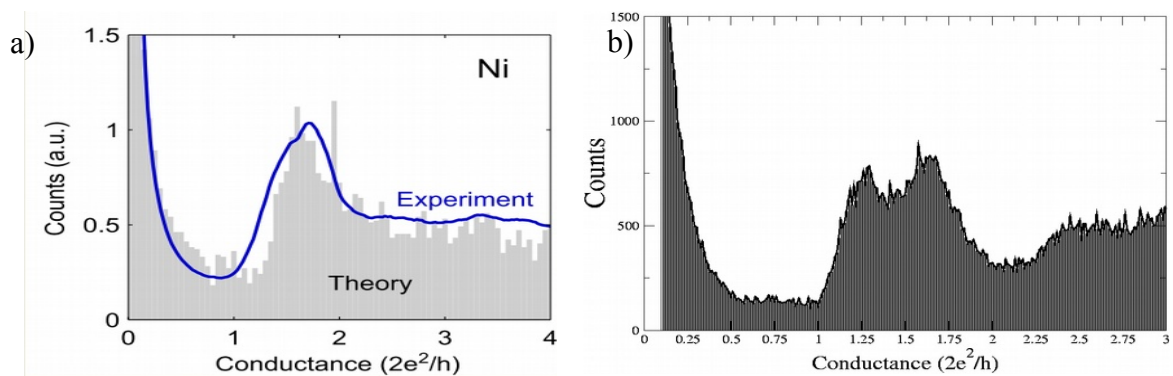


Fig. 2.2: a) Experimental (thick blue line) and theoretical (grey shaded area) conductance histogram for Ni, extracted from [30]. b) Experimental conductance histogram for Ni extracted from [32].

Another example is Fe, where the first peak of the histogram of conductance has not been successfully explained yet. The best model to date [30] gives a position of this peak at around $1.4 G_0$ while the experimental result is closer to $2 G_0$.

In ferromagnetic nanocontacts, besides the electronic structure of the last atomic contact and the geometric structure, magnetic domain walls (DWs), that is, the presence of interfaces separating magnetic domains, could affect electronic transport [15]. This may be one of the explanations as to why it has been difficult to explain histograms of conductance in Ni or Fe. In fact, some authors claim that the formation and pinning of a domain wall at the constriction may be responsible for the first low-conductance peak at $\sim 1.2 G_0$ [32]. As a result of the pinning of magnetic domain walls at the constriction of the nanocontacts [39], ballistic magnetoresistance (BMR), that is, changes in resistivity in the presence of an external field in the ballistic regime, or, equivalently, *ballistic magnetoconductance* (BMC), presumably arises in ferromagnetic nanocontacts.

DWs can either enhance [90] or reduce [91] the transmission of electrons through the nanocontacts. BMC is strictly defined for ferromagnetic nanocontacts as $\frac{G_{\uparrow\uparrow} - G_{\uparrow\downarrow}}{G_{\uparrow\downarrow}} \times 100\%$ [17,92], where $G_{\uparrow\downarrow}$ is the conductance across the constriction when the magnetisation in the bulk leads, on either side of the constriction, is aligned anti-parallel, and $G_{\uparrow\uparrow}$ is the conductance, when it is aligned parallel. Such magnetic configurations are usually realised in experiments by applying two separate external magnetic fields to the two macroscopic electrodes on each side of the nanocontact. In the following, a discussion is presented of the most important experimental and theoretical facts known about magnetoresistance in ferromagnetic nanocontacts.

Domain-wall magnetoresistance (conductance) (DWMR or DWMC) was detected for the first time in 1994-5 [93,94], at low temperatures (< 10 K) in *mesoscopically* thin Ni nanowires (with diameters several tens of nanometers across). The authors measured the resistance in the wires with a magnetic field perpendicular and parallel to the direction of flow of the current in the wires. Such studies are difficult to undertake by other means, e.g., superconducting quantum interference device (SQUID) magnetometers, due to the small sizes of the samples.

The DWMR detected in Refs. [93,94] was referred to as longitudinal magnetoresistance to distinguish it from anisotropic magnetoresistance (AMR) [95]. AMR arises from the change in resistivity of a bulk or mesoscopic ferromagnetic sample as a function of the

angle of the applied external magnetic field to the direction of the current passing through the sample. As will be seen in Section 4.3.1, AMR requires very strong spin-orbit coupling to be appreciable, which is not the case of the ferromagnetic 3*d* transition metals.

Briefly, then, longitudinal magnetoresistance was detected in Refs. [93,94] when the external magnetic field, in the parallel configuration, aligned along the direction of the flow of the current in the nanowires, was swept from large positive to large negative values. The hysteresis in the measured resistance was interpreted as arising from a magnetic domain wall passing through the wire when the magnetisation was reversed, the result, in turn, of cycling the external field between large negative and large positive values (with respect to the flow of the current). This phenomenon did not appear when the external magnetic field was applied perpendicular to the wires.

Tatara and Fukuyama made a first attempt in 1997 [96] to explain how the interaction between conduction electrons and a domain wall in a thin ferromagnetic wire could affect its resistance. In this way they were able to reproduce the experimental change in conductance observed for thin Ni nanowires in Refs. [93,94].

In 1998, further experimental work at low temperatures (< 80 K) was undertaken to study the BMR resulting from the nucleation and motion of DWs in micron and submicron Fe wires, and in Co wires and paired disks [90,97,98]. For the structures most similar to the nanocontacts considered in this thesis, the nanowires, it was found that the conductivity of the samples were slightly enhanced at low external magnetic field. Presumably, this was a result of the nucleation and movement of DWs through the sample during magnetisation reversal (with hysteresis) of the sample. It was hypothesised in Ref. [96] that DWs destroy weak localisation of the electrons at low temperatures, the result of phase coherence, and, in turn appears to enhance conductivity (reduce resistivity) because, presumably, Pauli repulsion is reduced. This is at odds with the mechanism in giant magnetoresistance (GMR) materials that the operating principle of magnetic read-and-write heads in hard disk drives is based upon. The domain walls in these devices enhance resistivity because they mix spin majority and minority channels in the wall [99].

In the mesoscopic ferromagnetic nanowires discussed up to now, which measure several tens of nanometers in diameter, very wide domain walls can form that are on the order of the diameter of the wire [39], and in such DWs the spin textures vary smoothly from one side of the wall to the other. In a static picture, this leads to a very small contribution to the DWMR (or DWMC) of the wire because the spins can adjust their orientations adiabatically from one side of the DW to the other [92].

In 1998, Oshima and Miyano [91] studied the effect of spin-polarised current in atomic-sized Ni point contacts created in high vacuum ($< 10^{-1}$ Pa) at room temperature, above and below the Curie temperature of Ni (~ 630 K), and in the presence and absence of an externally applied magnetic field. They took great care to ensure that the nanocontacts were free from contamination in their experiments, which is a problem for hard Ni as compared to malleable Au or Cu, since in the case of the latter two, plastic deformations can easily rid the surfaces of contaminating layers and thus permit clean metallic contacts to be re-established.

By accumulating consecutive conductance measurements during the pull-off, or rupture, phase of the experiments, cumulative conductance histograms could be constructed under the various combinations of the parameters of the experiments. In this way it was possible to observe the difference between the most likely conductance values when the contacts were ferromagnetic, below the Curie temperature, or paramagnetic, above it. The fact that the histograms were constructed cumulatively also made it possible to verify that the histograms were stable from the very beginning, i.e., when only few data had been recorded at first.

Below the Curie temperature, it is expected that only three spin channels, two $4s$ and one $3d$, would each contribute $\frac{1}{2} G_0$ at most to the conductance at last-contact during the rupture phase, for a total of $1.5 G_0$ as the first maximum in the histogram. This is because the spin majority $3d$ channel is completely below the Fermi level in ferromagnetic Ni, and hence cannot contribute to conduction at the Fermi level [94]. Above the Curie temperature, Ni is paramagnetic and both $3d$ spin channels, in addition to the two from the $4s$ orbitals, can now contribute to conduction for a total of $2 G_0$ as the first maximum in

the histogram. This is indeed what is seen in the histograms above and below the Curie temperature of Ni in Ref. [91].

An interesting observation was made in Ref. [91] that ties in well with the research objective of this thesis concerning the double-peak structure in Ni histograms at low conductance values [32–34]. In the absence of an external magnetic field, the alignment of the magnetisation in the bulk electrodes adjacent to the constriction cannot be guaranteed, and hence a magnetic domain wall may nucleate at one or both of the boundaries between the constriction and the two electrodes, but, according to Oshima and Miyano [86], not in the constriction itself. In the presence of such a DW between two magnetisation directions at different angles, the transmission across the DW of a spin-polarised $3d$ electron depends on the difference between the angles, and decreases as the difference becomes greater. Hence, in the extreme case, i.e., a difference in angles of 180° , it is possible that only the $4s$ channels transmit electrons, and also that the first maximum in the conductance histogram occurs exactly at $1 G_0$. However, in most cases the conductance will range between 1 and $1.5 G_0$ since the angle between the magnetisations in the bulk leads will not be maximum.

The first theoretical BMR results for point contacts were reported in 1999 [100], in the ballistic but not quantum-coherent limit. Thus, no lateral quantisation of electrons in the constriction was assumed. This precludes atomic-sized point contacts in which the transport is in the quantum-coherent limit. This limit is reached when the diameter of the constriction is on the order of the Fermi wavelength of the metal (~ 0.5 nm). In Ref. [100], a local gauge transformation was used to diagonalise the exchange field that arises from the presence of a domain wall in the constriction of the nanocontact. But instead of using second-order perturbation theory as in Ref. [96], the Wentzel-Kramer-Brillouin (WKB) approximation was used, since it is valid even in the limit of a vanishing exchange field. The authors' calculations, which ignored spin-orbit coupling, shows that the DW mixes the majority and minority spins much as SOC would, and that the effect increases the DWMR when there are many almost degenerate spin-split bands close to the Fermi level. As opposed to a simple two-band model in which the increase in DWMR is quadratic, it increases linearly with the abruptness of the DW when more realistic band structures are used in the calculation. Since DWs are expected to be most abrupt when they are pinned in

atomic-sized constrictions, it is predicted that really large DWMR would occur in ferromagnetic point contacts, although a maximum of only 70% for a planar DW, i.e., one-atomic layer thick, was estimated.

In 1999, BMR was measured for the first time in atomic-sized Ni point contacts at room temperature and in the presence of a magnetic field [101]. One of the electrodes was magnetised in an oscillating field to accomplish parallel and anti-parallel magnetisations in the electrodes adjacent to the constriction. For the narrowest contacts, only a few atoms wide, DWMR of up to 300% was measured. The DWMR also seemed to decrease exponentially with increasing contact cross-section, and hence conductance. Care was taken to rule out magnetostrictive or magnetostatic, i.e., mechanical, effects [102] that could alter the atomic configuration at the minimum cross-section and hence give rise to MR other than that from the presence of domain walls.

In a follow up work [103], theory was developed to explain the universal scaling of the DWMR as a function of conductance or, equivalently, contact cross-section, first noticed in Ref. [101]. The model of DWMR in Ref. [103] depends, on the one hand, on the ratio of the difference between the spin-resolved density of states to the total density of states at the Fermi level, and, on the other hand, the width of the domain wall. This model was used to explain how very narrow domain walls pinned [39] at the constriction of the nanocontacts could lead to very large DWMR, and also decrease rapidly when the contact cross-section, and by extension domain wall width, increased.

In all of the literature on BMR covered up to this point, the DWMR was measured in the presence of an external magnetic field. Since the focus of this thesis is domain walls in ferromagnetic nanocontacts, in the *absence* of an external magnetic field, the aforementioned literature is not directly relevant to this thesis, but provides context. Thus, for a thorough review of BMR in macro- and mesoscopic ferromagnetic structures, in the presence of external magnetic fields, outlining the basic theory as well as the most important experimental results, the interested reader is referred to chapter 18 in volume 5 of Ref. [92].

Another interesting feature first observed experimentally by Ono et al [104] in Ni atomic point contacts at room temperature, is conductance quantisation at *half-integer* $G_0 = 2e^2/h$ steps. The constriction was made fully ferromagnetic by applying a large enough external magnetic field of the same orientation, on the two bulk electrodes adjacent to the constriction. The resulting current across the nanocontact was fully spin-polarised, since conductance quantisation occurred at integer multiples of e^2/h of up to about 7, instead of integer multiples of the spin-degenerate $G_0 = 2e^2/h$.

Qualitatively, the half-integer conductance quantisation can be explained as follows [89]: Since the spin minority and majority electrons experience different exchange fields, spin degeneracy is lifted in ferromagnetic materials. Correspondingly, the number of transmission channels at the Fermi level in a given ferromagnetic nanocontact, depends on the spin orientation in the presence of an external magnetic field that fully aligns the magnetisation of both bulk ends of the nanocontact.

However, when the alignment of the magnetisation in the bulk ends is anti-parallel, a domain wall must exist across the nanocontact, whose width usually scales with the size of the constriction [39]. Now spin degeneracy can be restored because the DW re-introduces both spin species and conductance quantisation at integer steps of $G_0 = 2e^2/h$ is observed. In the absence of any external magnetic field, on the other hand, conductance quantisation at the usual spin degenerate quantum of conductance G_0 is also recovered. The same experiment was repeated in Ref. [104] on Cu in the presence and absence of a magnetic field, and no *non* spin-degenerate conductance quantisation was observed.

Finally, if the DW in the ferromagnetic nanocontact is very abrupt, the magnetisation has to rotate from its orientation in one end of the nanocontact, to the opposite orientation in the other end, but at an atomic scale. In this case, the DW sets up a potential step whose height is on the order of the exchange splitting between majority and minority spins. Since transmission is ballistic in nanocontacts, the only source of spin-dependent resistance is then provided by reflection from the potential step set up by the very abrupt DW that spans the atomically-narrow constriction [89]. Furthermore, the longitudinal kinetic energies of conduction electrons in very narrow nanocontacts can become smaller than the exchange

splitting and hence, in theory, lead to very large values of the magnetoresistance (see Ref. [89] and references therein).

Half-integer conductance quantisation was also reported for iron point contacts at 4.2 K and in ultra-high vacuum, in the presence [105] and absence [106] of an external magnetic field. The authors admitted that the half-integer conductance quantisation was only partly realised and that further experimental work was required to fully explain the phenomenon.

More work was subsequently undertaken on electrodeposited Ni nanocontacts in Ref. [107], in order to rule out magnetostrictive, magnetostatic [102] and other mechanical effects, such as two-level fluctuations [108], which could lead to a large change in the resistance of contacts. Such a study was useful for ruling out the aforementioned effects because the technique of creating nanocontacts by electrodeposition is much less susceptible to mechanical instabilities. Although mechanical effects could almost be ruled out entirely, the authors of Ref. [107] observed half-integer conductance quantisation even in the absence of an external field as well as large BMR of several hundred percent when the sample was exposed to a cycled external magnetic field.

Other studies using the electrodeposition technique to create ferromagnetic nanocontacts also reported DWMR of several hundred percent and even several thousand [109], as well as conductance quantisation at half-integer steps of $G_0 = 2e^2/h$ [110,111]. Surprisingly, even non-magnetic metals such as Au [112] and Cu [113] were found to exhibit half-integer conductance quantisation. As early as the year 2000, it was suggested in Ref. [112] that the ions in the electrolyte solution could act as centres for defect scattering because they would aggregate about the nanoconstriction and give rise to large values of DWMR and the quantisation of conductance at half-integer values of $G_0 = 2e^2/h$.

A simple theoretical *ab-initio* treatment [114] would go on to show that defect scattering, resulting from contamination of the constriction surface by oxygen, is most likely responsible for large DWMR and half-integer conductance quantisation in atomic point contacts, by virtue of completely spin-polarised *p* orbitals on the oxygen atoms. Trace amounts of atmospheric gases such as oxygen are always present even in the ultra-high vacuum (UHV) environments created in MCBJ and STM setups.

A very important experimental study carried out by Untiedt *et al.* in 2004 [35], in an STM setup at low temperature and in ultra-high vacuum, on Fe, Ni, Co and non-magnetic Pt nanocontacts, would largely confirm the above theoretical finding not only for oxygen, but for other gases too. Another much more recent experimental study in 2015 also confirms this result for Ni [38]. For the sake of completeness, I mention that a competing explanation for half-integer conductance quantisation, observed even in the absence of an externally applied field, in both magnetic (Ni) and non-magnetic (Cu) metal nanocontacts, and proposed in Ref. [115], is the formation of point contacts in parallel between the sample surfaces in experiments.

Several careful experimental studies on Ni nanocontacts in different setups, e.g., low-temperature break junction [89], room-temperature electrodeposition avoiding oxidation [111], and room-temperature electron-beam lithography [116], obtained more modest values of the DWMR (~50%) in applied fields. This magnitude is more consistent with the most recent experimental work where the magnetoresistance has been unambiguously attributed to the presence of domain walls in permalloy ($\text{Ni}_{80}\text{Fe}_{20}$) nanoconstrictions, even in the *absence* of an external magnetic field [16,18]. At least one older study on permalloy also obtained DWMR values in this range [117].

Turning now to theoretical studies, past treatments of magnetic nanocontacts have mostly been confined to small idealised geometries in *ab-initio* calculations, both scalar- and vector-relativistic [15,17,32,59,118–127]. Another approach uses micro-magnetic simulations [116,128], which are continuum models of spin textures on finite-element meshes of varying shapes and sizes, but whose smallest dimension is at least a few nanometers across, and thus well in excess of the atomic point-contact limit. Although atomistic detail is taken into account in the *ab-initio* studies, sometimes involving asymmetric or relaxed contact structures [15,32,59,123], these approaches fail partially in the idealised *ab initio* case, and completely for continuum finite-element meshes, to capture realistic atomic configurations that exhibit considerable disorder, a result of finite temperatures and the cyclic loading of contacts routinely performed in STM and MCBJ experiments [129,130].

Jacob *et al.* [15] made an important contribution to clarifying the controversy surrounding the existence of very large intrinsic DWMR in Ni point contacts. DFT quantum transport calculations were performed on a very simple 28-atom (001)-oriented Ni nanocontact (see the insets of Fig. 4.10, which show similar structures), with a dimer bridging the contact. In order to simulate anti-parallel and parallel magnetic configurations in the electrodes, the contact was oriented along the x -axis, physically lying on its side. In the ANT.Gaussian DFT quantum transport software used in the study, only collinear magnetic spin configurations were permitted, with “up” and “down” spins being understood as being oriented along the positive and negative z -axis, respectively. The authors performed an orbital eigenchannel analysis [131] of their transmission results to show that the spin-resolved transmission channels at the Fermi energy, contributing to conduction through the contact, consisted of, on the one hand, spin-majority sp hybridised orbitals, which are not too sensitive to the particular configuration of the atoms in the constriction, and can contribute to transmission at larger interatomic separations, and, on the other hand, spin-minority spd hybridised orbitals, which are very sensitive to the contact geometry and more localised than the majority-spin orbitals.

Thus, by performing a rupture “simulation” of the simple contact, i.e., relaxing the atoms sandwiched between the single frozen layer on opposite ends of the contact, and starting geometry relaxation at different separations between the frozen ends, it was observed how the spin-minority channel became blocked by disorder and stretching of the contact, leaving only the spin-majority channel to transmit. In parallel magnetisation configurations of the electrodes, this led to a very small value of magnetoresistance due to “orbital blocking” as a result of a geometric effect. In the anti-parallel configuration of the magnetisation in the electrodes, a maximum of 30% DWMR was obtained as the contact was stretched and deformed. It was noted that in a perfect monatomic wire with a DW, a maximum DWMR of 250% had been obtained (see Ref. [15] and references therein). It bears mentioning here that an earlier theoretical study [123] compared an unrelaxed and relaxed three-atom chain of Co atoms sandwiched between non-magnetic electrodes, and also came to similar conclusions as Ref. [15]. However, since three-atoms chains are highly unlikely to form for Fe, Ni and Co [27], and Ref. [15] draws more explicit attention to the geometric nature of the magnetoresistance in stretched and ruptured Ni nanocontacts, the latter reference has been discussed here in somewhat more detail.

All models and calculations described until now for ferromagnetic nanocontacts do not consider the dynamic evolution of the system with time as the nanocontact forms or breaks. Even in Monte Carlo simulations [132,133] of domain walls in ferromagnetic nanoconstrictions, on frozen lattices, the atomic structure was not allowed to evolve dynamically as they would in experiments. CMD simulations, on the other hand, are capable of achieving realistic atomic geometries in the modelling of dynamically evolving magnetic metal nanocontacts [30,75]. Recently, the spin degree of freedom has been included directly in CMD [48–50]. But, to the best of my knowledge, never to model dynamically evolving ferromagnetic nanocontacts. This is one of the novelties of the work presented in this thesis.

In light of the above, to model ferromagnetic nanocontacts within the spin-lattice dynamics framework, it is not merely enough to include the spin degrees of freedom and a generalised exchange interaction between the spins, as done previously [48–50]. In order to capture the transfer of angular momentum between the spins and lattice, i.e., conservation of total angular momentum mediated by spin-orbit coupling, a magnetocrystalline anisotropy energy correction that is compatible with the axial symmetry of the nanocontacts, or a generalised uniaxial anisotropy [56], has to be added to existing spin-lattice dynamics codes such as SPILADY [134].

In summary, the above overview of the influence of magnetic domain walls on the conductance of ferromagnetic nanocontacts, is covered in more detail in chapter 18, volume 5 of Ref. [92], and also in Ref. [135], which summarises the discussion of BMR in this thesis, including the consensus finding that DWMR only amounts to a few tens of a percent in very narrow ferromagnetic nanocontacts, i.e., in the atomic point contact limit. Ref. [135] also very briefly addresses all the controversies surrounding the origin of BMR in atomic-sized point contacts.

Another review questioning even the premise of the concept of BMR, is also worth consulting. According to Doudin and Viret [136], the term *ballistic* magnetoresistance should apply only when the full opening and/or blocking of transmission channels by magnetic or spin-filtering effects takes place, and not when partial closing off or opening

of transmission channels occurs, even when the latter is the result of magnetically-induced scattering of electrons at the constriction.

One of the main research objectives of this thesis is to apply and extend state-of-the-art models of the dynamics of atoms *and* spins, as well as *ab initio* methods, to ferromagnetic nanocontacts. The combined use of these models allows exploring the contribution of different mechanisms to the conductance of these nanocontacts. As an application, these models will be used to study the low-conductance “twin peaks” sometimes seen in histograms constructed for Ni nanocontacts [32–34]. Because their exact positions were found to vary with bias voltage, and did not occur at the same conductance values for rupture and contact formation either, this led to speculation in Ref. [32] that they could be attributed to the formation of a magnetic domain wall in the constriction, *even* in the *absence* of an external magnetic field. As we have now seen, DWs are known to affect the resistance of magnetic nanocontacts by up to at most 50% [15,16]. Therefore, it may be possible that the low-conductance peak in the twin-peak histogram of Ni corresponds to the situation where a magnetic domain wall is present in the constriction [32]. The two peaks also appeared to emerge in the presence of an external magnetic field of 5 T [35], which is another strong indication that they may be related to the formation of domain walls, since external magnetic fields are used create domain walls in recent experiments that measure the resistance of ferromagnetic nanocontacts at remanence, i.e., in zero field [16,18].

Note that zero-bias anomalies such as the Kondo resonance [36,37] can be ruled out since they contribute at most $\pm 0.1 G_0$ at rupture, and also occur at the second peak ($\sim 1.5 G_0$), or when there is only a single broad first peak. Thus, Kondo resonances may contribute to broadening of the two peaks, but cannot explain the difference of ~ 0.3 – $0.5 G_0$ between their two centres (at ~ 1.2 and $1.5 G_0$, respectively).

A theory that competes with magnetic DWs leading to twin low-conductance peaks in histograms of Ni, is one where the twin peaks arise from a purely geometric effect. In this theory, either one of two different last-contact structures, e.g., a vertical dimer or a monomer (recall Fig. 2.1), or two different face-centred cubic crystallographic orientations of the Ni nanocontacts, (001) or (111), or a combination of last-contact structure and

crystallographic orientation, give rise to the two low-conductance peaks. In fact, in 2008, Garcia-Mochales *et al.* [40] explicitly proposed such a theory after having performed a statistical analysis of the minimum cross-section of Ni nanocontacts in ensemble rupture CMD simulations along different crystallographic axes of Ni: (001), (110) and (111). They used EAM potentials to describe the interactions between the atoms in their simulations.

In the past, dimers have been shown to occur more often than monomers in CMD simulations of FCC metal contact dynamics [32,40–42,137]. However, in more recent published work, contributing towards this thesis, monomers were found to occur more often in (001)-oriented Au, Ag and Cu nanocontacts in CMD simulations, in agreement with what is expected from experiments on these metals (see Chapter 5, Section 5.1). One might therefore expect the first low-conductance peak of Ni in Fig. 2.2 b) to correspond to a dimer configuration, if it also occurs less often than the monomer as in Au, Ag and Cu, since the twin-peak histogram occurs less often than the one with a single broad first-conductance peak. An experimentalist colleague⁵ has also suggested that (111)-oriented Ni contacts are sometimes pulled off the sample surface in STM experiments, even when the initial indentation into the surface is done very brusquely with the purpose of guaranteeing that mostly (001)-oriented nanocontacts are created. In FCC nanocontacts, (001)-oriented nanocontacts are more favourable in energy terms, since (111) facets form on their oblique sides. For FCC metals, exposed (111) surfaces have the lowest energy of all the low Miller index surfaces [24]. Hence, dimers forming more often in (111)-oriented Ni nanocontacts at rupture, could possibly explain the low-conductance peak in the histogram in Fig. 2.2 b).

Regarding potentials used to model nanocontacts in CMD simulations, as mentioned above, Garcia-Mochales *et al.* used EAM potentials in their simulations of Ni nanocontacts [40]. To the best of my knowledge, no one has ever attempted to study this problem using a modified embedded-atom method (MEAM) interatomic potential [138]. The MEAM potential model represents an improvement over the EAM model, since directionality (covalency) is added to the bonding between the metals. Only Refs. [139,140] used a MEAM potential to describe the interactions between Ni atoms in CMD simulations of

⁵ Private communication with Dr. Carlos Sabater.

nanocontact rupture, in order to compare stress-strain relationships, but not to characterise last-contact structures.

A very recent MEAM potential has been developed for Ni, Fe, Cu and Al [45] that has been fitted to the elastic constants near the melting point of the metals, in addition to being fitted to the melting point temperatures themselves. This means that this potential should describe the plastic deformations that occur in nanocontact rupture particularly well, as they are similar to the disordered boundaries that exist between a molten and perfect crystalline phase of the metal. Another reason for using this particular MEAM potential is that it reproduces the exposed (001), (110) and (111) surface energies of Ni and Fe very well compared to experiment and *ab-initio* calculations.

Presently, MEAM potentials have also only been used to study the stress-strain properties of Fe nanocontacts, inside carbon nanotubes [141–143], in an attempt to explain soldering at the atomic level. However, no reference is made to the type of last-contact structures that form between ruptured Fe tips, or the conductance values they would give rise to.

In this work, the recent MEAM potential referred to above will also be employed to explain the unexpectedly high value of the first conductance peak of Fe in experimental conductance histograms [30,36,37,144]. Recall from Ref. [30] that the first conductance peak in the histogram for Fe constructed from those theoretical calculations, occurred at a lower conductance value than the experimental peak (see Chapter 6, Sec 6.1). According to the authors, this happens because of a fundamental limitation of the EAM potential they used in their ensemble CMD simulations of Fe nanocontact rupture. Upon trying different EAM potentials, similar conclusions were reached.

A possible reason for this is the greater relative covalent bonding in BCC vs FCC metals. EAM interatomic potentials treat the bonding in metals as isotropic. That the 12 first-nearest neighbours of an atom in an FCC metal form essentially equivalent bonds to the central atom, suggests that the bonding is more isotropic compared to BCC metals, where only 8 first-nearest neighbours form more or less equivalent bonds to the central atom. (The bonds are not entirely equivalent due to thermal vibrations at finite temperatures and

magnetocrystalline anisotropy. But, on average, the distribution of valence electrons immediately surrounding a given atom is more directional in the BCC metals.)

For that reason, the discrepancy between the positions of the first peaks in the theoretical and experimental conductance histograms for Fe nanocontacts in Ref. [30], seems to suggest that the explanation may reside in the greater directional character of the bonding in BCC iron. For Ni, on the other hand, a ferromagnetic FCC metal, excellent agreement between theory and experiment is obtained for the conductance histogram with a single broad peak at around $1.5 G_0$.

Vardimon *et al.* [30] also explicitly state that SOC was not included in their conductance calculations and, by the same token, ruled out the effects that magnetic domain walls (DWs) may have on their results. This once more raises the question of whether DWs might not explain the observed low-conductance features of histograms of conductance of Ni and Fe nanocontacts, discussed at length above.

Despite questions arising regarding the role that domain walls can play in enhancing the conductance of iron nanocontacts [145], this possibility will, nevertheless, also be considered in this work. However, fundamentally, the covalent bonding between iron atoms would appear to not favour the formation of single-atom contacts such as vertical dimers and monomers, which are highly favoured in FCC metals such as nickel. Since the EAM potential favours the formation of such single-atom contacts [32,40–42,75], the MEAM potential, which takes directional bonding into account, may produce more realistic last-contact structures for Fe in rupture simulations. Therefore, ensemble CMD simulations of nanocontact rupture, employing both MEAM and EAM potentials, are performed in this work, to compare the stable structures Fe and Ni nanocontacts adopt before breaking.

This concludes the survey of the literature most relevant to the research questions posed in this thesis. In the two next chapters, the standard methods and extensions thereof needed to accurately model metallic nanocontacts are described.

3. OVERVIEW OF STANDARD METHODS

For convenience, the main modelling techniques used in this work are described in this chapter. A basic understanding of these techniques is essential in order to appreciate the developments and results that are presented in subsequent chapters.

Section 3.1 gives an overview of classical molecular dynamics (CMD), which is a well-established simulation technique dating back to the 1950s [146]. More specifically, Sec 3.1.1 describes the embedded-atom method (EAM) formalism, which is a model of reactive bonding between atoms in CMD simulations. It also briefly introduces the modified embedded-atom method (MEAM) formalism in which covalency is added to the isotropic bonding modelled by ordinary EAM potentials. Then, Sec 3.1.2 introduces an attempt to add collinear magnetism to CMD simulations within the EAM formalism.

Section 3.2 develops the more recent idea of spin-lattice dynamics (SLD), which was developed by Dudarev and co-workers in the late 2000s [48]. In the SLD formalism, there is an additional interaction between the atoms that depends on the relative noncollinear orientations of spins, which are treated semi-classically.

Section 3.3 deals with the fully quantum mechanical approach of density functional theory (DFT). Already formulated in the 1960s, by Kohn and Sham [147], DFT is today a widely-used simulation technique that has been considerably refined. Unlike classical molecular dynamics, which does not take into account electrons, DFT has the advantage of producing the full electronic band structure of the modelled materials, although this additional information does come at a much higher computational cost.

Finally, in Sec 3.4, the non-equilibrium Green's function (NEGF) approach, as applied to DFT transport problems, is briefly described. The NEGF formalism is needed to treat out-of-equilibrium quantum mechanical systems, which usually have open boundaries and lack translation invariance. Like DFT, it was formulated in the 1960s, independently by Kadanoff and Bohm [148] and Keldysh [149], respectively.

Since none of the material that is reviewed in this chapter is fundamentally new, readers who are already familiar with the above-mentioned techniques may wish to skip certain sections, or simply proceed directly to the next chapter.

3.1. Classical molecular dynamics

CMD simulations are presently considered a standard method with well defined limitations, applications and validation tools. In the following sections the main aspects of this method are discussed.

The evolution of the atomistic structure of materials is widely modelled by means of CMD simulations, which makes systems involving millions of atoms now accessible [79]. In general, this approach involves solving Newton's second law [150] for each of the particles in the system, as they evolve in time:

$$m_i \ddot{\vec{R}}_i = -\nabla_i V, \quad (3.1)$$

where m_i is the mass of particle i at position \vec{R}_i , and V is the empirical many-body potential energy function. This necessarily requires having a realistic description of the interaction potential V between the particles.

A distinct advantage of CMD simulations over other approaches, such as quantum mechanical molecular mechanics (QM/MM), is that the interaction potential V between the particles is treated semi-classically, and can usually be truncated, e.g., for electrically neutral systems such as metals, at an appropriately chosen cut-off separation between the atoms [146]. The value of the cut-off is usually fixed by fitting the interaction potential to *ab-initio* calculations and experimental properties of the system under consideration [146]. This greatly reduces the computational overhead required to model the system of particles, because the sum over interactions between all particles to calculate the total energy of the system, is limited by the cut-off.

In most applications, CMD models the properties of a macroscopic-sized sample of atomic

and molecular systems. Unfortunately, the choice of boundaries (e.g., fixed or free or periodic) does not guarantee those properties are not affected by the size of the system chosen to represent the macroscopic sample. A standard illustration of the importance of simulation domain size in simulations of a three-dimensional system containing N particles, is that the particles at the surface of the domain number approximately $N^{1/3}$ [146]. Thus, in a simple cubic (SC) lattice with 1000 atoms, with roughly 49% of all the atoms located at the surface, free boundaries will constitute a very bad model of a macroscopic-sized sample [146]. The edge, or finite-size, effects that inevitably results from using free boundaries, are, however, greatly reduced in an SC lattice containing a million atoms, say, since only 6% of the atoms are now located at the surface of the simulation domain.

Periodic boundary conditions therefore offer an appropriate solution to the problem created by free boundaries, because they effectively mimic macroscopic structure. In practice, with periodic boundaries in force, the simulation domain is akin to a primitive cell within an infinite periodic lattice of identical cells (See Fig. 3.1) [146]. The red dotted line in Fig. 3.1 shows that it is important to ensure that periodic images of the atom in the central cell across the infinite simulation domain, do not overlap directly with the atom in the original cell. Otherwise, when a sum over energies is performed to calculate the total energy of the system, its value could become unrealistically large.

Periodic and shrink-wrapped boundaries are used in the CMD simulations in this work. However, overlap between periodic image atoms in contiguous cells or atoms on the opposite sides of central cells are sometimes provoked by the geometries of certain initial structures and actions applied to structures during simulations of nanocontact evolution. LAMMPS provides an easy way to avoid this problem by allowing for the use of shrink-wrapped boundary conditions. Unlike fixed boundary conditions, no atoms are lost when the simulation system crosses the boundary with shrink-wrapped boundary conditions in force. Instead the boundaries move with the simulation system when it exceeds the initial confines of the simulation domain.

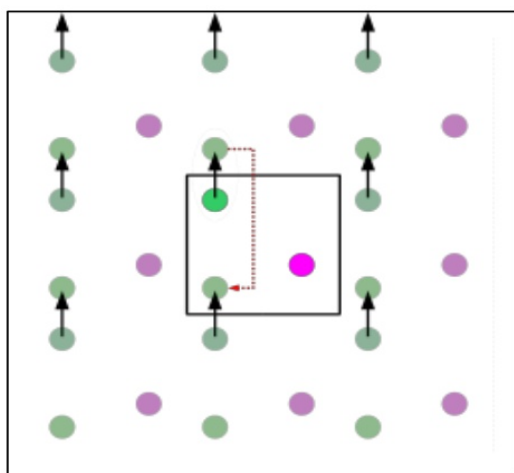


Fig. 3.1: A two-dimensional simulation box containing three atoms (black square in the centre), which, in turn, has been embedded in an infinite two-dimensional lattice via periodic boundary conditions. The small black square encloses the minimum possible cell size that can be repeated in all directions. The red dotted line shows a periodic image from a contiguous cell, of the light green atom in the central cell. The black arrows represent pairwise interactions between atoms in contiguous smallest cells.⁶

3.1.1. The embedded-atom method potentials

There are many systems for which quantum mechanical effects are relatively unimportant, and for which CMD can give surprisingly accurate results. However, in cases where the classical approximation is valid, the success or failure of the method may still rely critically on the accuracy of the interaction potentials that are used in the model.

The class of potentials that can model the atomistic evolution of metallic nanocontacts require the ability to accurately reflect the reorganization and breaking of bonds between metal atoms. Potentials that can model bond making and breaking are referred to as reactive potentials [79]. They can vary in sophistication from the simple embedded-atom method (EAM) potential [31,78,79], used to model the metals in this thesis, to ReaxFF potentials [151], not applied here, which permit chemical reactions involving (originally) hydrocarbons.

In classical molecular dynamics within the EAM formalism, the potential energy of a system of N particles can be expressed as:

⁶ Source: <https://commons.wikimedia.org/wiki/File%3ALimiteperiodicite.svg>.

$$E_{\text{EAM}} = \sum_i^N F[\rho_i] + \frac{1}{2} \sum_{i,j,i \neq j}^N V(r_{ij}), \quad (3.2)$$

where

$$\rho_i = \rho_c \sum_{j \neq i}^{NN} f(r_{ij}), \quad (3.3)$$

and r_{ij} is the distance between particles i and j . $V(r_{ij})$ and $f(r_{ij})$ are the standard pair-wise repulsive and pair-wise density functions within the EAM formalism, respectively [152]. The functional $F[\rho_i]$ in Eq. (3.2) represents the many-body term of the potential, where ρ_i can be interpreted as the electron density at the position of atom i , due to contributions from all neighboring atoms j within a cutoff radius of atom i , and $F[\rho_i]$ itself can be interpreted as the energy required to “embed” atom i in the assembly of atoms j about the position of the former.

The EAM formalism of isotropic bonding between metal atoms provides a very realistic description of the structures adopted by metals, even in nanocontacts at first- and last-contact, as evidenced by the myriad previously reported results (see Refs. [11,17] and references therein). However, isotropic bonding remains a deficiency of the EAM model, and the so-called modified embedded-atom method (MEAM) potential [138] represents an attempt to correct this deficiency by including higher order moments of the electron “density” in the EAM formalism in Eq. (3.3). This approach lends directionality, or covalency, to the bonding between the atoms.

MEAM potentials nevertheless suffer from some of the same drawbacks as EAM potentials, in that they are typically fitted to low temperature properties of the materials they are intended to model, $T = 0$ K for properties obtained in *ab initio* calculations, [45,79]. Recently, a MEAM potential has been developed for Fe, Ni, Al and Cu that has not only been fitted to the melting point of these metals, but also to their near-melting point elastic constants. It thus very accurately reproduces the behaviour of the metals near their melting points [45], such as the interface between the solid and molten phases of a bulk metal. This is useful for the simulations performed in this work, because nanocontacts go through successive cycles of elastic and plastic deformation when they are subjected to

cyclic loading. Of the CMD codes used in this work, the MEAM formalism is only available in the Large-scale atomic/molecular massively parallel simulator (LAMMPS), and will be used to model Ni and Fe nanocontacts, where the difference between directional vs. non-directional bonding may be important.

3.1.2. *Magnetic potentials*

CMD simulations can provide, for example, kinetic and potential energies, atomic stresses and forces, and atomistic (structural) details, but no electric or magnetic properties. However, in 2005, a physically reasonable ‘magnetic’ interatomic potential for CMD simulations of BCC iron was developed by Derlet and Dudarev [153]. It is an EAM-type potential for which ρ_i in Eq. (3.3), assigned to each atom i , determines the magnetic moment ξ_i of atom i , in a similar manner as functionals in DFT depend on the electron density at a given position in the system. We briefly consider the most important aspects here.

Derlet and Dudarev [153] used an approximation of the total energy per atom, E_{tot} , as a function of its atomic magnetic moment ξ ,

$$E_{\text{tot}}(\xi) = F(\xi), \quad (3.4)$$

based on an analogy with the simplest model of the second-order magnetic phase transition: the Ginzberg-Landau model (see Refs. [153,154] and references therein):

$$E_{\text{tot}}(\xi) = E_0 + \alpha \xi^2 + \beta \xi^4, \quad (3.5)$$

where $\alpha < 0$ and $\beta > 0$ are fitting coefficients that depend on the local environment of each atom, and E_0 is the energy of the non-magnetic phase [153,154]. Eq. (3.5) has the shape of a double-well potential with two energy minima. The roots of these minima are equal in magnitude but opposite in sign, and correspond to the equivalent “spin-up” and “spin-down” collinear states in an equilibrium ferromagnetic arrangement [153,154]:

$$\xi_{\pm} = \pm \sqrt{\frac{-\alpha}{2\beta}}, \quad (3.6)$$

The above model inspired Derlet and Dudarev to use an upside-down parabola to approximate the density of states $D(E)$ of the non-magnetic phase near the Fermi energy (centred at zero for convenience). Derlet and Dudarev parameterised $D(E)$ in terms of the d -orbital bandwidth W and two fitting parameters $a > 0$ and $b > 0$ that are independent of W :

$$D(E) = \frac{1}{W} F\left(\frac{E}{W}\right) = \frac{1}{W} \left[a - b \left(\frac{E}{W}\right)^2 \right] + \frac{1}{W} R\left(\frac{E}{W}\right), \quad (3.7)$$

The function F , chosen to be scalable so that $D(E)$ is independent of W , is a sum of parabolic and regular parts [153,154], the latter becoming negligible near the Fermi energy, $E_F \approx 0$, i.e., $|R(0)| \ll a$. The total per-atom energy can also be written as [153]

$$E_{\text{tot}}(\xi) = E_{\uparrow} + E_{\downarrow} - I \xi^2 / 4, \quad (3.8)$$

where I is the Stoner parameter [155] of Fe, and E_{\uparrow} and E_{\downarrow} are the “spin-up” and “spin-down” sub-bands, with their corresponding Fermi energies $\epsilon_{F\uparrow}$ and $\epsilon_{F\downarrow}$,

$$E_{\uparrow} = \int_{-\infty}^{\epsilon_{F\uparrow}} E D(E) dE \quad E_{\downarrow} = \int_{-\infty}^{\epsilon_{F\downarrow}} E D(E) dE. \quad (3.9)$$

When Eq. (3.7) is substituted into Eqs. (3.9), and, the latter, in turn, into Eq. (3.8), it can be seen that for $I > W/a$, Eq. (3.8) has the form of the double-well potential of Eq. (3.5):

$$E_{\text{tot}} = -\text{const} \cdot W + \frac{a}{4} \left(\frac{\epsilon_{F\uparrow} - \epsilon_{F\downarrow}}{W} \right)^2 (W - Ia) + \frac{b}{32} \left(\frac{\epsilon_{F\uparrow} - \epsilon_{F\downarrow}}{W} \right)^4 \left(\frac{4}{3} Ia - W \right) + \dots, \quad (3.10)$$

E_{tot} in Eq. (3.10) has a maximum corresponding to the non-magnetic phase $\epsilon_{F\uparrow} - \epsilon_{F\downarrow} = 0$, while it reaches a minimum when

$$\epsilon_{F\uparrow} - \epsilon_{F\downarrow} = \pm 2W \sqrt{\frac{a}{b} \left(\frac{Ia - W}{\frac{4}{3}Ia - W} \right)}. \quad (3.11)$$

Finally, substituting Eq. (3.11) into (3.10) gives the energy of the equivalent (collinear) “spin-up” and “spin-down” ferromagnetic states of Fe:

$$E_{\text{tot}}|_{\text{min}} = -\text{const} \cdot W + \frac{a^2}{2b} \frac{(Ia - W)^2}{\left(\frac{4}{3}Ia - W\right)} \Theta(Ia - W), \quad (3.12)$$

where $\Theta(x)$ is the Heaviside step function, with $\Theta(x)=1$ on $x > 0$ and $\Theta(x)=0$ otherwise.

It is well-known that the bandwidth W of the d -orbitals of Fe decreases as these orbitals become more localised, i.e., when the interatomic separation between the Fe atoms increases, and/or the coordination about every atom decreases. At the same time, a narrower bandwidth implies a higher density of states at the Fermi level $D(E_F)$ in $3d$ transition metals because the number of electrons in the d -bands must remain conserved. The famous Stoner criterion [155] predicts that if the product of the Stoner parameter I of the $3d$ metal and its density of states at the Fermi energy $D(E_F)$ exceeds unity, the material will be ferromagnetic. One can thus arrive at an expression for the EAM embedding functional $F[\rho_i]$ in Eq. (3.2) if one assumes the bandwidth W is proportional to the function ρ_i representing an effective “electron density”:

$$F[\rho_i] = -A\sqrt{\rho_i} - B \frac{(\sqrt{\rho_c} - \sqrt{\rho_i})^2}{\nu + \sqrt{\rho_c} - \sqrt{\rho_i}} \Theta(\rho_c - \rho_i), \quad (3.13)$$

where A , B and ν are constants, and ρ_c is a critical effective “electron density” below which Fe is ferromagnetic (because the bandwidth is narrower then), while above ρ_c it is non-magnetic (much wider bandwidth).

To avoid the cusp at $\rho \approx \rho_c$ in Eq. (3.13), and thus ensure its first and second derivatives are continuous –in this way meeting the criteria for a second-order phase transition discussed earlier– the following final expression was adopted by Derlet and Dudarev [153,154]:

$$F[\rho_i] = -A\sqrt{\rho_i} - \frac{B}{\ln 2} \left(1 - \sqrt{\frac{\rho_i}{\rho_c}}\right) \ln \left(2 - \frac{\rho_i}{\rho_c}\right) \Theta(\rho_c - \rho_i), \quad (3.14)$$

In CMD simulations using the above potential, the scalar atomic spin magnetic moments of the atoms are defined as [154]:

$$\xi_i = C \left(1 - \sqrt{\frac{\rho_i}{\rho_c}}\right)^\gamma, \quad (3.15)$$

where $C = 2.929\mu_B$ and $\gamma = 0.259$, obtained from a fit of Eq. (3.15) to DFT calculations of the magnetic moment as a function of the volume per atom in bulk iron [154]. The values of C and γ lead to an equilibrium per-atom magnetic moment of $2.154\mu_B$ for bulk BCC iron [154]. The agreement with the experimental value of $2.12\mu_B$ for the spin-only magnetic moment, or in DFT calculations in the local spin density approximation (LSDA), $2.15\mu_B$, are both rather good [63].

3.2. Spin-lattice dynamics

In the last section, it was seen that the magnitude of the magnetic moment of an atom varies depending on its local environment in an assembly of ferromagnetic atoms. Lower coordination about a given ferromagnetic atom leads to greater confinement of its $3d$ electrons, which, in turn, enhances its magnetic moment (more unpaired electrons) because of greater Coulombic repulsion between the electrons.

This simple picture, which is derived from the Stoner formalism discussed in the previous section, is a model of *long-range* magnetism, finding its origin in the interplay between *intra-atomic* exchange and *interatomic* quantum hopping of valence electrons [48]. Both Ni and Fe exhibit long-range magnetism because of their delocalised $3d$ electrons. This fact makes these metals notoriously difficult to model at finite temperatures, even in quantum approaches [54,156–158].

Intuitively, however, the lower coordination of first neighbours (8 of them) about a given

Fe atom in a bulk BCC crystal lattice, implies that there should be less overlap between its $3d$ orbitals than in Ni, which has 12 first neighbours in an FCC crystal [158]. Because the $3d$ electrons should, in the case of Fe, be relatively more localised than in Ni, a model of *localised* interacting magnetic moments, such as a generalised Heisenberg model of ferromagnetic exchange [48–50], may represent a reasonable description of the magnetism in Fe [54,157].

In fact, in a semi-empirical approach, the exchange energy of a weakly-inhomogeneous spin-polarisation density should always be modelled by a Heisenberg Hamiltonian (see Refs. [159–161] and references therein). Furthermore, at 4.2 K, the operating temperature in many STM and MCBJ experiments, longitudinal excitations of the magnetic moments in Fe, i.e., fluctuations in their magnitudes, are far less important than transverse excitations, i.e., precession of the magnetic moments about a local effective magnetic field produced by the moments on neighboring atoms [63,156].

It therefore becomes clear that the Derlet-Dudarev interatomic potential discussed in the previous section, which models collinear magnetism in Fe at 0 K in CMD simulations [48], cannot account for non-collinear spins or how these spins interact locally with each other [48], since they are modelled by an interatomic potential which allows only for spin “up” or spin “down”, and not any other orientation. In addition, the conservation of total angular momentum in ferromagnetic materials and, correspondingly, how energy and angular momentum are dissipated in spin currents, may lead to important technological ramifications in spintronics (See references in Ref. [48]). Conservation of total angular momentum in ferromagnetic materials requires non-collinear spin configurations and coupling between the spin and lattice degrees of freedom [55,56]. Therefore, at least for metals such as Fe, it is necessary to model the evolution of the three Cartesian spin degrees of freedom (S_{ix}, S_{iy}, S_{iz}) of each atom i in so-called spin-lattice dynamics (SLD).

In this regard, a semi-classical exchange model of non-collinear magnetism was implemented for bulk Fe in 2008 by Ma *et al.* [48], and released in 2016 as a freely available spin-lattice dynamics code SPILADY [134]. The exchange parameters used in this model were procured by means of a standard approach followed in spin-polarised DFT, whereby *ab-initio* data are mapped onto classical Hamiltonians, such as a generalised

Heisenberg exchange Hamiltonian [54,63]. The SLD model in Ref. [48] was developed out of interest in the effects lattice vibrations have on the stability of magnetism in FCC versus BCC iron [52,162]. To model such effects, Ma *et al.* added a generalised Heisenberg exchange term to the Derlet-Dudarev potential, $H_{\text{DD}} = E_{\text{EAM}}$ in Eq. (3.2) [48]:

$$H = \sum_i^N \frac{\vec{p}_i^2}{2m_i} + H_{\text{DD}} - \frac{1}{2} \sum_{i,j}^N J_{ij}(r_{ij}) (\vec{S}_i \cdot \vec{S}_j - 1), \quad (3.16)$$

where m_i is the mass, \vec{p}_i is the momentum vector and \vec{S}_i is the spin vector of atom i . The exchange coefficient $J_{ij}(r_{ij})$ of the Heisenberg term in Eq. (3.16) depends explicitly on the interatomic distance r_{ij} as:

$$J_{ij}(r_{ij}) = J_0 (1 - r_{ij}/r_c)^3 \Theta(r_c - r_{ij}), \quad (3.17)$$

where $J_0 = 904.90177$ meV, and the cut-off radius $r_c = 3.75$ Å was chosen to lie between 2nd and 3rd nearest neighbors in BCC Fe [48]. $\Theta(r_c - r_{ij})$ is again the Heaviside step function.

The choice of the simple isotropic function in Eq. (3.17) was motivated by the small effects lattice vibrations have on magnons in BCC iron [52,54], and also by the fact that forces in a molecular dynamics model of spins are calculated as gradients of smoothly-varying continuous functions [51].

More generally, however, the spin-lattice interaction should be expanded in terms that are bilinear in the spins \vec{S}_i and \vec{S}_j of atoms i and j , including $i = j$, and with the atomic coordinates and vector derivatives of J_{ij} , with respect to the coordinates, occurring in increasing order (See Ref. [54]). In such a scheme, the generalised Heisenberg exchange term in Eq. (3.16) corresponds to the zeroth-order term in the bilinear spin expansion. The next-lowest order term, the first-order term of the bilinear expansion, which is not included in Eq. (3.16), contains a sum over all atoms of the dot product of a rank 3 tensor, the gradient of J_{ij} with respect to the position of atom k , and the position vector of atom k [54].

Interestingly, the (anisotropic) off-diagonal elements of the rank 3 tensor in the aforementioned first-order term of the bilinear expansion provides a (non-relativistic) means for the lattice and spins to exchange angular momentum and equilibrate to the same temperature in a simulation in the microcanonical ensemble [54–56]. In the next chapter, it will be shown that the transfer of angular momentum between spin and lattice degrees of freedom, the Einstein-de Haas effect [51,163], can be achieved in SLD simulations of ferromagnetic nanocontacts via the addition of a generalised *uniaxial magnetocrystalline anisotropy* correction [55,56].

The symmetry properties of the tensor in the first-order term, as well as those of higher rank in the higher order terms, of the bilinear expansion, depend crucially on the geometry and symmetry of the systems under consideration. Hence, in Ref. [54], the elements of the rank 3 tensor in the first-order term were only worked out for a dimer, trimer and tetramer of iron atoms, in addition to bulk iron. Repeating such an analysis for an iron nanocontact of arbitrary shape, which evolves dynamically as it stretched or compressed, is well outside the scope of this thesis. Besides, Wang *et al.* showed that although the model of J_{ij} in Eq. (3.17) is too simple [53], $J_{ij}(r_{ij})$ could be represented by a superposition of (isotropic) Bethe-Slater curves.

Finally, returning to Eq. (3.16), note that a term $\frac{1}{2} \sum_{i,j}^N J_{ij}(r_{ij})(1)$ has been subtracted from the spin-dependent generalised Heisenberg exchange term to ensure that the energy and forces are properly defined in the collinear ferromagnetic phase that exists at 0 K [48]. This term represents the ground-state energy of the spin degrees of freedom at 0 K. Additionally, it permits the use of any EAM interatomic potential, not restricted to the Derlet and Dudarev potential.

In this regard, because the EAM potential developed by Malerba *et al.* in Ref. [43] reproduces the energies of exposed (001), (110) and (111) surfaces of Fe better than any of the other potentials, including the Derlet-Dudarev potential, it will be used in the production runs carried out in this work.

The equations of motion integrated during simulations in SPILADY are, written succinctly as,

$$\left\{ \begin{array}{l} \frac{d\vec{r}_i}{dt} = \frac{\vec{p}_i}{m_i} \\ \frac{d\vec{p}_i}{dt} = \vec{f}_i \\ \frac{d\vec{S}_i}{dt} = -\frac{1}{\hbar} \vec{H}_i^{\text{eff}} \times \vec{S}_i \end{array} \right. , \quad (3.18)$$

where $\vec{f}_i = -\nabla_{\vec{r}_i} H$ and $\vec{H}_i^{\text{eff}} = -\nabla_{\vec{S}_i} H$ and H is the Hamiltonian in Eq. (3.16).

It is noted that the sign in the Hamilton's equation, Eq. (3.18), for the force contribution $\vec{f}_i = -\nabla_{\vec{r}_i} H$ from the generalised Heisenberg exchange term in Eq. (3.16) is wrong in many of Ma *et al.*'s works (e.g., Refs. [48,134]). The equations are, however, correctly expressed in e.g., Refs. [49,50,164]. Notwithstanding, the sign of this force contribution has been verified and found to be correct in the SPILADY code itself.

Technical details of the integration procedure and temperature control in SLD simulations is explained at length in Refs. [48,134,165,166]. A more sophisticated integration scheme, the second-order *Suzuki-Trotter decomposition (STD)* of non-commuting operators of spin and lattice coordinates (see Ref. [48,166–168] and references therein), simultaneously conserving the total energy, linear momentum and the spin magnitudes of the atoms for a reasonable trade-off between accuracy and computational efficiency [48,166–168], is used in SPILADY. The default simulation time step in SPILADY is one femtosecond, the same as in LAMMPS.

Finally, the temperature in SPILADY is controlled by a Langevin thermostat (for a very detailed discussion of the implementation thereof, see Ref. [165]). If so desired, two separate thermostats can be used simultaneously to thermalise the lattice and spin degrees of freedom. Further details regarding temperature control will be provided in the next chapter, which deals with adding the effect of spin-orbit coupling to SLD simulations. Thermostatting in LAMMPS is discussed in Chapter 5.

In this work, two different open-source codes are used to model metallic nanocontacts. The first, the Large-scale atomic/molecular massively parallel simulator (LAMMPS) [169], is a

well-established and versatile simulator, which has been used extensively, in combination with EAM potentials, throughout our previous work [23,24,76].

Spin-lattice dynamics, on the other hand, is still in its infancy. So far, it has only been applied to a few, selected, systems [48,49,55,134]. In the present work, SLD is applied for the first time to ferromagnetic nanocontacts. For this reason, a significant portion of the present work is devoted to the extension of the SLD model and validation thereof, as will be explained in detail in the next chapter.

Unfortunately, the MEAM formalism discussed in Sec 3.1.2 is only available in LAMMPS and not SPILADY. Therefore, it is not possible at present to use MEAM potentials of Fe or Ni nanocontacts in recently implemented SLD simulations in LAMMPS [50], since no magnetic anisotropy parameters for these metals were available for LAMMPS at the time of writing of this thesis.

We now turn to discussing how the electronic structure of the solid state is modelled theoretically via density functional theory, which is needed in order to make predictions of experimental conductance values.

3.3. Density functional theory

In order to calculate the electronic transport in nanocontacts in this work, an accurate description of the electronic structure of nanoscopic materials is required. An important example is the linear-combination-of-atomic-orbitals (LCAO) DFT transport calculations of conductance of CMD/SLD snapshots carried out in this work. While structures extracted from CMD/SLD simulations may be used “as is” in most DFT transport calculations of conductance, the simulations may not be sufficiently accurate to predict the bonding strength between atoms in noble-metal nanocontacts made of gold. In such cases, it becomes necessary, at the very minimum, to use plane-wave DFT calculations of the force-extension characteristics of the nanoscopic structures. In simple terms, this latter approach involves calculating the DFT total energy of a nanostructure as a function of interatomic separation along the axis in which the nanostructure is extended adiabatically. This section

discusses the basic theory underlying the powerful materials modelling tool that density functional theory represents.

There is a limit on the number of electrons that can realistically be treated in a many-particle wave-function (MPWF) approach (in practice $\sim 10-10^2$ electrons, at most [170]). That is because an anti-symmetric wave function that is $3N$ -dimensional is needed to describe an assembly of N electrons [171]. Moreover, a large number of parameters is needed to obtain accurate results, even for simple quantities, such as binding energies and bond lengths, when small atomic systems are described by MPWFs [170]. Such limitations led to the development of density functional theory. The basic premise of DFT is that all ground-state quantities of interest for a many-electron system can be expressed explicitly or implicitly as functionals of the position-dependent density of electrons, $\tilde{n}(r)$, instead of a many-electron wave function.

In the section, the Kohn-Sham (KS) self-consistent version of DFT is briefly described because it is the most widely used in practical applications [170,171]. It puts the self-consistent Hartree theory of an assembly of interacting electrons moving in an effective single-particle potential, on an exact footing [170].

In a variational approach, the minimizing electron density $n(r)$, derived from Euler-Lagrange equations, leads to the following set of equations that must be solved self-consistently [170]:

$$\left\{ \begin{array}{l} \left(-\frac{1}{2} \nabla^2 + v_{eff}(r) - \epsilon_j \right) \psi_j(r) = 0, \\ n(r) = \sum_{j=1}^N |\psi_j(r)|^2, \\ v_{eff}(r) = v(r) + \int \frac{n(r')}{|r-r'|} dr' + v_{xc} \end{array} \right. , \quad (3.19)$$

where ψ_j and ϵ_j are the single-particle KS eigenfunctions and eigenvalues (the subscript j represents both spatial and spin quantum numbers), associated with the ground-state electron density $n(r)$. The first two terms in the equation on the third line represent the

electron-ion and electron-electron Coulomb interactions, respectively, and the integral in the second term is evaluated over all space (as are all the other integrals in this section). The third term v_{xc} is the local exchange-correlation potential that is a functional of the whole distribution of electron density functions $\tilde{n}(r)$, with respect to which the exchange-correlation energy E_{xc} is minimized and evaluated at $\tilde{n}(r)=n(r)$ [170].

In practice, Eqs. (3.19) are solved iteratively (self-consistently) by constructing an approximate electron density $n(r)$ using input single-particle atomic or plane-wave orbitals, ψ_j . Then, the obtained electron density is used to find v_{eff} which, in turn, is used to find new ψ_j (and ϵ_j). This process is continued until the change in the ground-state energy, see Eq. (3.20) below, falls below a user-defined threshold, and with the conservation of the total number of electrons, or charge, as constraint.

$$E = \sum_{j=1}^N \epsilon_j + E_{xc}[n(r)] - \int v_{xc}(r)n(r)dr - \frac{1}{2} \int \frac{n(r)n(r')}{|r-r'|} dr' , \quad (3.20)$$

With the exact E_{xc} and v_{xc} , all the many-body interactions in the assembly of electrons are, in theory, accounted for [170], but this remains the central unsolved problem of density functional theory. Currently, only approximations of E_{xc} , and, by extension, v_{xc} , of increasing sophistication and realistic physical content, exist [171].

The most widely used and successful approximations of $E_{xc}[n(r)]$ can be expressed in a near-local form [170]:

$$E_{xc}[n(r)] = \int e_{xc}(r;[n(\tilde{r})])n(r)dr , \quad (3.21)$$

where $e_{xc}(r;[n(\tilde{r})])$ is an exchange-correlation energy per particle at position r . It is also a functional of the electron density at a point \tilde{r} that is near r , such that they are about a distance of the local Fermi wavelength, λ_F , apart [170]. The most well-known and widely used form of $e_{xc}(r;[n(\tilde{r})])$, especially for solids, is the so-called local density approximation, in which $e_{xc}(r;[n(\tilde{r})])$ is the energy/particle of a uniform electron gas

whose density varies slowly on the scale of the local Fermi wavelength λ_F . The LDA approximation is especially successful at predicting the equilibrium geometries and lattice parameters of most systems for which the electron gas can be treated, at least initially, as a slowly-varying density $n(r)$. For the purposes of this thesis, the LDA, and also so-called generalised gradient approximation (GGA), discussed next, have been employed. However, both fail in systems where electron-electron interactions are very strong, such as in Heavy Fermion compounds [170].

As a result of the combined effect of the Pauli exclusion principle and electron-electron repulsion, an electron at position at r will be screened from all the other electrons, which, in turn, means that the electron density $[n(\tilde{r})]$ at position \tilde{r} , near r , is effectively “shortsighted” [170]. The electron density at \tilde{r} can therefore be expanded about r in a Taylor series in moduli of the gradients of the electron density at r . The generalised gradient approximation (GGA) referred to above is thus obtained by expressing e_{xc} in Eq. (3.21) as a function of $n(r)$ and $|\nabla n(r)|$. Using GGA instead of LDA reduces errors for, e.g., atomization energies [170], and the magnetic moments and lattice parameters of ferromagnetic metals [63].

So far, we have only dealt explicitly with DFT for non-magnetic materials. The spin-polarised extension of KS DFT involves the construction of a determinant from N fictitious single-particle spin orbitals, for a system of non-interacting electrons with spin densities n_\uparrow , the 3-dimensional density of all “spin-up” electrons, and n_\downarrow , the 3-dimensional density of all “spin-down” electrons, where the overall density of the entire system is given by $n = n_\uparrow + n_\downarrow$ [171]. The difference between these two densities is then referred to as the spin-polarisation density [171]. In this formulation of DFT, also called “one-component”, “collinear”, or “spin-free” [171], the direction of the spins are fixed along an arbitrary quantisation axis, usually chosen to be the z -axis. In an actual spin-polarised calculation, the spin orbitals are products of spatial and spin kets, but the spatial part of a “spin up” orbital is not necessarily the same as that of a “spin down” one. Conversely, in a calculation with no spin polarisation, also referred to as “spin-restricted”, the spin orbitals are also a product of spatial and spin kets, and share the same quantisation axis too, but now the spatial part of occupied, and paired spin-up and -down orbitals, is the same [171].

To treat the non-collinear spin textures that are generated in the SLD simulations in this work, it is necessary to resort to the “two-component”, vector-relativistic formulation of DFT, in which a single-particle orbital can be expressed as a linear combination of “spin-up” and “spin-down” orbitals with angular momentum $j = l \pm \frac{1}{2}$, with the positive sign corresponding to “spin-up”, and the negative sign to “spin-down” electrons [171]. For more details, we refer the reader to the review of magnetism in DFT in Ref. [63].

In non-collinear DFT, each single-particle orbital has a spin that can point in any direction in space, and all such spins need not point in the same direction either. In the two-component formalism, the definition of the spin polarisation density is based on the magnitude of the spin magnetisation vector, as opposed to the definition in the one-component or collinear formalism where it is the projection of this vector onto the z -axis. Therefore, the spin polarisation vector becomes invariant to rotations in the space of the spins in a non-collinear formalism [171].

Finally, the distinguishing characteristic of the non-collinear formalism is that, in practice, the off-diagonal blocks of the $2N \times 2N$ spin-density matrix become populated when the two spin densities in the collinear formalism mix. Here, N represents the number of spatial single-particle orbitals or kets. This also means that the spin-density functional depends on the off-diagonal elements. Furthermore, the spatial part in a non-collinear calculation is, in general, complex [171].

Any approach to solving the electronic structure of a material, requires a basis set in terms of which the wave functions have to be expanded. There are many categories of DFT calculation that employ, for example, Gaussian (*linear combination of atomic orbital* – LCAO) or plane-wave basis sets, or combinations of these, to treat systems such as solids, exposed surfaces or isolated molecules [171]. The calculations can be further divided into all-electron or effective core potential (ECP, also known as pseudopotential). In the latter case, the core electrons are replaced by benchmarked ECP potentials [172], which in many cases are freely available online (along with their corresponding basis sets in the case of LCAO DFT codes).

Plane-wave DFT codes employ periodic boundary conditions, via Bloch’s theorem, in

calculations involving solids, which some of the LCAO codes also do, e.g., CRYSTAL14 [173] and OpenMX [62,174,175]. Periodicity leads to the existence of a reciprocal space (k-space), which requires sampling of the Brillouin zone of k-space. Periodic boundary calculations are not limited to solids, since surfaces can be treated by the so-called supercell approach, where more than one k point is sampled only in the periodic dimensions of the system, and vacuum slabs are used in the non-periodic dimensions in order to avoid interactions between the system and its periodic images in those dimensions. This also means that only one k point in the Brillouin zone, the Gamma point, is sampled in supercell calculations on isolated molecules and other non-periodic clusters.

Below follows a very brief description of the DFT codes employed in this work:

It is a standard practice to first obtain a converged DFT solution for a nanocluster, such as a snapshot extracted from CMD/SLD simulations, before performing an open-boundary DFT calculation of the electronic transport within the non-equilibrium Green's Function (NEGF) approach [176]. Therefore, the workhorse for the majority of the DFT quantum transport calculations performed towards this thesis, is ANT.Gaussian [68]. It interfaces seamlessly with the DFT code Gaussian [177], which, as its name implies, uses Gaussian atomic basis sets (discussed in a little more detail in the next chapter). The CMD/SLD nanocontacts in this work technically constitute non-periodic nanoclusters in ordinary DFT calculations, and hence, Gaussian, most widely used for isolated molecules, is very appropriate for handling them.

We also note that Gaussian does support periodic boundary conditions, but above all, that the range and quality of the optimised basis sets, ECPs and density functionals available in this DFT code [171], is reflected by its widespread use in the quantum chemistry literature.

OpenMX [62], also a LCAO DFT code, uses numeric pseudo-atomic orbitals (PAOs) instead of Gaussian basis functions. It is vector-relativistic, possessing a constrained non-collinear magnetism capability [63] that permits the use of spin textures, along with the atomic structures, generated in, for example, SLD simulations, as input to calculations.

As for the plane-wave codes used to calculate force-extension characteristics of monatomic

chains in this work, CASTEP solves a set of single-particle KS equations in the pseudopotential approach, by expanding wavefunctions in a set of plane waves based on periodic boundary conditions and Bloch's theorem [64]. *Ab-initio* pseudopotentials of the norm-conserving and ultrasoft variety describe the electron-ion potential in CASTEP [64]. In this work, on-the-fly-generated (OTFG) ultrasoft pseudopotentials are used in CASTEP [178].

Very accurate DFT calculations can be performed by using the full-potential linearised augmented plane wave (FP-LAPW) approach. Full-potential refers to the fact that all the electrons, core and valence, are included in the “active space” of the calculation. In the FP-LAPW method, a spherical harmonic basis set is used inside of atomic spheres, because wave functions are rapidly varying and atomic-like here, while a plane-wave expansion is used in the interstitial regions between atoms, because in this second region, wave functions are more smoothly varying and not atomic-like. The other DFT code used in this work to calculate the force-extension characteristics of monatomic wires, is Wien2K [65,179], a code that uses the FP-LAPW approach.

More details of the DFT codes used in this work will be discussed in the chapters where production results on nanocontacts are presented. In the following section, we see how DFT can be combined with non-equilibrium Green's Functions to calculate the electronic transport of nanocontacts.

3.4. Non-equilibrium Green's Function DFT quantum transport

In this work, a LCAO DFT approach is used to obtain the converged Hamiltonian $[H]_{\sigma'\nu}^{\sigma i \mu}[n(r)]$ of the nanocontacts extracted from CMD/SLD simulations. As explained in the previous section, this Hamiltonian is the result of a DFT total energy calculation on an isolated nanocluster. The Hamiltonian $[H]_{\sigma'\nu}^{\sigma i \mu}[n(r)]$ depends on the minimizing electron density $n(r)$ of the cluster, where i and j denote atomic positions on which single-particle “orbitals” μ and ν , used to calculate $n(r)$, are centred, and σ and σ' correspond to up and down spins, respectively, in the effective “one-component” Kohn-Sham (KS) formalism described in the previous section.

Since the electronic transport is calculated in a post-processing step from $[H_{\sigma'j\nu}^{oi\mu}[n(r)]]$, and its properties are, in turn, determined by the disordered atomic cluster extracted from the CMD/SLD simulations, it is very important to use an *ab-initio* approach that can handle disorder and charge transfer correctly, because every atom “counts” in the cluster [2,180]. The one-component KS formalism described in the previous section produces a single-particle Hamiltonian with electron-electron interactions taken into account at a static mean-field level [180], providing a reliable description of the electronic structure of the disordered clusters obtained from CMD/SLD simulations.

In such a calculation, when the set tolerance in total energy and root-mean square deviation in the (spin) density matrix is reached, two semi-infinite leads are attached to the contact, in a typical two-terminal configuration (see Fig. 1.1). This converts the problem from one in which the system is an isolated cluster or a cluster surrounded by vacuum slabs in a periodic supercell approach, to one with open boundaries, i.e., infinite in extent and devoid of translational invariance [180].

In this configuration, ordinary DFT is no longer applicable, and the expanded system of Lead-Device-Lead is best treated by a combination of the partitioning approach, described below, and either a complex band-structure approach (see Refs. [17,181] and references therein), typically used in plane-wave DFT codes such as Quantum ESPRESSO [182], or, a non-equilibrium (single-particle) Green’s function (NEGF) approach [68,183,184], typically implemented in atomic-basis set (LCAO) DFT codes such as ANT.Gaussian and OpenMX.

In the partitioning method [180], the two-terminal system of coupled device and leads is divided into left lead (L), device (D) and right lead (R). The converged Hamiltonian from the previous DFT step corresponds to the device and is denoted by H_D . The Hamiltonian for the overall system H can then be represented in matrix form as

$$H = \begin{pmatrix} H_L & H_{LD} & 0 \\ H_{DL} & H_D & H_{DR} \\ 0 & H_{RD} & H_R \end{pmatrix}, \quad (3.22)$$

Note that in Eq. (3.22) it is implicitly assumed that there is no interaction between the left and right leads.

Because the basis sets used in DFT calculations are not always orthogonal, for example, in Gaussian DFT calculations, it is also necessary to take into account overlap between KS single-particle orbitals on the same and different atoms. This is expressed by the following matrix:

$$S = \begin{pmatrix} S_L & S_{LD} & 0 \\ S_{DL} & S_D & S_{DR} \\ 0 & S_{RD} & S_R \end{pmatrix}, \quad (3.23)$$

The single-particle Schrodinger equation for a system of more than one atom with Hamiltonian H , and overlap between orbitals on the same and different atoms represented by the matrix S , can be expressed as a matrix equation that has a Green's function matrix as solution when the inhomogeneity on the right side of the equation is the identity matrix:

$$(zS - H)G(z) = 1, \quad (3.24)$$

where, generally, z is a complex number, and 1 is the identity matrix.

Equation (3.24) can be understood using a familiar example from undergraduate quantum mechanics. In elementary treatments of quantum mechanical scattering between two particles in the laboratory frame of reference, where one particle impinges on another from negative infinity, the system has open boundaries and no translational invariance, and the traditional route of solving the Schrodinger equation resorts to treating the scattering centre as an inhomogeneity, or source term. This opens the way for making use of a Green's function to solve the problem, since it constitutes the solution to the inhomogeneous Schrodinger equation when the inhomogeneity is a delta function [185]. In a similar way, the single-particle Green's function in Eq. (3.24) can be defined as a quantum mechanical operator that solves the single-particle Schrodinger equation for scattering from a generalised potential, such as the potential that a nanocontact represents, when its narrowest width or cross-section is comparable to the Fermi wavelength of the electrons that impinge on the constriction [186].

Now, by the partitioning method (see Ref. [180] and references therein), the Green's

function of the *device* region can be obtained as

$$G_D(z) = (zS_D - H_D - \Sigma_L(z) - \Sigma_R(z))^{-1}. \quad (3.25)$$

In Eq. (3.25), Σ_L and Σ_R are needed to account for the coupling of the device to the semi-infinite left (L) and right (R) leads. They are referred to as self-energies, and can be calculated from the Green's function matrices $g_\alpha(z) = (zS_\alpha - H_\alpha)^{-1}$, $\alpha = L, R$, when the leads are treated in isolation [180]:

$$\Sigma_\alpha(z) = (zS_{D\alpha} - H_{D\alpha})g_\alpha(z)(zS_{D\alpha}^\dagger - H_{D\alpha}^\dagger). \quad (3.26)$$

In ANT.Gaussian, the leads are constructed as so-called Bethe Lattices or Cayley trees [187,188]. Bethe lattices branch outward like a tree from a given atomic centre based on its coordination with nearest-neighbour atoms as well as the distances between it and those atoms. These lattices do not reproduce (closed) long-range bulk symmetry, but the local symmetry about each atomic centre mimics the correct parent lattice structure. ANT.Gaussian builds these lattices from the atoms in the frozen ends of the CMD/SLD-extracted nanocontacts (recall that the frozen ends have perfect parent crystal symmetry, see Sec 3.1.2), and the self-energies and Green's functions of the leads in Eqs. (3.25) and (3.26) are calculated by a parameterised tight-binding approach, using two-centre Slater-Koster parameters [189].

As pointed out in Ref. [180], the density of states, charge, spin-densities, current I , zero-bias, as well as differential, conductance $\frac{dI}{dV}$, i.e., quantities of interest for making comparisons with experiment, can be calculated from the Green's function matrix G_D of the *device* and the self-energies Σ_L and Σ_R of the bulk leads.

The main quantity of interest in the DFT quantum transport calculations performed on nanocontacts extracted from CMD/SLD simulations in this work, is the zero-bias conductance. It can be derived from the widely-known Landauer formula [190] for the steady-state current I through a nanocontact, with a bias voltage V applied across its

bulk leads:

$$\begin{aligned}
I(V) &= \frac{2e}{h} \int [f(E-\mu_L) - f(E-\mu_R)] T(E) dE \\
&= \frac{2e}{h} \int_{\mu_R}^{\mu_L} T(E) dE
\end{aligned}
\tag{3.27}$$

where the Fermi-Dirac statistical distributions $f(E-\mu_L)$ and $f(E-\mu_R)$ have been evaluated at *zero* temperature (the KS DFT formalism is used to obtain the converged device Hamiltonian H_D), and μ_L and μ_R are the chemical potentials (the energy required per electron to add one additional electron to the electron reservoir deep in the bulk of the electrodes), of electrons in the left and right leads, respectively. The chemical potentials can be expressed as $eV = \mu_L - \mu_R$ in terms of the applied bias voltage V . In this *non-equilibrium* situation, the chemical potential of lead L has been assumed to be higher than that of lead R, since electrons, being negative, move from a higher electrostatic potential, and hence chemical potential, to a lower one [180]. The factor 2 comes from spin degeneracy and the fact that we are, for the sake of argument, considering a closed-shell (spin-unpolarised) DFT calculation here.

Then, in Eq. (3.27), the transmission function $T(E)$ is the quantity that is calculated from the zero-temperature Green's function matrix G_D of the *device* and the self-energies Σ_L and Σ_R of the bulk leads, according to (see Ref. [180] and references therein)

$$T(E) = \text{Trace} \left[\Gamma_L(E) G_D^{(-)}(E) \Gamma_R(E) G_D^{(+)}(E) \right],
\tag{3.28}$$

where $G_D^{(\pm)}$ are the retarded (−) or advanced (+) Green's function of the device region $G_D^{(\pm)}(E) = \lim_{\eta \rightarrow 0^+} G_D(E \pm i\eta)$, used to circumvent poles at eigenvalues of the device Hamiltonian H_D on the real energy axis [185], i.e., in the integration over the energy, as in Eq. (3.27). Also, $\Gamma_\alpha(E) = i(\Sigma_\alpha^{(+)}(E) - \Sigma_\alpha^{(-)}(E))$, with $\alpha = L, R$, are matrices that take into account the coupling between the device and bulk leads in the calculation of the transmission function in Eq. (3.28). The $\Sigma_\alpha^{(\pm)}$ are defined in analogous fashion to the retarded (−) and advanced (+) Green's functions, i.e., $\Sigma_\alpha^{(\pm)}(E) = \lim_{\eta \rightarrow 0^+} \Sigma_\alpha(E \pm i\eta)$.

Finally, when $\mu = \mu_L \simeq \mu_R$, i.e., at zero bias and temperature, the conductance $G = I/V$

across the nanocontact reduces from Eq. (3.27) to

$$G = \frac{2e}{hV} \int_{\mu_R}^{\mu_L} T(E) dE \simeq \frac{2e^2}{h} T(\mu), \quad (3.29)$$

where we have used the fact that $eV = \mu_L - \mu_R$.

In summary, to calculate the zero-bias conductance of a nanocontact snapshot extracted from an SLD or CMD simulation, it suffices to calculate the transmission function at the common chemical potential μ of the two bulk leads. For greater detail of the implementation of the NEGF formalism in the codes ANT.Gaussian and OpenMX, used in this thesis to calculate zero-bias conductance, the interested reader is referred to Refs. [68,180,188,191] and Ref. [184], respectively.

The next chapter discusses extensions and modifications of the CMD, SLD and DFT quantum transport methods in order to reproduce experimental cyclic loading of nanocontacts in CMD and SLD, and take the effects of spin-orbit coupling into account in more accurate models of ferromagnetic nanocontacts in SLD and DFT transport calculations.

4. EXTENSIONS OF STANDARD METHODS AND PRELIMINARY COMPUTATIONAL RESULTS

Chapter 4 looks at key modifications to the methods discussed in the last chapter, needed to accurately model nanocontacts.

Section 4.1 describes the algorithm implemented in CMD and SLD to emulate cyclic loading in the experiments.

Then, Sec 4.2. discusses extensions to SLD simulations. Section 4.2.1 shows how spin-orbit coupling has been incorporated in SLD simulations via magnetocrystalline anisotropy, and presents results reproduced from the literature to validate the approach. Section 4.2.2 subsequently discusses how the results of Sec 4.2.1 can be used to model non-collinear spins of ferromagnetic nanocontacts in SLD simulations.

Finally, Sec 4.3 deals with vector-relativistic DFT transport calculations. Section 4.3.1 details how SOC has been introduced in ANT.Gaussian, and presents test calculations to validate the implementation. Sec 4.3.2 explains how non-collinear magnetism has been included in ANT.Gaussian via a unitary transformation of the spins.

4.1. Emulating the experiments: cyclic loading

In Sec 1.1, the operating principle of the STM and MCBJ techniques were discussed. In particular, it was pointed out that contact could be repeatedly broken off and re-established in these techniques, via cyclic loading of the contacts. We have shown in the past that this is, in fact, an important point to take into account when doing simulations since it gives rise to more stable and reproducible structures [130]. We developed a method to mimic this experimental setup [12,42,130,192], unlike work done by other authors, where only individual and independent contacts are considered [19,40,41,74,75]. This method implies making use of the algorithm proposed by Bratkovsky *et al.* [193], to model controlled cyclic loading of the nanocontacts [42,130,192]. In the present work, the algorithm and

methodology has been implemented in both LAMMPS and SPILADY, which, in the latter case, allows us to do cyclic loading at the same time that the dynamics of the spins are followed.

In order to perform cyclic loading in simulations, special boundary conditions are required. It is assumed that the ends of the nanocontacts are connected to an infinite bulk. In practice, this involves freezing 2-3 layers of atoms (and spins in SLD simulations, see the next section), at the top and bottom of the nanocontacts (see Fig. 4.1). The frozen layers are subsequently displaced in opposite directions at a constant speed of ~ 1 m/s, which is similar to previous work in the field [192]. The remaining atoms (and spins) respond to the motion of the frozen layers and each other. Most simulations are started from an ideal contact with atoms occupying positions they would in an infinite perfect lattice (see Fig. 4.1 a)), while, in SLD simulations, all the spins are oriented along a fixed axis of the parent crystal structure, e.g., the positive z -direction (along the axis of the nanocontact), in the case of, e.g., BCC iron.

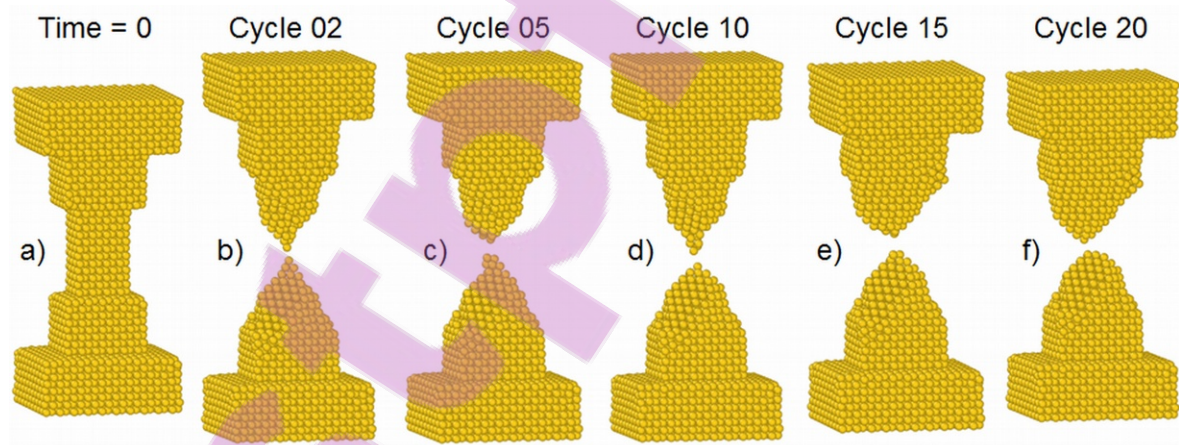


Figure 4.1: Cyclic loading of a notched Au(001) nanocontact at 4.2 K, to a contact depth of 5 atoms in the minimum cross-section: a) at time = 0 in the simulation and b) – f) immediately after rupture during cycles 2, 5, 10, 15 and 20, respectively.

It is important to calculate the cross-section of the nanocontact in simulations in order to model the repeated stretching and compressing of nanocontacts over many cycles in the experiments [130]. However, no unambiguous definition of the minimum cross-section

exists [30]. In this work, we use the approach in Refs. [41,193] to determine the minimum cross-section:

The z -coordinates of the atoms in the outermost frozen layers on opposite ends of the nanocontacts are determined by a standard algorithm which searches for minima and maxima. Then, the length of the nanocontact is calculated by subtracting the minimum from the maximum z -coordinate. Following, all atomic z -coordinates are taken relative to that of the bottom-most layer. The nanocontact is then divided into overlapping horizontal slabs of thickness equal to 2.1 times the radius of the atoms such that the overlapping slabs are displaced by a 10^{th} of an atomic radius along the z -direction from the previous slab. (The atoms are assumed to have a spherical volume of radius equal to its value in a close-packed lattice of the metal: FCC or BCC in this work.)

Starting from the bottom of the nanocontact, and moving up a tenth of a slab thickness at a time [41], the volume of atoms in each overlapping slab is calculated progressively, by assuming that an atom lies completely within a given slab if its z -coordinate is a vertical distance, equal to or smaller than the radius of the atom, from the top and bottom faces of the slab in question. The volumes of atoms that straddle two adjacent slabs are calculated from the formula:

$$V_{\text{partial}} = \frac{\pi}{3} h^2 (3r_0 - h), \quad (4.1)$$

where h = is the height of a partially filled sphere, calculated as the difference of the atom's z -coordinate (at the atom's centre) and the coordinate of the face of the horizontal slab closest to it within the slab, i.e., the face it straddles, and $r_0 = \sqrt[3]{\frac{3}{4\pi} V}$ is the radius of an atom of volume V . This latter volume is, in turn, calculated from the packing fraction of atoms in a conventional unit cell of the (FCC or BCC) metal crystal.

Once the volumes of all the atoms in every overlapping horizontal slab along the length of the contact have been determined (recall that we step vertically through the contact a tenth of the slab thickness at a time), the minimum cross-section of the contact can be found by identifying the slab of smallest volume, and dividing its volume by the constant thickness

of the slabs.

The above algorithm has been implemented in SPILADY by adding a new C++ module to its source code. In LAMMPS, PYTHON code is called from within the LAMMPS input script when the minimum cross-section of the nanocontact is requested. Typically, this is done every 10 picoseconds during a LAMMPS/SPILADY simulation, to, in particular, give the contact enough time to fully rupture under stretching, when the minimum cross-section gets below a small predefined threshold value. The algorithm that calculates the minimum cross-section is not infallible, and contact sometimes, but usually very seldomly, persists even after the minimum cross-section has fallen below the threshold. Allowing the stretching to continue a few picoseconds longer ensures that rupture is always complete. The motion of the frozen ends is reversed at this point in order to bring the two ruptured fragments back into contact, once more, up to a predefined value of the minimum cross-section. Recall that this process of repeated and controlled rupture and contact formation is referred to as cyclic loading.

Finally, we note that the Derlet-Dudarev interatomic potential discussed in Sec 3.1.2 was originally developed to model point and extended defects in bulk iron [153]. Here, for the first time, it is applied in the study of cyclic loading of nanocontacts. In LAMMPS, it has been necessary to modify the source code slightly to calculate and output the magnetic moments of all the atoms along with their positions during cyclic loading (see Fig. 4.2 below). This is because the variables ρ_i , needed to calculate ξ_i in Eq. (3.15), are normally inaccessible at run-time in LAMMPS, since they are treated as internal variables.

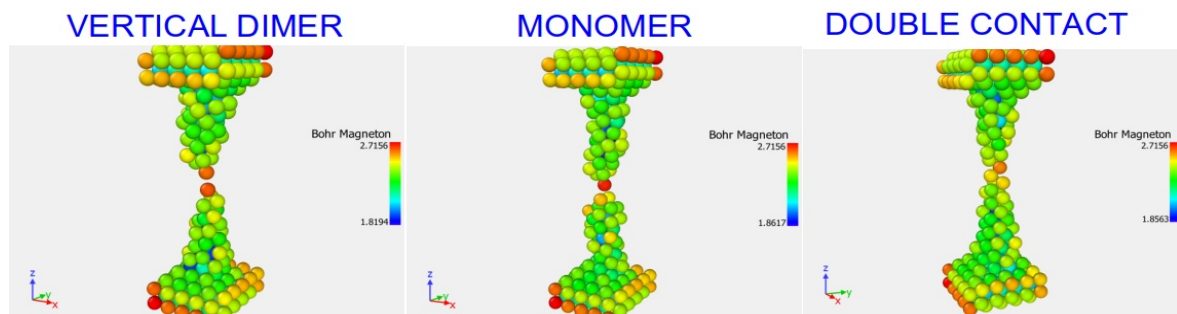


Fig. 4.2: The three most-likely last-contact structures obtained during cyclic loading of a 308-atom (001)-oriented BCC iron nanocontact at 4.2 K. Depending on the coordination about each Fe atom in the structure, the magnitudes of the atomic magnetic moments, calculated from Eq. (3.15), vary between ~ 1.8 and $\sim 2.7 \mu_B$ (see color legend at right in each panel).

4.2. Spin-lattice dynamics with spin-orbit coupling

The original SLD algorithm in SPILADY suffers from an important shortcoming. The spatially isotropic generalised Heisenberg potential in Eq. (3.16) cannot account for magnetic anisotropy, an effect that finds its origin in spin-orbit coupling [55,56,194]. This becomes evident even in finite-temperature simulations of bulk iron.

When only the lattice degrees of freedom are thermalised using the lattice Langevin thermostat, the spin temperature remains zero even though the spin degrees of freedom are coupled to the lattice through the separation-dependent exchange coefficient $J_{ij}(r_{ij})$ in Eq. (3.17). The spin temperature remains zero because the isotropic $J_{ij}(r_{ij})$ factor does not permit conservation of total angular momentum in the system. Therefore, no demagnetisation as a result of the finite temperature occurs, and the ratio of magnetisation to saturation magnetisation remains unity ($M/M_s=1$) [55,56,194]. In other words, there exists an “entropic barrier” between the lattice and spin degrees of freedom [55], because they cannot exchange angular momentum.

To remedy the aforementioned problem, the authors of Ref. [55] realised that a key ingredient was missing: SOC, which couples the spins to the lattice. Since SOC cannot be included directly in CMD simulations, due to the obvious lack of electrons in classical “ball-and-stick” simulations, they instead suggested including magnetic anisotropy, the manifestation of spin-orbit coupling in a crystal lattice, by adding another appropriately defined spin- and lattice-dependent term to the Hamiltonian.

4.2.1. Uniaxial magnetic anisotropy

The proposed magnetic anisotropy term needs to be at least quadratic in the spin degree of freedom, i.e., uniaxial magnetocrystalline anisotropy, to ensure that no term of the spin Hamiltonian undergoes a sign change under time-reversal in the absence of an external magnetic field [153]:

$$\mathbf{H}_{\text{anis}, 2, i} = -C_2 \sum_i^N \vec{\mathbf{S}}_i \cdot \Lambda_i \cdot \vec{\mathbf{S}}_i, \quad (4.2)$$

where C_2 is a constant of magnitude $\sim 10^{-1}$ eV [55], $\vec{\mathbf{S}}_i$ is the spin of atom i , and Λ_i is the Hessian matrix $\left[\frac{\partial^2 f_i(r_{ij})}{\partial x_{i\alpha} \partial x_{i\beta}} \right]$ ($\alpha, \beta = 1, 2, 3$) with respect to atom i , of a function $f_i(r_{ij})$, which, by analogy with the effective “electron density” function in the EAM formalism, takes the asymmetry of the local environment of atom i into account via a sum over pairwise contributions $\phi_{ij}(r_{ij})$, from neighboring atoms j , within a cutoff radius r_c from i :

$$f_i(r_{ij}) = \sum_{j \neq i} \phi_{ij}(r_{ij}) = \sum_{j \neq i} \begin{cases} (1 - r_{ij}/r_c)^4 \exp(1 - r_{ij}/r_c), & r_{ij} \leq r_c \\ 0, & r_{ij} > r_c \end{cases}, \quad (4.3)$$

where $r_c = 3.5$ Å was chosen for BCC Fe (between 2nd and 3rd nearest neighbors) [55]. The fourth-order polynomial in Eq. (4.3) was chosen to guarantee that the interatomic forces due to Eq. (4.2) go to zero smoothly at r_c [55].

Since the magnetic anisotropy in Eq. (4.2) is uniaxial, when $C_2 > 0$, the spins will tend to align along the axis of axial symmetry, e.g., the length of an elongated nanocontact, or perpendicular to this axis when $C_2 < 0$. In this work we assume $C_2 > 0$ since uniaxial anisotropy is positive for many materials that assume a *hexagonal close-packed* (HCP) crystal structure possessing a single high-symmetry axis, i.e., along the c axis [195]. Obtaining an exact value for C_2 is also extremely difficult, since a very careful DFT calculation of the vibrational breaking of local symmetry in bulk Fe, employing large a 128-atom supercell, only managed to yield an order of magnitude estimate for this constant: $\sim 10^{-1}$ eV (see Ref. [55] and references therein).

Uniaxial magnetocrystalline anisotropy, which corresponds to the second-order term in the expansion of the magnetocrystalline anisotropy energy (MAE) [56], cannot predict the easy or hard magnetisation axes in cubic metals such as BCC iron or FCC nickel. The lattice of a cubic metal has more than one high symmetry axis and requires at least a fourth-order first term in the expansion of the MAE to correctly predict the metal’s

preferred magnetisation axes [51]. However, since the Fe and Ni nanocontacts in this work have roughly axial symmetry, they have a well-defined single high-symmetry axis, and the above approach thus constitutes a reasonable first-order approximation with which to describe magnetocrystalline anisotropy in ferromagnetic nanocontacts.

On the other hand, in the scanning tunnelling microscopy (STM) and mechanically controllable break junction (MCBJ) experiments in which ferromagnetic nanocontacts are fabricated under conditions of cryogenic vacuum, the contacts are attached to bulk electrodes in a two-terminal configuration (recall Sec 1.1 for a brief description of the two experimental techniques). The spins are therefore frozen in the direction of the long axis in the ends of the model nanocontacts considered in this work (see Fig. 4.7 in Sec 4.2.2.).

Since magnetic anisotropy is not yet available in SPILADY, and until very recently, neither ordinary SLD, nor SLD with magnetic anisotropy, was available in LAMMPS [50], SPILADY's source code has been modified in this work to perform cyclic loading on ferromagnetic nanocontacts in which the effects of SOC are taken into account through the uniaxial magnetic anisotropy term in Eq. (4.2). This term is a *dynamic* magnetic anisotropy correction that arises because of a deviation of the environment of each spin from what it would “see” in a perfect BCC lattice of Fe. The background (static) magnetic anisotropy that exists in real Fe crystals has, as in Ref. [55], not been included in this work. The aforementioned boundary conditions of frozen spins effectively impose a background magnetisation easy axis on the nanocontacts in our SLD simulations (see Fig. 4.7 in Sec 4.2.2).

Note that, because it does not obey time-reversal symmetry in the absence of an external field, the other anisotropy correction in Refs. [55,56,194], which is first-order in the spin

\vec{S}_i of atom i , $H_{\text{anis},1,i} = -C_1 \sum_i^N \vec{K}_i \cdot \vec{S}_i = -C_1 \sum_i^N \nabla_{\vec{r}_i} [f_i(r_{ij})] \cdot \vec{S}_i$, has not been included in this work either.

In its original form, Eq. (4.2) is not amenable to numerical implementation. Therefore,

based on the realisation that $\left[\frac{\partial^2 f_i(r_{ij})}{\partial x_{i\alpha} \partial x_{i\beta}} \right] = \nabla_{\vec{r}_i} \left[\nabla_{\vec{r}_i} f_i(r_{ij}) \right]$, it can be rewritten as:

$$\mathbf{H}_{\text{anis},2,k} = -C_2 \sum_{k=1}^N \sum_{j \neq k} \left[g(r_{kj}) \vec{\mathbf{S}}_k \cdot \vec{\mathbf{S}}_k + g(r_{jk}) \vec{\mathbf{S}}_j \cdot \vec{\mathbf{S}}_j + \frac{1}{r_{kj}} \frac{dg(r_{kj})}{dr_{kj}} (\vec{\mathbf{r}}_{kj} \cdot \vec{\mathbf{S}}_k) (\vec{\mathbf{r}}_{kj} \cdot \vec{\mathbf{S}}_k) + \frac{1}{r_{jk}} \frac{dg(r_{jk})}{dr_{jk}} (\vec{\mathbf{r}}_{jk} \cdot \vec{\mathbf{S}}_j) (\vec{\mathbf{r}}_{jk} \cdot \vec{\mathbf{S}}_j) \right], \quad (4.4)$$

where $g(r_{ij}) = \frac{1}{r_{ij}} \frac{d\phi(r_{ij})}{dr_{ij}}$ with $r_{ij} = |\vec{\mathbf{r}}_i - \vec{\mathbf{r}}_j|$ and $\phi(r_{ij})$ was defined in Eq. (4.3). The index k is used to ensure that when $\vec{\mathbf{f}}_{\text{anis},2,i} = -\nabla_{\vec{\mathbf{r}}_i} \mathbf{H}_{\text{anis},2,k}$ is evaluated with respect to atom i , no terms are missed during the differentiations (as shown explicitly, terms with indices j and k swapped, occur in the double summation in Eq. (4.4)). This leads to

$$\vec{\mathbf{f}}_{\text{anis},2,i} = C_2 \sum_{j \neq i} \frac{1}{r_{ij}} \left[\frac{dg(r_{ij})}{dr_{ij}} \left\{ \vec{\mathbf{S}}_i \cdot \vec{\mathbf{S}}_i + \vec{\mathbf{S}}_j \cdot \vec{\mathbf{S}}_j - \frac{(\vec{\mathbf{r}}_{ij} \cdot \vec{\mathbf{S}}_i)^2}{r_{ij}^2} - \frac{(\vec{\mathbf{r}}_{ij} \cdot \vec{\mathbf{S}}_j)^2}{r_{ij}^2} \right\} \vec{\mathbf{r}}_{ij} + 2 \frac{dg(r_{ij})}{dr_{ij}} \left\{ (\vec{\mathbf{r}}_{ij} \cdot \vec{\mathbf{S}}_i) \vec{\mathbf{S}}_i + (\vec{\mathbf{r}}_{ij} \cdot \vec{\mathbf{S}}_j) \vec{\mathbf{S}}_j \right\} + \frac{1}{r_{ij}} \frac{d^2 g(r_{ij})}{d^2 r_{ij}} \left\{ (\vec{\mathbf{r}}_{ij} \cdot \vec{\mathbf{S}}_i)^2 + (\vec{\mathbf{r}}_{ij} \cdot \vec{\mathbf{S}}_j)^2 \right\} \vec{\mathbf{r}}_{ij} \right], \quad (4.5)$$

Furthermore, $\vec{\mathbf{H}}_i^{\text{eff}} = -\nabla_{\vec{\mathbf{S}}_i} \mathbf{H}_{\text{anis},2,k}$ also changes because of the addition of Eq. (4.2):

$$\vec{\mathbf{H}}_i^{\text{eff}} = \sum_{j \neq i} J_{ij}(r_{ij}) \vec{\mathbf{S}}_j + 2C_2 \sum_{j \neq i} \left[g(r_{ij}) \vec{\mathbf{S}}_i + \frac{1}{r_{ij}} \frac{dg(r_{ij})}{dr_{ij}} (\vec{\mathbf{r}}_{ij} \cdot \vec{\mathbf{S}}_i) \vec{\mathbf{r}}_{ij} \right], \quad (4.6)$$

where the first term comes from the generalised Heisenberg exchange term in Eq. (3.16). (For the expression equivalent to Eq. (4.5), involving the generalised Heisenberg exchange term, the interested reader is referred to Ref. [48].)

Not only have Eqs. (4.3) through (4.6) been incorporated into SPILADY, which is coded in the C++ programming language, the analytical expressions of the derivatives of $g(r_{ij}) = \frac{1}{r_{ij}} \frac{d\phi(r_{ij})}{dr_{ij}}$ that occur in Eqs. (4.4) – (4.6) have also been added in a new separate module.

Furthermore, because Eq. (4.6) is now a function of the spin of atom i , \vec{S}_i , the equation of motion of its spin $\frac{d\vec{S}_i}{dt} = \frac{-1}{\hbar} \vec{H}_i^{\text{eff}} \times \vec{S}_i$ is no longer linear. This renders the second-order Suzuki-Trotter Decomposition (STD) integration algorithm implemented in SPILADY invalid [55,167,168]. The simplest way to remedy this situation is to use a hybrid integration algorithm, in which the STD is combined with the iterative scheme proposed in Refs. [167,168]. For this, a new effective local field \vec{H}_i^{eff} about the spin of atom i has to be defined [167]:

$$\begin{aligned} \vec{H}_i^{\text{eff}} &= \vec{H}_{\text{exch},i}^{\text{eff}} + \frac{1}{2} \left[\vec{H}_{\text{anis},2,i}^{\text{eff}}(\vec{S}_i(t)) + \vec{H}_{\text{anis},2,i}^{\text{eff}}(\vec{S}_i(t+\delta t)) \right] \\ &= \sum_{j \neq i} J_{ij}(r_{ij}) \vec{S}_j + C_2 \sum_{j \neq i} \left[g(r_{ij}) \vec{S}_i(t) + \frac{1}{r_{ij}} \frac{dg(r_{ij})}{dr_{ij}} (\vec{r}_{ij} \cdot \vec{S}_i(t)) \vec{r}_{ij}, \right. \\ &\quad \left. + g(r_{ij}) \vec{S}_i(t+\delta t) + \frac{1}{r_{ij}} \frac{dg(r_{ij})}{dr_{ij}} (\vec{r}_{ij} \cdot \vec{S}_i(t+\delta t)) \vec{r}_{ij} \right] \end{aligned} \quad (4.7)$$

(It is necessary to mention that there was a sign error in the equivalent of Eq. (4.7) in Ref. [194] (their Eq. (5.9), page 101), with respect to Ref. [167]. The explicit forms of $\vec{H}_{\text{exch},i}^{\text{eff}}$ and $\vec{H}_{\text{anis},2,i}^{\text{eff}}$ have the same sign in Eq. (4.7), as also implied in Ref. [167], but according to Eq. (5.9) in Ref. [194], their explicit forms have opposite signs. This minor discrepancy added greatly to the difficulty of implementing the method in SPILADY, since it was not easily noticed.)

By using Eq. (4.7) instead of (4.6), the spin of atom i can be updated using the existing STD integration scheme implemented in SPILADY. However, regrettably, prior knowledge of the spin of atom i at a future time $(t+\delta t)$ is needed in order to use Eq. (4.7). One can overcome this difficulty by iterating Eq. (4.7), starting from $\vec{S}_i(t+\delta t) \approx \vec{S}_i(t)$, and updating the spin of atom i according to $\frac{d\vec{S}_i}{dt} = \frac{-1}{\hbar} \vec{H}_i^{\text{eff}} \times \vec{S}_i(t)$. In the simulations performed towards this thesis, 4 iterations for every spin update (the lattice degrees of freedom are updated every femtosecond, and the spins every 0.2 fs [55,56,194]), are sufficient to guarantee no apparent energy drift, at least in the presence of only the second-order anisotropy correction in Eq. (4.2), over a simulation time of 500 picoseconds:

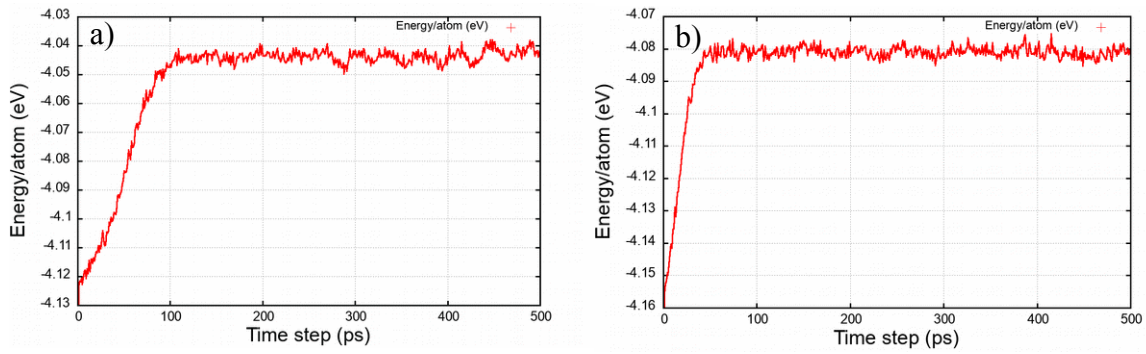


Fig. 4.3: Comparison of the energy a $16 \times 16 \times 16$ cube of (001) BCC iron as a function of time step in a simulation with a) first and second order anisotropy corrections, where $C_1 = 0.2$ eV and $C_2 = 0.1$ eV, and b) only a second order anisotropy correction, where $C_2 = 0.3$ eV [55]. There appears to be energy drift in the case with both first and second anisotropy corrections. The first anisotropy correction does not obey time-reversal symmetry in the absence of an external magnetic field and has thus been omitted in this work. The exchange and anisotropy coefficients and cutoffs used to generate these results have been taken from Refs. [48,55].

Finally, to test my implementation of Perera *et al.*'s method in SPILADY, some of the results of Ref. [194] are reproduced here, to validate the implementation:

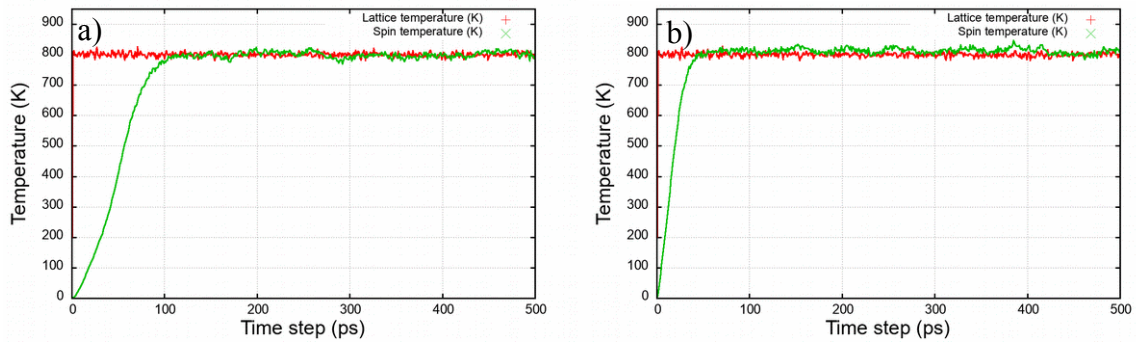


Fig. 4.4: Comparison of the lattice and spin temperatures of a $16 \times 16 \times 16$ cube of (001) BCC iron as a function of time step in a simulation with a) first and second order anisotropy corrections, where $C_1 = 0.2$ eV and $C_2 = 0.1$ eV, and b) only a second order anisotropy correction, where $C_2 = 0.3$ eV [55,56,194]. Only the lattice temperature is thermostatted in this case, and thus rises almost instantaneously to the target temperature of 800 K. The spins take roughly $\sim 10^2$ ps to thermalise to the same temperature as the lattice, as expected [49,50]. The exchange and anisotropy coefficients and cutoffs used to generate these results have been taken from Refs. [48,55].

To calculate the spin temperature when the effective field about atom i , Eq. (4.6), depends on the spin of i , \vec{S}_i , itself, also required modifying the source code of SPILADY, such that it uses the full definition of the spin temperature [49,56,196]:

$$T_s = \frac{\sum_i |\vec{S}_i \times \nabla_{\vec{S}_i} H_{\text{spin}}|^2}{k_B \sum_i [\vec{S}_i \times \nabla_{\vec{S}_i}] \cdot [\vec{S}_i \times \nabla_{\vec{S}_i}] H_{\text{spin}}}, \quad (4.8)$$

and not the simplified equation implemented in the original source code of SPILADY [134],

$$T_s = \frac{\sum_i |\vec{S}_i \times \vec{H}_i^{\text{eff}}|^2}{2k_B \sum_i \vec{S}_i \cdot \vec{H}_i^{\text{eff}}}, \quad (4.9)$$

where $\nabla_{\vec{S}_i} H_{\text{spin}} = -\vec{H}_i^{\text{eff}}$, with \vec{H}_i^{eff} as defined in Eq. (4.6). When \vec{H}_i^{eff} depends explicitly on \vec{S}_i , Eq. (4.8) no longer reduces to Eq. (4.9), and the full definition of T_s in Eq. (4.8) has to be used.

Finally, as a further test of the implementation in SPILADY of the uniaxial magnetic anisotropy correction in Eq. (4.2), the evolution of the ratio of magnetisation to saturation magnetisation has been calculated:

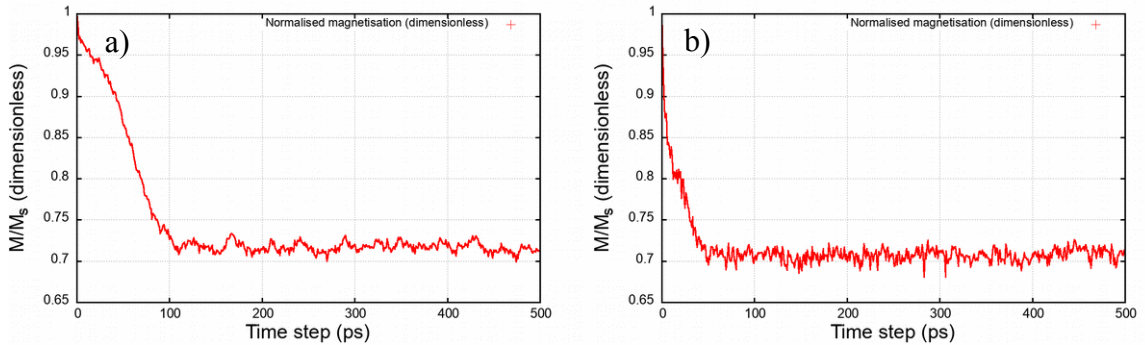


Fig. 4.5: Comparison of the normalised magnetisation of a $16 \times 16 \times 16$ cube of (001) BCC iron as a function of time step in a simulation with a) first and second order anisotropy corrections, where $C_1 = 0.2$ eV and $C_2 = 0.1$ eV, and b) only a second order anisotropy correction, where $C_2 = 0.3$ eV [55,56,194]. The exchange and anisotropy coefficients and cutoffs used to generate these results have been taken from Refs. [48,55].

The equilibrium magnetisation of $\sim 1.55 \mu_B$ at 800 K (the experimentally-observed saturation magnetisation of iron is $2.20 \mu_B$ (see Ref. [194] and references therein)), is

closer to the experimentally-observed value of $\sim 1.8 \mu_B$ at 800 K [197], than the value $\sim 1.4 \mu_B$ reported in Refs. [56,198].

Note that, to obtain their results, Perera *et al.* [55,194] used the the Derlet-Dudarev EAM potential and the parameters for the generalised Heisenberg exchange term ($J_0 = 904.90177$ meV and $r_c = 3.75$ Å) that were fitted by Ma *et al.* in Ref. [48]. Unfortunately it has been discovered that the original fitting parameters of Eq. (3.17) are wrong, due to the incorrect conversion of exchange-pair energies from mRy to eV in Ref. [52]. A fitting of the latest (correct) data reported by Wang *et al.* in Ref. [53], leads to $J_0 = 110.1698373$ meV and $r_c = 5.34$ Å. These corrected parameters, along with the Malerba *et al.* EAM potential [43], are used for the production results presented in Chapter 7.

Using the correct fitting parameters ($J_0 = 110.1698373$ meV and $r_c = 5.34$ Å) does not seriously affect the results for the spin temperature shown in Fig. 4.4. The relative greater importance of the anisotropy correction ($C_2 = 0.3$ eV) compared with the exchange term only leads to the spin temperature overshooting the lattice temperature somewhat (see Fig. 4.6 a) below).

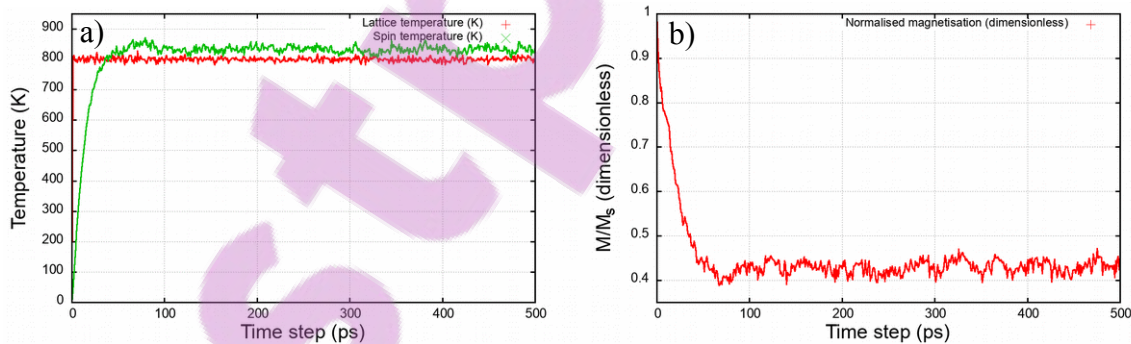


Fig. 4.6: a) Thermalisation of the spin temperature, and b) normalised magnetisation, of a $16 \times 16 \times 16$ cube of (001) BCC iron at 800 K, as a function of time step, in a simulation with $J_0 = 110.1698373$ meV and $r_c = 5.34$ Å in Eq. (3.17), and $C_2 = 0.3$ eV in Eq. (4.2).

The normalised magnetisation, on the other hand, in Fig. 4.6 b), is affected more significantly by the use of the correct exchange parameters. However, it is now more in line with the value at 800 K reported in Ref. [54], in which spin-lattice dynamics

simulations are performed in an *ab-initio* approach.

Using the correct fittings in Eq. (3.17) may imply that these models fail to reproduce the experimental Curie temperature of Fe, which is 1043 K. Instead, a Curie temperature for bulk Fe is found that is closer to 900 K, which is reasonable for a semi-classical model. Also, it is well known that *ab-initio* calculations of the exchange parameters underestimate the Curie temperature of ferromagnetic metals (see Ref. [51] and references therein). But, by merely scaling the parameters for the generalised Heisenberg exchange energy in Eq. (3.16), to, say, the incorrect values for Fe used in Refs. [48,55], one can obtain a model that gets closer to the experimental value of the Curie temperature. In fact, this is precisely what is done in Ref. [51] to obtain an improved SLD model of bulk Ni, which usually exhibits even worse agreement than Fe between its experimental Curie temperature (~ 630 K) and values estimated from *ab-initio* calculations (~ 400 K).

4.2.2. Spin-lattice dynamics of ferromagnetic nanocontacts

This section illustrates how SLD simulations of ferromagnetic nanocontact evolution is performed in this work. To that end, Fig. 4.7 shows an example SLD simulation of a Fe(001) nanocontact being stretched at ~ 1 m/s, until immediately before it ruptures. For illustrative purposes, the magnetisation in the frozen ends of the nanocontact, representing the bulk leads in an experiment, are aligned anti-parallel, as if two separate oppositely-directed external fields are being applied to the ends. Such a configuration is not the focus of the work in this thesis, but it does give an idea of the capabilities of the SLD simulations of ferromagnetic nanocontacts implemented in SPILADY.

In the simulation depicted in Fig. 4.7, the Derlet-Dudarev EAM potential [153] is used to describe the interactions between the atoms, and the parameters for the exchange interaction are those used in Refs. [55,56,194], i.e, the incorrectly fitted ones. The constant in the uniaxial magnetic anisotropy term is $C_2 = 0.3$ eV.

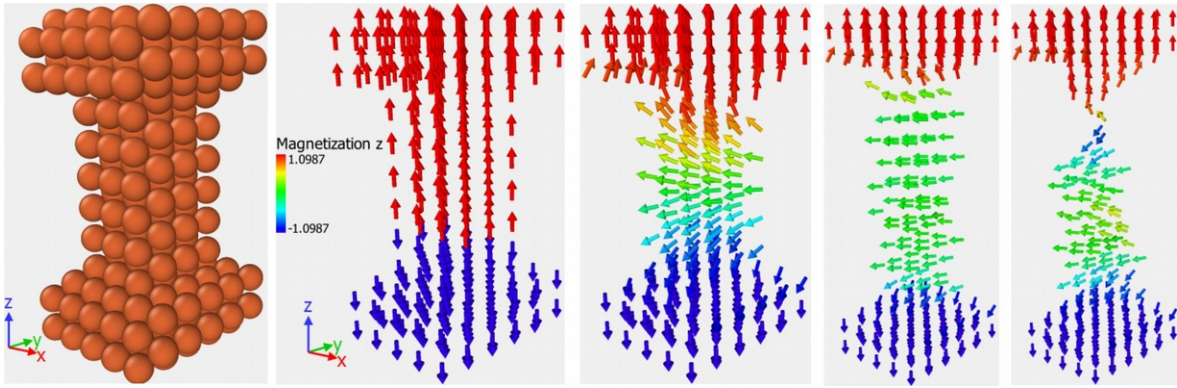


Fig. 4.7: Various stages of the evolution of the spins, initially along $\pm z$, with three quarters of them pointing “up” and the other quarter “down”, in a 308-atom (001)-oriented BCC iron nanocontact (see panel at left) under cyclic loading at 4.2 K. For purposes of illustration, the spins in the frozen top and bottom ends point in opposite directions, but in all the production simulations performed in this work, they point in the direction of a configuration that is consistent with ferromagnetism. The color legend corresponds to the projection of the spins (in μ_B) on the positive z -axis, which is the saturation magnetisation of Fe, $2.2 \mu_B$ divided by the electron’s gyromagnetic factor: 2.002319.

The spins are initially aligned anti-parallel, but as soon as they are allowed to evolve dynamically, a transverse domain wall immediately forms between the oppositely directed spins in the frozen ends (in under 1 picosecond, the interval at which snapshots in the simulation trajectory are written to file). Note that this initial domain wall is about as wide as the contact constriction cross-section is [39].

In this case, when the ends are magnetised in opposite directions, an abrupt domain wall does form in the constriction at last-contact (see the structure furthest to the right in Fig. 4.7). However, in simulations where the spins are all initially aligned parallel and $C_2 > 0$ in Eq. (4.2), no abrupt domain walls form at last-contact, and the orientations of the spins vary gradually along the length of the nanocontacts.

4.3. Vector-relativistic NEGF quantum transport

In Sec 3.4, the theory underpinning the quantum transport code ANT.Gaussian [68,180,187,188,191] was briefly described. This code is employed to do the majority of the conductance calculations in this work. Until very recently, ANT.Gaussian could not perform vector-relativistic calculations with spin-orbit coupling and non-collinear magnetism. In this section, the implementation of spin-orbit coupling in ANT.Gaussian (which formed part of the work of this thesis) is described.

Recall that SOC can play an important role in ferromagnetic transition metals at finite temperatures and in low-dimensional geometries (e.g., iron [17,55,56,118,199,200]), because under these circumstances the orbital magnetic moment of a given atom is no longer quenched, producing via SOC, non-collinear magnetic configurations and enhanced spin moments [118,199,200].

Non-collinear spin textures are accounted for in SLD simulations through the uniaxial magnetic anisotropy correction, Eq. (4.2), that was added to the classical Hamiltonian in Eq. (3.16). It is thus necessary to consider SOC and non-collinear magnetism in DFT transport calculations too. In this regard, there are several open-source DFT packages available that permit SOC in transport calculations. Most notable among the LCAO codes are SIESTA [201] and OpenMX [62]. A widely-used plane-wave DFT code with this capability is Quantum ESPRESSO [182].

Unfortunately, vector-relativistic DFT and NEGF calculations involving magnetism are notoriously expensive computationally, and especially unconstrained non-collinear magnetism makes convergence to the global minimum very difficult to achieve, since the potential landscape in such calculations may contain many local minima that the self-consistent field cycles can easily become trapped in (see Ref. [202] and references therein).

Other than modelling ferromagnetic nanocontacts more realistically, SLD with magnetic anisotropy produce non-collinear magnetic spin textures that can be taken advantage of in *constrained* vector-relativistic DFT calculations [61,63]. Among the codes cited above, OpenMX is the most convenient code for performing self-consistent vector-relativistic NEGF transport calculations in which non-collinear spins can be constrained [184], so that OpenMX can be considered a comprehensive package for NEGF transport calculations. In addition, constraining the spins in such calculations is explicitly encouraged by the authors of OpenMX [62], since it limits the potential space OpenMX has to explore, thus facilitating convergence. Steady convergence does, however, come at a price of a small energy penalty, in the form of an adjustable parameter in constrained vector-relativistic DFT [61,63]. But this measure ensures the final converged spin directions are close to their input values (which are those taken from SLD simulation snapshots).

Although OpenMX, a LCAO-based code, is less computationally expensive than a plane-wave competitor, e.g., Quantum ESPRESSO, it still requires considerable resources, especially memory. Constrained DFT does indeed exhibit better convergence properties than its unconstrained counterpart, but convergence remains slow.

To circumvent the aforementioned limitations and difficulties, in this work, SOC has been implemented in ANT.Gaussian in collaboration with Prof. Juan José Palacios of the Autonomous University of Madrid in Spain, following the approach described in Ref. [57]. Section 4.3.1 provides an overview of the methodology of Ref. [57], while, in the subsequent section, more time will be devoted to discussing the implementation of non-collinear magnetism in ANT.Gaussian, which typically accompanies SOC [202] in ferromagnetic materials at finite temperatures and in low-dimensional geometries.

4.3.1. Spin-orbit coupling in quantum transport

SOC is considered to be an intra-atomic effect, and the core electrons of the all-electron basis sets used in ANT.Gaussian are expected to make the greatest contribution due to their nodal structure near the core (see Ref. [57] and references therein). Therefore, in the lowest-order approximation, the Dirac-Kohn-Sham Hamiltonian, which is fully relativistic (with its electronic and positronic parts decoupled), yields the $\xi(r)\vec{L}\cdot\vec{S}$ SOC operator (see Ref. [57] and references therein). The form this operator takes shows that orbital and spin angular momentum are mixed.

The radial and angular components of the wave functions in LCAO DFT are orthogonal. The angular components are just Cartesian spherical harmonics, and the radial parts are the so-called (and widely-available) contracted Gaussian type orbitals (CGTOs), used, for example, by Gaussian [177] and CRYSTAL [173]:

$$R(r) = N_0 \left\{ \sum_i d_i \left(N_i r^{n-1} e^{-\alpha_i r^2} \right) \right\}, \quad (4.10)$$

where N_0 is an overall normalisation factor and each $N_i r^{n-1} e^{-\alpha_i r^2}$, referred to as an uncontracted Gaussian “primitive”, is normalised by its own factor N_i . In a typical

valence basis set, for which there are many available online (see, for example, the repository at <https://bse.pnl.gov/bse/portal>), the values of the exponent α_i , which describes the extent of the uncontracted primitive, and d_i , the coefficient of each uncontracted primitive in the expansion of contracted primitives in Eq. (4.10), are listed for different “shells” corresponding to different values of angular momentum $L = 0, 1, 2, 3, \dots$, such that $n = L + 1$ in Eq. (4.10).

The above-mentioned orthogonality of the wave functions in LCAO DFT allows the matrix elements of the SOC operator $\xi(r)\vec{L}\cdot\vec{S}$ to be evaluated simply as [57]:

$$\xi_{ij}\langle l_i; m_{l_i}; s | \vec{L}\cdot\vec{S} | l_j; m_{l_j}; s' \rangle, \quad (4.11)$$

i.e., the operator $\vec{L}\cdot\vec{S}$ is evaluated between the spherical harmonics $|l_i; m_{l_i}; s\rangle$, and the spin-orbit constants ξ_{ij} as [57]

$$\xi_{ij} = \frac{\hbar^2 e^2}{2 m_e c^2} \int_0^\infty \frac{1}{r} \frac{dV_{\text{eff}}}{dr} R_i(r) R_j^*(r) r^2 dr. \quad (4.12)$$

The angular elements of the intra-atomic SOC matrix are defined relative to the standard orbital and spin angular momenta quantisation axis, the z -axis:

$$\langle l_i; m_{l_i}; s | \vec{L}\cdot\vec{S} | l_j; m_{l_j}; s' \rangle = \langle l_i; m_{l_i}; s | L_z S_z + \frac{1}{2} L_+ S_+ + \frac{1}{2} L_- S_- | l_j; m_{l_j}; s' \rangle, \quad (4.13)$$

where L_z , $L_+ = L_x + iL_y$, and $L_- = L_x - iL_y$ are the standard orbital angular momentum operators of quantum mechanics [185], whose sizes as matrices depend on the shell type of the CGTO in question, and S_z , $S_+ = S_x + iS_y$, and $S_- = S_x - iS_y$ are the spin-half angular momentum operators. Below, the $\xi_{ij}\langle l_i; m_{l_i}; s | \vec{L}\cdot\vec{S} | l_j; m_{l_j}; s' \rangle$ matrix is reproduced for a single site ($i = j$) and $L = 1$ shell CGTO, in terms of the Cartesian spherical harmonics used by Gaussian internally, in the order $(|p_x\rangle; |p_y\rangle; |p_z\rangle)$:

$$\begin{pmatrix}
& |p_{x,\uparrow}\rangle & |p_{y,\uparrow}\rangle & |p_{z,\uparrow}\rangle & |p_{x,\downarrow}\rangle & |p_{y,\downarrow}\rangle & |p_{z,\downarrow}\rangle \\
|p_{x,\uparrow}\rangle & 0 & -i\frac{\xi_{11}}{2} & 0 & 0 & 0 & \frac{\xi_{11}}{2} \\
|p_{y,\uparrow}\rangle & i\frac{\xi_{11}}{2} & 0 & 0 & 0 & 0 & -i\frac{\xi_{11}}{2} \\
|p_{z,\uparrow}\rangle & 0 & 0 & 0 & -\frac{\xi_{11}}{2} & i\frac{\xi_{11}}{2} & 0 \\
|p_{x,\downarrow}\rangle & 0 & 0 & -\frac{\xi_{11}}{2} & 0 & i\frac{\xi_{11}}{2} & 0 \\
|p_{y,\downarrow}\rangle & 0 & 0 & -i\frac{\xi_{11}}{2} & -i\frac{\xi_{11}}{2} & 0 & 0 \\
|p_{z,\downarrow}\rangle & \frac{\xi_{11}}{2} & i\frac{\xi_{11}}{2} & 0 & 0 & 0 & 0
\end{pmatrix}, \quad (4.14)$$

where $\xi_{11}=1.5$ eV in the case of Bismuth [203], for example. In terms of the usual spherical harmonics $|l_i; m_{l_i}; s\rangle$:

$$\begin{cases}
|p_{x,\uparrow}\rangle = -\frac{1}{\sqrt{2}}(|1, 1, \frac{1}{2}\rangle - |1, -1, \frac{1}{2}\rangle) \\
|p_{y,\uparrow}\rangle = \frac{i}{\sqrt{2}}(|1, 1, \frac{1}{2}\rangle + |1, -1, \frac{1}{2}\rangle) \\
|p_{z,\uparrow}\rangle = |1, 0, \frac{1}{2}\rangle
\end{cases} \quad (4.15)$$

The matrix elements have been calculated using the eigenvalues of the general angular momentum operators:

$$\begin{cases}
J_+ |j, m\rangle = \hbar \sqrt{(j-m)(j+m+1)} |j, m+1\rangle \\
J_- |j, m\rangle = \hbar \sqrt{(j+m)(j-m+1)} |j, m-1\rangle \\
J_z |j, m\rangle = \hbar m |j, m\rangle
\end{cases} \quad (4.16)$$

where, in the case of the orbital angular momentum, $j=l=0, 1, 2, \dots$ and $m_l=-l, \dots, 0, \dots, +l$, and in the case of the spin angular momentum, $j=s=\frac{1}{2}$ and $m_s=-\frac{1}{2}, +\frac{1}{2}$. The $L_z S_z + \frac{1}{2} L_+ S_+ + \frac{1}{2} L_- S_-$ operator in Eq. (4.13), therefore, acts on Eqs. (4.16) by writing, for example, $|1, 1, -\frac{1}{2}\rangle = |1, 1\rangle | \frac{1}{2}, -\frac{1}{2}\rangle$. The reader may have noticed that the \hbar^2 resulting from the evaluation of the matrix elements in Eq. (4.14) has been absorbed into the definition of ξ_{ij} in Eq. (4.12).

In a final step of an ANT.Gaussian calculation, the SOC matrix is added directly to the final self-consistent Hamiltonian of the *device* region H_D discussed in Sec 3.4, and

obtained from a converged ANT.Gaussian calculation (which runs over the total number of orbitals in the calculation). Since the SOC matrix is twice the size of this Hamiltonian, H_D is first recast to a double-sized matrix, with the spin-majority and spin-minority matrices, which are equal in an closed-shell (spin-unpolarised) calculation, on the upper and lower diagonal blocks of the new double-sized matrix, respectively.

As a test of the present implementation of SOC in ANT.Gaussian, Fig. 4.8 shows the quantisation of conductance at $1 G_0$ observed for (metallic) Bi(111) bilayer nanoribbons along their zig-zag edges [203], for ribbons of various sizes and using the CRENBBS minimum $s-p$ basis set [204] for all the atoms in the ribbon. The radial SOC coefficient was taken to be $\xi_{11}=1.5$ eV, which is equivalent to the tight-binding calculation of Ref [203].

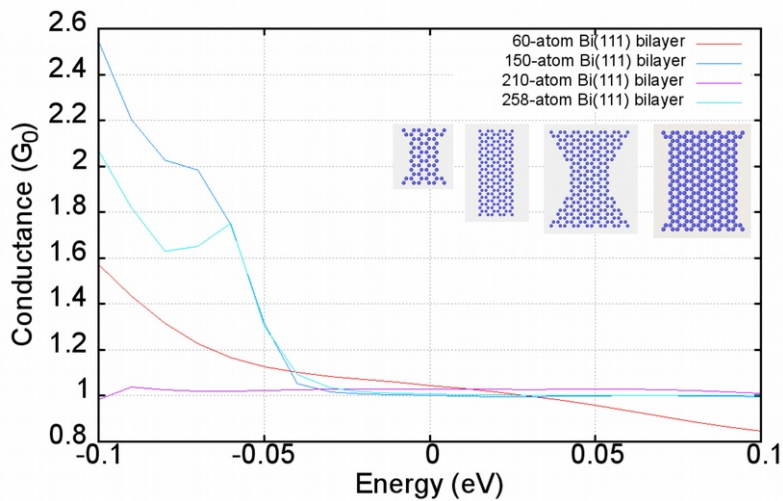


Fig. 4.8: Conductance as a function of energy for the 4 different input structures shown in the insets, obtained using the implementation of SOC in ANT.Gaussian in this work, with the CRENBBS minimal valence-electron basis set [204]. In agreement with Ref. [203], conductance is quantised at around $1 G_0$ at zero bias, or zero energy, in the figure.

A feature of ANT.Gaussian that is not available in tight-binding implementations of SOC, such as the one in Ref. [203], is the availability of high-quality benchmarked basis sets, up to all-electron quality. The only requirement on the all-electron basis sets, in particular, is, as discussed in Ref. [57], that they reproduce very well the band structure of the material before the addition of the SOC matrix. In that case, the band structure after addition of SOC will also be reliable.

The main difference with regard to the implementation of SOC in CRYSTAL14 [173] in Ref. [57], is that there are no all-electron tight-binding parameters available to describe the electronic structure of the electrodes or leads in transport calculations. It therefore becomes necessary to mix basis sets in ANT.Gaussian, a common practice [15,124,176,205], and apply a valence basis set to the atoms that are in direct contact with the semi-infinite Bethe lattice electrodes, in order to make them compatible with the TB parameters used for the electrodes. In our past work, higher quality basis sets were assigned to several atoms in the minimum cross-section of CMD structures. These higher quality basis sets for atoms near the minimum cross-section, resulted in improved conductance results [192]. That practice is continued here, the main difference being that all-electron basis sets are assigned to 5-15 atoms in the smallest cross-section of the CMD/SLD structures, depending on the coordination of the atoms there.

Conductance quantisation in Bi(111) bilayers is again reproduced in order to test the use of mixed basis sets in ANT.Gaussian calculations. The following conductance functions (see Fig. 4.9) have been obtained for a 150-atom ribbon-shaped Bi(111) bilayer, for transport along the zig-zag edge, after assigning various sized Gaussian basis sets (CRENBS (both contracted and fully uncontracted), CRENBL (uncontracted) [204], cc-pVDZ-PP (small core) [206], Douglas-Kroll-Hess DZP (all-electron) [207]) to 30 atoms in the centre of the ribbon:

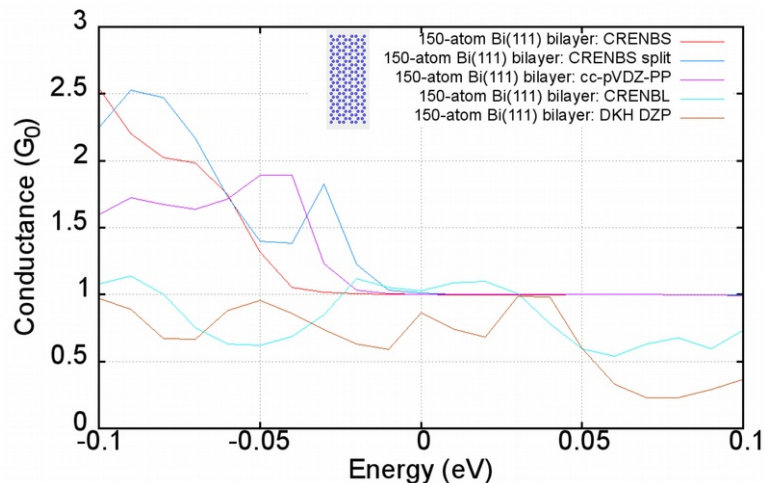


Fig. 4.9: Conductance as a function of energy for the 150-atom Bi(111) bilayer input structure shown in the inset, obtained using the implementation of SOC in ANT.Gaussian in this work, and by assigning 5 different basis sets to 30 atoms in the centre of the nanoribbon (the remaining atoms are assigned the minimal basis set (CRENBS) to make them compatible with the tight-binding parameters of the Bethe lattice semi-infinite leads).

In all cases in Fig. 4.9, $\xi_{11} = 1.5$ eV and $\xi_{22} = 0.5$ eV have been used. Deviation from conductance quantisation at $1 G_0$ occurs in the case of the all-electron basis set (DKH DZP) because it has not been optimised for periodic structures, and probably does not appropriately reproduce the band structure of bulk Bi even before the addition of SOC. In addition, a guess value of $\xi_{33} = 0.25$ eV has been used for the F shells of the DKH DZP basis set, absent a known experimental parameter. For all the other basis sets, these results reproduce the expected quantisation of conductance of $1 G_0$ at zero bias, therefore confirming the validity of the implementation.

Before moving on to transport calculations with non-collinear magnetism, two further pieces of evidence are provided in support of the implementation of (collinear) SOC in ANT.Gaussian in this work.

It is widely known that SOC leads to anisotropic magnetoresistance (AMR), or equivalently, anisotropic magnetoconductance (AMC) (see Ref. [17] and references therein). Although its effect on $3d$ transition metals is now known to be a very small [16,18], AMR/C accounts for the variation in resistance/conductance of a nanocontact with the angle of an applied external magnetic field relative to the direction of transport of charge. Therefore, the maximum extent of AMC occurs when all the spins are perpendicular to the transport direction. The implementation of SOC in ANT.Gaussian permits one to test for AMC in simple nanocontacts, since the implementation in this work imposes the z axis as the quantisation axis of the spins. Thus, one can test for AMC by performing a transport calculation on nanocontacts that are (physically) oriented along different coordinate axes.

Even though AMC is expected to be very small in Fe nanocontacts, as a simple test, conductance curves have been calculated in ANT.Gaussian for a toy-model iron nanocontact [118], oriented, in turn, along the y and z axes (see the insets in Fig. 4.10, in which the light pink atoms on the ends of the nanocontact merely show that the Bethe lattices describing the semi-infinite leads have been correctly attached). (As an aside, it should be noted that 3-atom or more monatomic chains do not form in $3d$ transition metals [27]). In order to test for appreciable AMC in ferromagnetic Fe nanocontacts, unrealistically large SOC coefficients have been used for Fe ($\xi_{11} = 3.5$ eV for the $L = 1$

shells and $\zeta_{22} = 0.7$ eV for the $L=2$ shells). Note that experimentally, Fe has small SOC coefficients (about an order of magnitude smaller than the values used here) [60].

Clearly, there is a large difference between the conductance values at zero bias when SOC is active, while without it, the conductance functions of the two structures nearly overlap. With this, the implementation of SOC in ANT.Gaussian is validated, since its ability to reproduce AMC in the presence of SOC is demonstrated, even though an unrealistic model has been used for this purpose. The small differences between the curves in the absence of SOC can be attributed to the algorithms used by ANT.Gaussian to obtain the self-consistent solution.

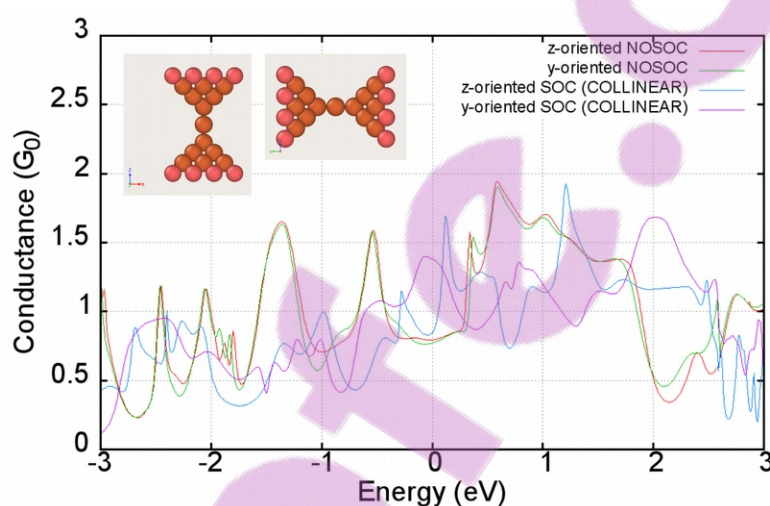


Fig. 4.10: Conductance as a function of energy for the 29-atom Fe (001) input structure shown in the insets, obtained using the implementation of SOC in ANT.Gaussian in this work, and by assigning an all-electron basis set to the 11 atoms in the centre of the contact (the remaining atoms are assigned the minimal basis set (CRENBS) to make them compatible with the tight-binding parameters of the Bethe lattice semi-infinite leads). In the cases with SOC, the parameters $\zeta_{11} = 3.5$ eV and $\zeta_{22} = 0.7$ eV have been used, which are much larger than reported in the literature [60]. Using large SOC parameters is necessary to obtain appreciable AMC in Fe and Ni nanocontacts.

For calculations on Fe, the all-electron Gaussian basis set assigned to the 11 atoms in the centre of each contact first had to be optimised, by following the same procedure employed to optimise the DOLL all-electron basis set for bulk Ni in Ref. [208]. The code billy, available online at <http://www.tcm.phy.cam.ac.uk/~mdt26/crystal.html>, used in combination with the LCAO DFT code CRYSTAL14 [173] for periodic structures, was the most convenient tool for this task. CRYSTAL14 and ANT.Gaussian use the same basis sets. To ensure that the optimised all-electron basis set for Fe was appropriate, the band

structure it produces for bulk Fe was compared with that obtained by OpenMX [62] and Wien2K [65]. As can be seen in Fig. 4.9 below, rather good agreement results:

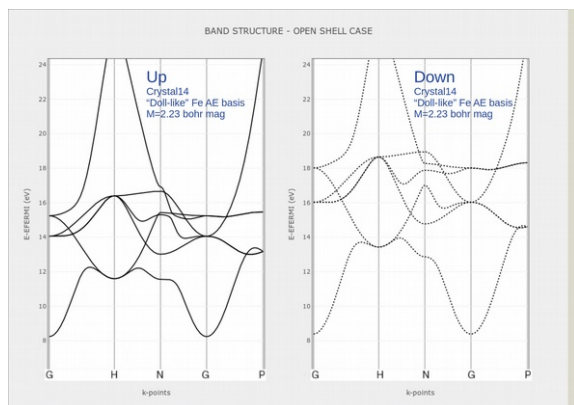
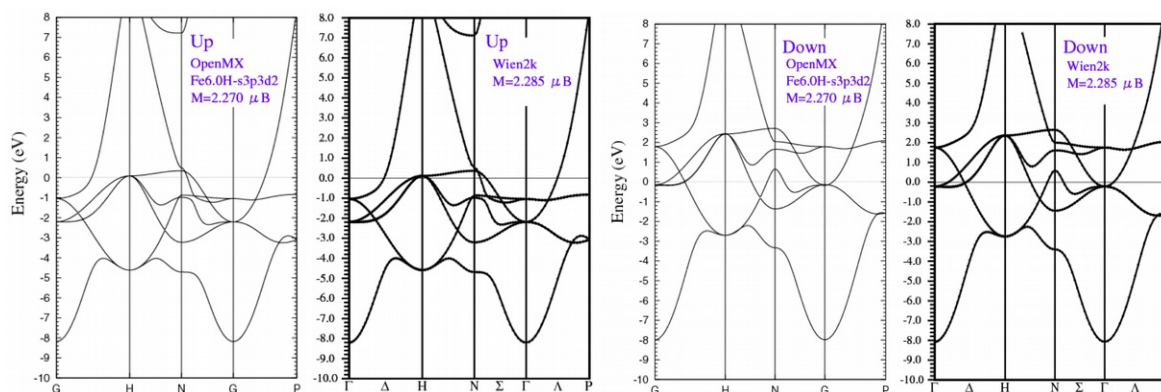


Fig. 4.11: (Left) Band structure obtained after optimising an all-electron basis set for Fe, in exactly the same way as was done in Ref. [208] for Ni. This band plot was made at <http://crysplot.crystalsolutions.eu/>. A comparison with results obtained in OpenMX and Wien2K is shown below. The energy scale on the left is the same in each case, it has just been zeroed at a different value (the Fermi energy in the bottom band plots)



As a final test of the present implementation of (collinear) SOC in ANT.Gaussian, results obtained from a vector-relativistic transport calculation in OpenMX on the same structure as before, a monatomic chain of 3 Fe atoms sandwiched between two Fe(001) bulk electrodes, are compared with the corresponding results produced by ANT.Gaussian. However, in this case, more realistic SOC parameters have been used in ANT.Gaussian (see Fig. 4.10), because OpenMX calculates the SOC parameters for Fe internally, which presumably agree with their experimental (small) values [60]. But, instead of doing the calculations in OpenMX on one structure physically oriented along z , and the other along y , the Euler angles (θ, ϕ) of the spins of all the atoms (including in the semi-infinite leads on either side of the device) were constrained to be (i) zero (along z) in the first calculation, and, (ii) 90 degrees (along y) in the second calculation. Note that the structure is still

physically oriented along z in both OpenMX calculations. At the cost of a small energy penalty term (~ 0.1 eV), equivalent to a Zeeman term or the application of an external magnetic field, OpenMX permits such calculations. A very high quality basis set ($s3p3d2$ valence space, with a 6 bohr cutoff, giving excellent agreement with the band structure obtained in Wien2K, see Fig. 4.11 above), was assigned to the 3-atom chain and layers immediately adjacent on either side (11 atoms in total), while a minimal basis set was assigned to the remaining atoms ($s2p2d1$ valence space and 5 bohr cutoff), in a fashion analogous to the approach used in ANT.Gaussian calculations.

In ANT.Gaussian, the calculation was repeated on the same structure, first oriented along z , and then along y , (the spins are quantised along the z axis in both cases). The all-electron basis set was assigned to the 11 atoms in the constriction, and the CRENBS minimal basis set, to the rest. This time, literature values of the SOC parameters for Fe ($\xi_{11} = 0.18$ eV and $\xi_{22} = 0.06$ eV [60]) have been used. The generally good agreement between the two codes in Fig. 4.12 is impressive, especially at the Fermi energy, or zero bias (see the inset in Fig. 4.12). Such good agreement is not surprising, given past work comparing ANT.Gaussian and OpenMX [176]. The visible discrepancies arise from the different description, by each basis set, of the valence space of the atoms, which occurs even when comparing only ANT.Gaussian calculations that employ different Gaussian basis sets [124,176]. Note that the same energy division (0.01 eV) was used in both codes to generate the conductance curves, but that the greater noise in the OpenMX results is a general feature of open-shell (spin-polarised) calculations in codes that use the supercell approach to describe the semi-infinite leads (of finite cross-section) in transport calculations (see Ref. [180] for a detailed comparison between the two different electrode models used in OpenMX and ANT.Gaussian).

Also note that, contrary to what is claimed in Ref. [60], at the DFT+GGA level of quality, OpenMX does not obtain a large orbital magnetic moment on the central atom in the 3-atom chain: $\sim 0.2 \mu_B$. Instead, the much enhanced magnetic moment obtained ($3.60 \mu_B$), is entirely due to the greater localisation of the d -electrons on the central atom in the monatomic chain as compared to bulk Fe. The same phenomenon is known to give rise to emergent magnetism in Pt chains, which is a paramagnetic metal in the bulk [118]. It is

worth mentioning that the value obtained by ANT.Gaussian for the magnetic moment of the same atom ($3.55 \mu_B$), compares favourably with the OpenMX result.

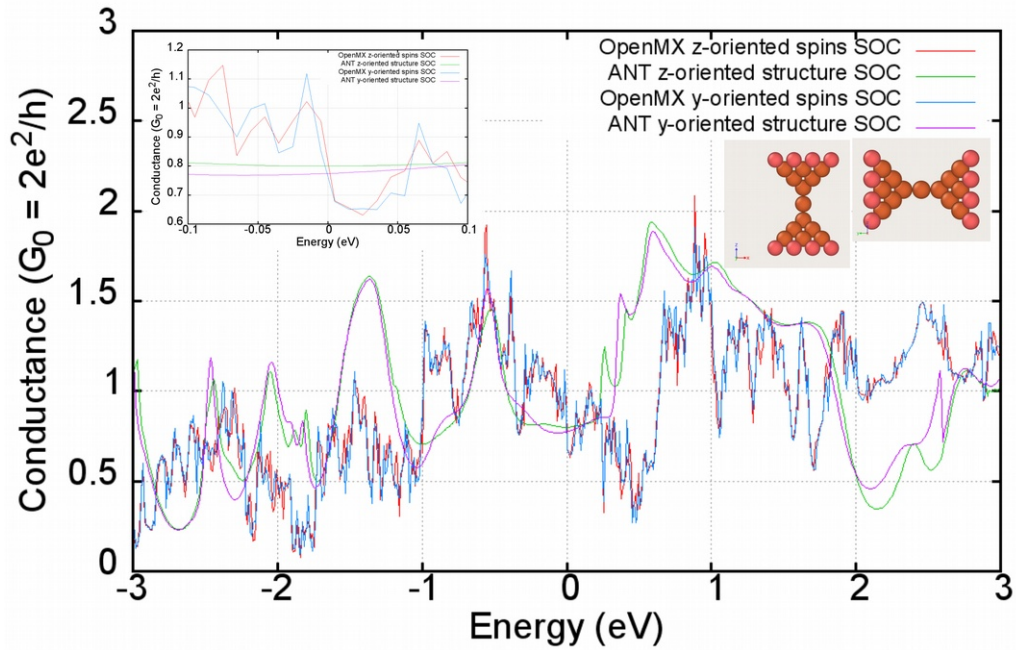


Fig. 4.12: Conductance as a function of energy for the 29-atom Fe (001) input structure shown next to the legend, obtained using the implementation of SOC in ANT.Gaussian in this work, and by performing a vector-relativistic self-consistent calculation in OpenMX, on a z -oriented input structure, with the *spins* oriented along the z axis in one case (red curve), and along the y axis in the other (light blue curve). As SOC parameters in ANT.Gaussian, $\zeta_{11} = 0.18$ eV and $\zeta_{22} = 0.06$ eV were taken from Ref. [60]. There is strikingly good agreement between the conductance values at the Fermi level, or zero bias, and no appreciable anisotropic magnetoresistance (conductance).

4.3.2. Non-collinear magnetism in quantum transport

When the immediate environment of a ferromagnetic atom, having a resultant spin per atom, is distorted from its symmetry in a perfect bulk lattice, e.g., such as in a nanocontact undergoing dynamic cyclic loading at low temperatures, the orbital angular momentum of the atom is no longer “quenched” [15,55]. Spin-orbit coupling will then give rise to non-collinear spin configurations, since the orbital angular momenta, and by extension, spin momenta, will not all point in the same direction.

Such non-collinear spin configurations can, in principle, lead to appreciable *intrinsic* magnetoresistance (MR), or equivalently magnetoconductance (MC), in thinning and

widening ferromagnetic nanocontacts [16,18]. It is therefore necessary to take into account non-collinear spin configurations in quantum transport calculations.

In practice, not only the atomic configurations from SLD simulations will be used in DFT quantum transport calculations. Here, for the first time, the non-collinear spin configurations from SLD simulations of nanocontacts are also included.

In the implementation of non-collinear magnetism in ANT.Gaussian in this work, it is assumed that the effect of the unquenched orbital angular momentum is provided by the SLD simulations, since ANT.Gaussian cannot produce non-collinear orientations of the spins. This is a reasonable approximation because *ab-initio* data have been mapped onto the semi-classical spin-dependent terms in the spin-lattice Hamiltonian (Eqs. (3.16) and (4.2)) used to perform SLD simulations in this work. Since the quantisation axis in ANT.Gaussian is chosen to be that in which the L_z operator is diagonal, the Cartesian coordinates of the spins in SLD simulations can be converted to their Euler angles (θ, ϕ) , with respect to the z -axis, in order to be used directly as input in DFT quantum transport calculations. OpenMX [62], for example, takes the Euler angles of atomic spins as input in non-collinear DFT transport calculations.

In order to include non-collinear spins in ANT.Gaussian, the approach taken in the tight-binding implementation of SOC and non-collinear magnetism in Refs [58,60] has been adopted in this work. Recall from the last chapter that the final self-consistent Hamiltonian matrices of the *device* region of the nanocontact from a spin-polarised (open-shell) calculation in ANT.Gaussian, one corresponding to the “up” and the other to the “down” spin components, are placed on the upper and lower diagonal blocks, respectively, of a new double-sized matrix, before the SOC matrix is added to it. We can express this double-sized matrix in a compact notation that will show the reader that the same approach as in Refs. [58,60] can be followed to include non-collinear magnetism in ANT.Gaussian transport calculations:

$$[\mathbf{H}_{\text{glob}}]_{\sigma'j\nu}^{\sigma i\mu} = U(\theta, \phi) \cdot [\mathbf{H}_{\text{loc}}]_{\sigma'j\nu}^{\sigma i\mu} \cdot U^\dagger(\theta, \phi), \quad (4.17)$$

where

$$U(\theta, \phi) = \begin{pmatrix} e^{-i\frac{\phi}{2}} \cdot \cos\left(\frac{\theta}{2}\right) & -e^{-i\frac{\phi}{2}} \cdot \sin\left(\frac{\theta}{2}\right) \\ e^{i\frac{\phi}{2}} \cdot \sin\left(\frac{\theta}{2}\right) & e^{i\frac{\phi}{2}} \cdot \cos\left(\frac{\theta}{2}\right) \end{pmatrix}, \quad (4.18)$$

is a standard unitary transformation, and (θ, ϕ) are the Euler angles of the spins with respect to the global quantisation axis, along z . The indices i, j run over atomic centres;

μ, ν index the orbitals on an atomic centre; and $\sigma = \uparrow, \sigma' = \downarrow$ are the spin components.

In the double-sized converged Hamiltonian to which the SOC matrix is added, the spins are not mixed, i.e., $\sigma = \sigma' = \uparrow$ or \downarrow in $[H_{\text{loc}}]_{\sigma'j\nu}^{\sigma i\mu}$ in Eq. (4.17). Equivalently, only the “ $\uparrow\uparrow$ ” and “ $\downarrow\downarrow$ ” blocks of this matrix are populated before the unitary transformation or addition of the SOC matrix. In spin-polarised (open-shell) calculations, the unitary transformation and addition of SOC have the effect of mixing the two spin components [124], and the “ $\uparrow\downarrow$ ” and “ $\downarrow\uparrow$ ” blocks of the double-size matrix become populated after these operations have been performed.

To justify the transformation in Eq. (4.17), it is assumed that the spins are originally quantised along their own (arbitrary) *local* magnetisation axes, and that the transformation re-expresses them in a basis that has the z -axis as the *global* quantisation axis. In a collinear spin-polarised DFT calculation, absent SOC to impose a given *global* quantisation axis, all that is known is that the spins are divided into two sub-populations, spin majority and minority, but their orientations in physical space are undefined [171]. (E.g., the results in Fig 4.10 are unaffected by physical orientation in the absence of SOC). This justification follows the same argument made in Ref. [59].

A self-consistent vector-relativistic treatment of non-collinear magnetism does not only optimise the spatial charge density of the electrons, with charge conservation as constraint, but also the directions and magnitudes of their spins, with the constraint that the average atomic magnetisation continues to point in the direction of the input atomic spin directions [59,60,63]. Since the SLD simulations in this work, in theory, provide a realistic description of spin orientations in ferromagnetic nanocontacts, it is not necessary, in a first approximation, to relax or optimise their directions, so the transformation in Eq. (4.17) is

performed on $[\mathbf{H}_{\text{loc}}]_{\sigma'j\nu}^{\sigma i\mu}$, and then the SOC matrix is added to the transformed or “rotated” matrix $[\mathbf{H}_{\text{glob}}]_{\sigma'j\nu}^{\sigma i\mu}$, whose spins are quantised with respect to the standard or z axis.

In practice, the intra-atomic ($i = j$) energy and overlap elements of $[\mathbf{H}_{\text{loc}}]_{\sigma'j\nu}^{\sigma i\mu}$ are transformed using the Euler angles (θ, ϕ) of the spin belonging to a given atomic centre. However, this leaves the transformation of the interatomic ($i \neq j$) hopping and overlap elements in $[\mathbf{H}_{\text{loc}}]_{\sigma'j\nu}^{\sigma i\mu}$, which need to be addressed. The approach adopted in this work is to, in a first approximation, take the arithmetic average of the transformed hopping and (interatomic) overlap elements ($i, j; i \neq j$).

Consequently, in order to calculate the conductance when non-collinear spins are present (Ref. [121] follows a similar approach, although the self-consistent Hamiltonian before rotation is obtained by a different method), the double-sized Hamiltonian in Eq. (4.17), to which the same-sized SOC correction matrix is added after the rotation transformation has been performed, is, in turn, substituted into Eq. (3.25), in which the other matrices have been recast to twice their size and populated on the diagonal blocks corresponding to “up” and “down” spins, where appropriate. Of those matrices, the overlap matrix of the device region S_D , equal for “up” and “down” spins, i.e., independent of spin, has also been rotated by the transformation in Eq. (4.17) after having been recast to twice its size. The equation for the conductance at 0 K and under zero bias then becomes:

$$G = \frac{e^2}{h} [T_{\uparrow\uparrow}(\mu) + T_{\downarrow\downarrow}(\mu) + T_{\uparrow\downarrow}(\mu) + T_{\downarrow\uparrow}(\mu)], \quad (4.19)$$

where the factor of 2 in Eq. (3.29) from spin degeneracy is no longer present because the pure “up” and “down” transmission channels are no longer the same, and mixing of the spins occur due to the non-zero off-diagonal blocks of the rotated and SOC-corrected Hamiltonian in Eq. (4.17).

Finally, as a test of the non-collinear SOC implementation in this work, it is shown that, using literature SOC constants for Fe, significant intrinsic domain-wall magneto-

conductance (DWMC), defined as $\frac{G_{\text{NC}} - G_{\text{sat}}}{G_{\text{sat}}} \times 100\%$ [17], where “NC” stands for non-collinear and “sat” for saturated, can be obtained for an idealised nanocontact attached to uniformly magnetised leads, but with very abrupt transverse head-to-tail domain walls (DWs) of varying width pinned at the constriction. Such DWs form in SLD simulations of cyclic loading of Fe and Ni nanocontacts, though they are not nearly as abrupt. In the particular case of a Fe(001) nanocontact, a few (110) layers form as the nanocontacts are stretched until breaking point (see Fig. 6.4 a)). The spins gradually align in-plane as the separation between these transient (110) planes increases, because the generalised Heisenberg exchange term in Eq. (3.16) aligns the spins locally. (Interestingly, in-plane magnetisation is known to be stable in ultra-thin Fe(110) films on W(110) substrates [209].) The planes form multiple times as the contact thins down towards rupture, such that DWs of different width nucleate and disappear during this process, possibly providing a mechanism for the monotonic decrease in DWMR with increasing DW width observed in permalloy ($\text{Ni}_{80}\text{Fe}_{20}$) nanocontacts very recently [18]. Results on DWMR in Fe and Ni nanocontacts will, however, be discussed in detail in Chapter 7, when the results of the SLD simulations of cyclic loading of Fe and Ni nanocontacts are reported.

Figure 4.13 clearly shows that the DWMR increases as the (abrupt) DW decreases in width. Contrary to the case in which the entire nanocontact is magnetised perpendicular to the transport direction (see Fig. 4.12), there is considerable DWMC in the case when only the single spin on the central atom in the 3-atom chain is oriented along the y axis. Note that literature SOC parameters were used in these calculations, as opposed to the unrealistically large parameters used to obtain appreciable AMC in Fig. 4.10.

The large MR in Fig. 4.13 is thus entirely due to the abrupt domain walls at the constriction, and increases as the domain wall width decreases. It may be rather fortuitous, but the MR is $\sim 50\%$ in the case where the single spin on the central atom is oriented along y . This agrees well with previous theoretical [15] and experimental findings [16,18], however the DWs which form in real nanocontacts in experiments are likely not quite as abrupt, and much lower MR is expected in calculations on realistic SLD nanocontacts in which spin orientations vary more gradually.

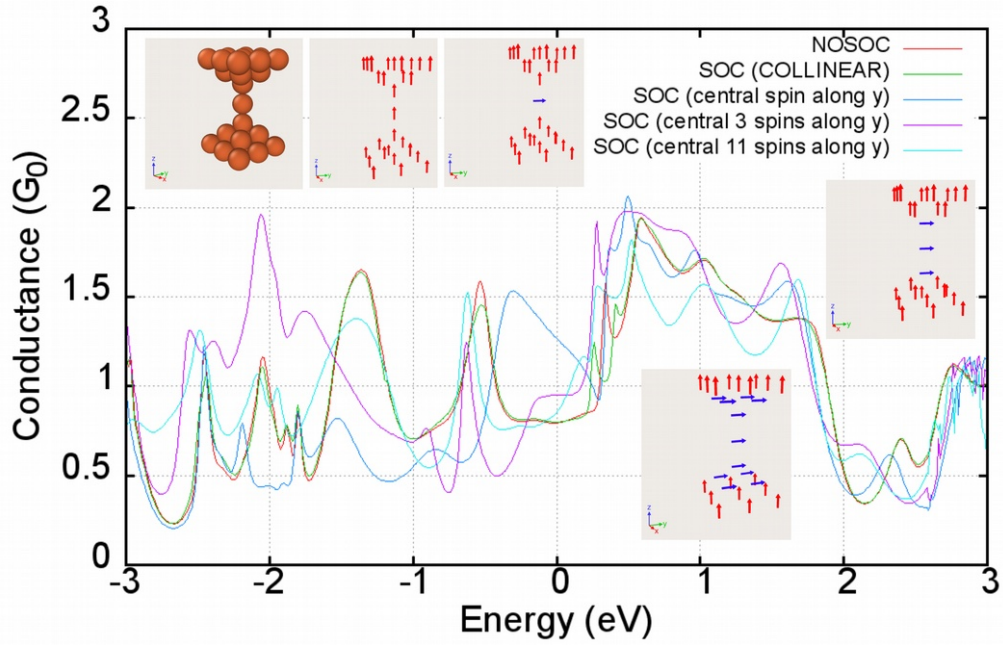


Fig. 4.13: Conductance as a function of energy for the 29-atom Fe (001) input atomic and spin structures shown in the insets, obtained using the implementation of SOC with non-collinear magnetism in ANT.Gaussian in this work. As SOC parameters in ANT.Gaussian, $\zeta_{11} = 0.18$ eV and $\zeta_{22} = 0.06$ eV from Ref. [60] were used. The insets show the very abrupt transverse domain walls imposed using Euler angles $(\theta, \phi) = (90^\circ, 90^\circ)$ on an increasing number of spins in the central region of the contact. As found experimentally [18], the DWMC at the Fermi energy, or zero bias, increases as the domain wall width decreases. There is virtually no difference between the calculation without SOC and with collinear SOC.

This chapter concludes the modification and extension of standard methods needed to model ferromagnetic nanocontacts in this work. In the remaining chapters, the research questions posed in Sec 1.2., will each be addressed in turn. Therefore, the next chapter deals with the influence of relativistic effects on the electronic transport of the noble-metal atoms.

5. RELATIVISTIC EFFECTS IN NON-MAGNETIC METAL NANOCONTACTS: Au, Cu AND Ag⁷

In this chapter, the differences observed in STM/MCBJ experiments between the noble-metal nanocontacts, that is, made of Au, Ag or Cu, are explained. Results from CMD simulations and DFT calculations of electronic transport and force-extension characteristics are presented, resolving the reason for Au's departure from the behaviour expected for the three metals. Two situations are considered: (i) where only a few atoms at most exist at the narrowest region of the constriction, at first contact, and (ii) before physical contact has actually been established, i.e., in the tunnelling regime.

To illustrate the significant differences which are observed experimentally, Fig. 5.1 shows a semi-logarithmic plot of a fit of G_a , the conductance just before contact (horizontal axis), and of G_b , the conductance just after contact has been established (vertical axis), to three bivariate distributions (labelled "1", "2" and "3" for each metal; in blue for Au, red for Ag and green for Cu). These distributions have been constructed from thousands of measurements of conductance for Au, Ag and Cu nanocontacts in a scanning tunnelling microscope at 4.2 K.

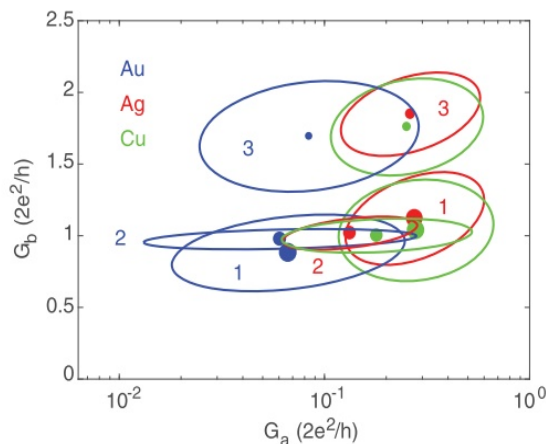


Fig. 5.1: A fit, to the sum of three bivariate distributions, of three experimental distributions obtained from thousands of conductance measurements performed immediately before, G_a , and after, G_b , jump to contact, for Au (blue), Ag (red) or Cu (green) nanocontacts at 4.2 K. The horizontal axis has a logarithmic scale since one order of magnitude in tunnelling conductance is approximately equivalent to 1 Å displacement of the electrodes. The solid circles correspond to the mean conductance value of each fit, and their sizes are proportional to the relative occurrence of the 3 types of distribution for each metal (labelled "1", "2", and "3" for each metal). The outer circles each enclose 1 standard deviation of the data.

⁷ Shorter versions of the material contained in this chapter have been published as Sabater C, Dednam W, Calvo M R, Fernandez M A, Untiedt C and Caturla M J (2018) Role of first-neighbor geometry in the electronic and mechanical properties of atomic contacts *Phys. Rev. B* **97**, 075418, and Calvo M R, Sabater C, Dednam W, Lombardi E B, Caturla M J and Untiedt C (2018) Influence of Relativistic Effects on the Contact Formation of Transition Metals *Phys. Rev. Lett.* **120**, 076802, respectively. ©2018 American Physical Society.

To explain the experimentally observed differences, or lack thereof, between Au, Ag and Cu nanocontacts, the *in-contact* behaviour of the metals, corresponding to the spread in G_b values in Fig. 5.1, is discussed in Sec 5.1. First, the in-contact structures the three metals adopt in CMD simulations are characterised (Sec 5.1.1), along the same lines as in Ref. [42]. Then, in Sec 5.1.2, the results of DFT quantum transport calculations of G_b on first-contact snapshots from CMD simulations, are reported and compared with experimental values.

To explain the anomalously large jump to contact of Au, corresponding to the large offset in mean G_a values between Au and Ag or Cu in Fig 5.1, Sec 5.2 presents the results of plane-wave DFT calculations of the force-extension characteristics of infinite monatomic chains of Au and Ag. This simple yet powerful approach provides a definitive answer to the main question this chapter aims to address.

5.1. Classical molecular dynamics of Au, Ag and Cu nanocontacts

In this section, a previously employed approach, classical molecular dynamics in conjunction with LCAO DFT transport calculations [23], is used to characterise the type of first-contact structures formed by Au, Ag and Cu nanocontacts. Here, the three metals are found to behave more alike, as very much suggested by the distributions in G_b values shown in Fig. 5.1.

It has been shown extensively, by various authors [22,210], including in our own past works [23], that classical molecular dynamics can model contact formation between silver and copper nanocontacts. The best illustration of this is that when an *adatom* is found on an otherwise perfect (111) Ag or Cu surface, that classical molecular dynamics is sophisticated enough to model the smooth contact formation process that is observed experimentally [210,211]. In all other cases, the contact formation process occurs with an abrupt jump. The same is not true of gold, which exhibits a large jump to contact (JC) in all experiments [22]. In our past work [23,24], CMD simulations have not always produced a JC for Au: e.g., when a adatom is on an otherwise clean (111) surface.

5.1.1. In-contact structures and the role of the nearest neighbours

The first-contact structures adopted by Au, Ag and Cu nanocontacts can be classified into three main categories (recall Fig. 2.1): monomers, vertical dimers and double (or higher) contacts. They can be inferred as corresponding to the three different types of distribution in G_b values, labelled “1”, “2” or “3” for each metal shown in Fig. 5.1.

In this section, the three broad categories of first-contact structure formed by the three noble-metals is studied in greater detail by means of CMD simulations of nanocontact evolution under cyclic loading. To that end, the arrangements that first-neighbour atoms adopt in the first-contact structures generated by these simulations, are characterised with a view to assessing their influence on G_b conductance values calculated in Sec 5.1.2.

Figure 5.2 a) shows the input structure used for Au, Ag and Cu (scaled to the lattice parameter of the metal as the case may be) in CMD simulations in this work, and also illustrates the dynamic evolution of the nanocontacts in the simulations of cyclic loading (see the arrows in Figs. 5.2 a) and b)). The input structure in a) is oriented along the (001) crystallographic axis of an FCC lattice because (111) surfaces, which are close-packed, form on the facets on the sides of these contacts. Such facets are the most energetically favourable because each atom in the plane of the surface has the maximum number of immediate neighbours. They are also more likely to form in situations where the contacts are subjected to cyclic loading to a large cross-section, which is done in order to avoid so-called “*mechanical annealing*” in which the same stable structure is formed repeatedly after an initial transient period of cyclic loading [130].

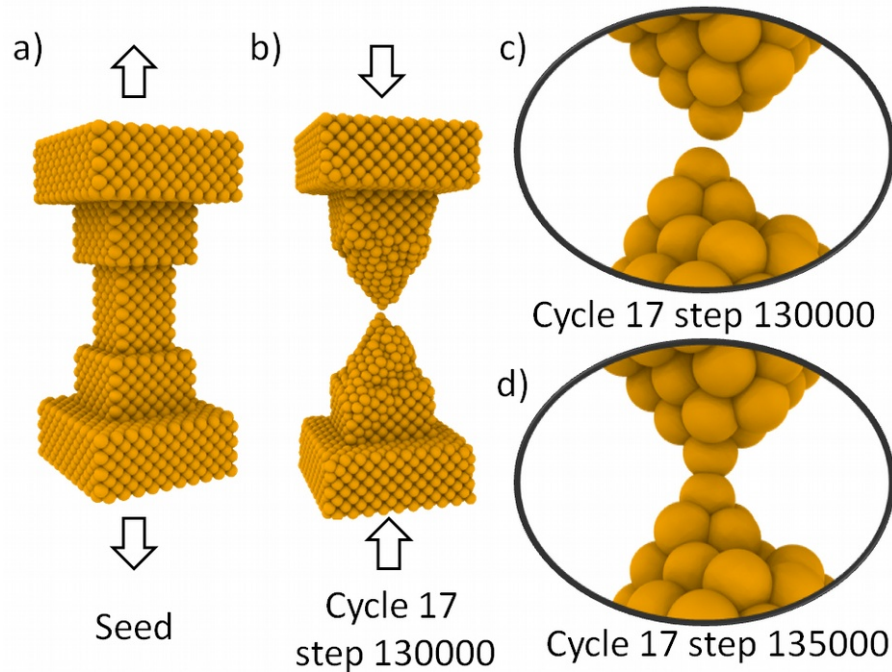


Fig. 5.2: The same 4736-atom (001)-oriented initial input structure is used in CMD simulations of cyclic loading of Au, Ag and Cu nanocontacts at 4.2 K in this work. The only difference is that they are scaled to their respective lattice constants: Au (4.08 Å), Ag (4.08 Å) and Cu (3.61 Å). a) shows the initial input structure used for Au. b) shows the structure just before first contact, after 17 cycles of repeated contact formation and rupture. c) is a zoom-in of b) before jump to contact, and d) after JC, when a vertical dimer has formed.

Repeated contact formation and rupture, i.e., cyclic loading, has been performed over 20 cycles in the CMD simulations reported in this section. A summary of the procedure is provided here:

The Large-scale atomic/molecular massively parallel simulator (LAMMPS) [169] serves to perform the CMD simulations on noble-metal nanocontacts in this work. To describe the interactions between the atoms, the now very well-established EAM potential developed by Wadley *et al.* [44,85] has been used for all three metals. It is an appropriate choice for simulations in which there are free metal surfaces, because among many other parameters, this potential has been fitted to the heat of sublimation of the metals, a surface property. To control the temperature during the simulations, the Nose-Hoover thermostat [212,213] is used, which is deterministic (ergodic) even with the application of external force on the system [146], such as in our simulations where the structures are pulled apart and pushed back together over successive cycles. The temperature is damped to the target temperature of 4.2 K every picosecond (every thousand time steps) by this thermostat, as recommended in the user guide of LAMMPS [169].

Cyclic loading is performed on the Au, Ag and Cu nanocontacts as described in section 4.1, with the exception that the minimum cross-section is not calculated as fractional numbers of atoms as in SPILADY. LAMMPS permits the subdivision of the simulation domain in many ways, for example, in order to tally quantities such as the number of atoms in a sub-region of the simulation domain, as a function of time step. Therefore, in order to count the atoms as the nanocontacts are subjected to cyclic loading, the simulation domain is divided into horizontal slices half a lattice parameter high because the input structures are oriented along the (001) crystallographic orientation of a FCC lattice. Then, the number of atoms are binned into these horizontal slices and written to a file every 5 picoseconds (5000 time steps).

Each simulation starts with the structure being stretched in opposite directions, which is accomplished by freezing the atoms at their equilibrium lattice positions in the three outermost layers at the top and bottom of the nanocontacts, i.e., internally, and displacing the frozen layers uniformly at ~ 1 m/s as illustrated in Fig. 5.2 by the arrows. Recall that this speed is much faster than in the experiments, but still well below the speed of sound of the materials, and so there is enough time for the structure to achieve equilibrium configurations as cyclic loading proceeds [47].

The initial stretching stops when the horizontal slice with the least number of atoms contains exactly zero atoms (the number of atoms in this bin is calculated every 10 picoseconds) and after a further 5 picoseconds of stretching to ensure that the contact has ruptured completely. At this point, the motion of the frozen ends is reversed and contact is re-established until the minimum-atom bin contains 16 atoms, in order to avoid mechanical annealing to sharpened tips, mentioned earlier, and repeated formation of the same stable first-contact structures [130].

There is another reason why this atom-counting algorithm was selected over the original Bratkovsky algorithm used to perform cyclic loading in SPILADY [193]. It allows prediction and classification of the first-contact structures that form, into one of the three categories listed at the beginning of this chapter: vertical dimer, monomer and double (or higher) contacts (recall Fig. 2.1).

Figure 5.3 a) shows the in-contact structure in Fig. 5.2 d) in its entirety and how the simulation domain is sliced up into layers half a lattice constant high (2.04 \AA in the case of Au). Layers 1 and 50 in Fig. 5.3 a) constitute the two outermost frozen layers on each side of the contact. Therefore, layers 2, 3, 48, and 49 are also frozen internally during the simulation. These three outer layers on each side of the contact are displaced in opposite directions away from and toward each other in successive cycles, in order to perform cyclic loading, as described previously. The remaining atoms are free to move and their positions and velocities are updated every time step (1 fs) by the Velocity-Verlet integration algorithm [214,215], which is the standard time integration algorithm implemented in LAMMPS.

Zooming in on the atoms in layers 25-28 in Fig 5.3 a), we can identify, see Fig. 5.3 b), the type of first-contact structure that has been obtained in cycle 17 of contact formation of the Au(001) nanocontact. Binning the numbers of atoms in the layers as a function of time step, produces the contact “profile” shown in Fig. 5.3 c) at the moment when contact is re-established. A closer look at the profile in the inset of Fig. 5.3 c) shows that there are 4 atoms in layer 25, 1 atom in layer 26, also 1 atom in layer 27 and finally, again 4 atoms in layer 28. This allows us to classify the first-contact structure as a 4-1-1-4 vertical dimer. Since we have performed 20 cycles of rupture and contact formation on each of our Au, Ag and Cu nanocontacts, we can in principle classify all the the first-contact structures that form during the 20 times that contact is re-established during the simulations. Doing so, we obtain the results collected in Table 5.1 below.

As can be seen, only the simulated gold nanocontacts (blue entries in Table 5.1) exhibit monomers as the most likely first-contact structure, which is what is also observed in the experiments. (Recall that, for each metal, the size of the central dots inside the bivariate distributions in Fig. 5.1 are proportional to the relative occurrence of the distributions). The reduced statistics (20 data points for each metal) may explain why the other two metals do not always exhibit mostly monomers.

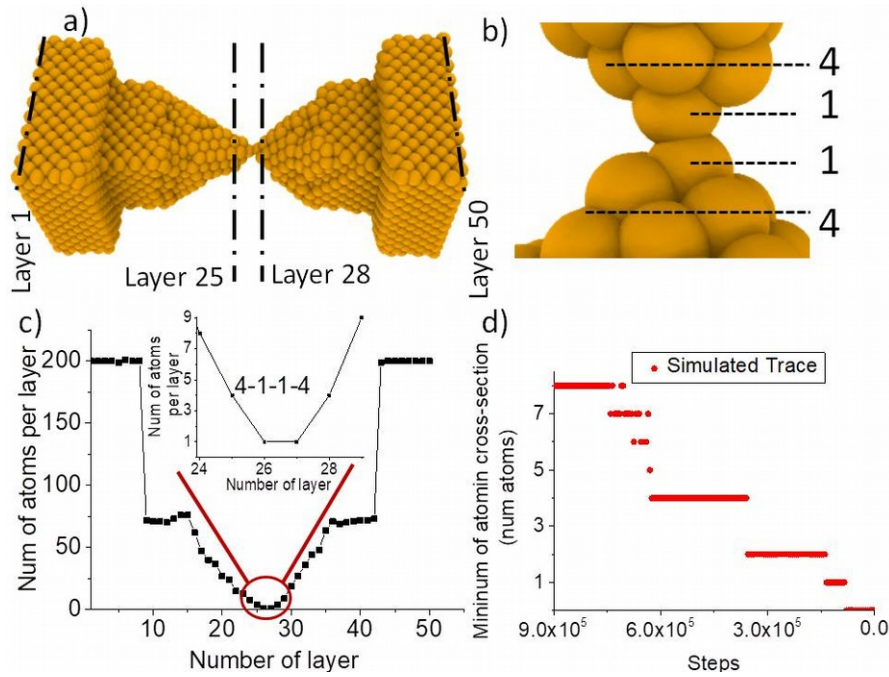


Fig. 5.3: a) shows the in-contact structure formed during the 17th cycle of contact formation of a Au(001) nanocontact undergoing cyclic loading at 4.2 K. b) is a zoom-in of layers 25-28 shown in a). The algorithm that counts the number of atoms in equally spaced layers along the vertical length of the simulation domain, allows us to make a contact “profile” such as in c), and to classify the type of first-contact structure that occurs, a 4-1-1-4 vertical dimer in this case (see the inset in c). The crude atom-counting algorithm also allows plotting a trace of atom number versus time step during one contact formation cycle, as shown in d). This is reminiscent of the conductance traces that are recorded for noble metals during experiments, since they typically exhibit conductance quantisation at integer numbers of the quantum unit of conductance $G_0=2e^2/h$ [11].

To assist the reader in visualising the variety of contacts formed in the CMD simulations, Table 5.2 below shows a schematic representation of the types of contacts obtained, and also shows the extent of coordination of these contacts with first-nearest neighbour atoms.

Note that the blue distribution labelled “2” in Fig. 5.1, for Au, can be used to identify the vertical dimer, since this metal tends to form long monatomic chains upon *rupture*, due to the much higher strength of relativistic effects in late 5*d* metals described in Sec 5.2 [26,67]. Au may not form long chains upon *first contact*, but does form vertical dimers (see Fig. 5.3 b)). The four first-neighbour atoms on each side of the dimer in Fig. 5.3 b) are expected to matter less in conductance measurements, and lead to very narrow distributions in G_b values, especially in the case of Au, in agreement with experiment (see the flat and elongated blue ellipse in Fig. 5.1).

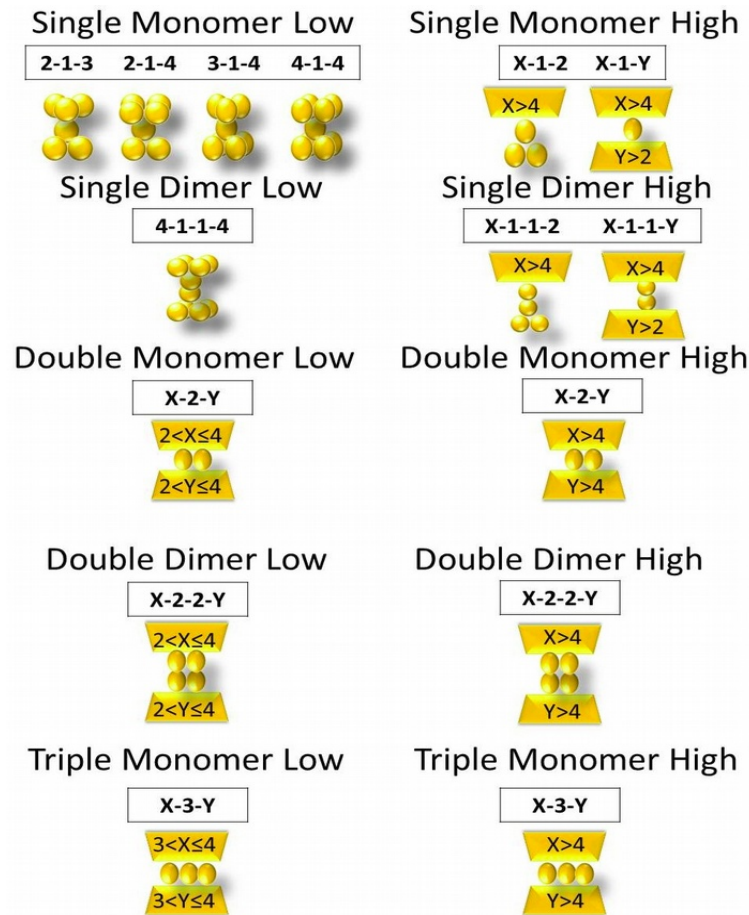
Table. 5.1: Types of first-contact structure and time steps (in ps) at which they form during the contact-formation legs of the 20 loading cycles performed at 4.2 K on Au (blue), Ag (red) and Cu (green) nanocontacts oriented vertically in the (001) crystallographic direction. The scatter in time step at which first contact occurs shows that mechanical annealing [130] to reproducible structures did not occur during the simulations. The entries with asterisks(*) indicate that the atom counting algorithm failed to discern the first-contact structure correctly, and had to be visually inspected to classify them. The nomenclature for the structures with X's and Y's becomes clear upon consulting Table 5.2.

Cycle	kStep	Type	kStep	Type	kStep	Type
1	3090	10-1-2	1545	5-2-5	715	6-3-8
2	145	4-1-2	1410*	X-2-Y*	540	6-3-4
3	285	3-2-5	405	6-1-2	220*	4-1-3*
4	605	2-1-4	395	3-1-2	1055	2-1-6
5	85	4-1-1-4	250	6-2-6	335	5-2-3
6	58	4-3-11	210	5-3-5	185	4-1-3
7	275*	4-3-Y*	320	6-3-5	610	6-2-2-7
8	160	6-1-2	210	6-2-6	285	3-1-4
9	425	7-3-4	255	6-3-5	165*	5-1-4*
10	240	2-1-4	315	6-3-5	525	4-1-4
11	400	4-2-5	255*	6-2-4*	385	3-2-4
12	435*	3-1-2*	320	5-3-5	1060	3-1-6
13	375	7-2-3	255	6-3-5	720*	4-3-5*
14	365	7-1-1-2	240	6-2-6	1260*	X-4-X*
15	200	5-2-3	280	4-1-6	180	8-2-2-4
16	185	2-1-3	305	6-2-6	225	5-1-1-3
17	135	4-1-1-4	210	6-3-5	225*	4-3-7*
18	535	3-1-2	210	6-3-5	265	3-1-1-6
19	340	3-1-2	355	6-3-5	410	8-3-5
20	700	4-2-6	215	6-3-5	160	8-3-4

Finally, double (or higher) contacts are far less likely to occur in experiments and the much higher occurrence of such structures in our simulations, especially for Ag and Cu, reveal the shortcomings of the interatomic potential we used. Another explanation for this discrepancy is the reduced statistics in our calculations: only 20 cycles for each metal.

In the next section the results of scalar-relativistic DFT quantum transport calculations on all the CMD first-contact structures in Table 5.1 are presented.

Table. 5.2: Classification of the types of first-contact structures observed in cyclic loading of Au, Ag, and Cu nanocontacts after 20 cycles. “Low” and “high” refer to the extent of coordination to first neighbour atoms on the either side of the contacts.



5.1.2. Scalar-relativistic quantum transport of CMD snapshots

The ANT.Gaussian conductance values of the in-contact CMD snapshots in Table 5.1, and collected in Table 5.3, correlate reasonably well with the experimental ranges.

In order to assess the conductance values collected in Table 5.3 in terms of the three experimental distributions of G_b values shown in Fig. 5.1, they are grouped (see Table 5.4) into those three types and sub-divided according to the number of first-nearest neighbours surrounding the first-contact atom(s). Contacts with more than four first neighbours on at least one side of the contact are labeled as high (H) coordination, since on a perfect FCC surface oriented along the (001) crystallographic direction, an adatom has four nearest neighbours at most [23].

Table 5.3: First-contact structures from Table 5.1 and the conductance values (in G_0) calculated for them: Au (blue), Ag (red) and Cu (green). The entries with asterisks(*) indicate that the atom counting algorithm failed to discern the first-contact structures correctly, and had to be inspected visually to classify them. For the structures with X's and Y's, the nomenclature becomes clear upon consulting Table 5.2.

Cycle	Type	G[G(0)]	Type	G[G(0)]	Type	G[G(0)]
1	4-1-5	1.26	6-2-6	2.43	6-3-6	3.25
2	3-1-3	0.72	X-2-Y**	0.69	6-3-4	1.71
3	X-3-Y	2.45	4-1-2	0.78	4-1-3	0.84
4	2-1-4	1.58	3-1-2	0.95	8-3-6	2.31
5	4-1-1-5	0.73	6-2-4	1.55	5-4-8	2.54
6	X-3-Y	2.76	8-2-5	1.72	8-3-4	1.58
7	4-3-Y	2.80	8-2-4	1.72	5-1-2	1.04
8	4-1-2	0.84	5-1-5	1.14	6-3-4	2.59
9	7-3-4	2.34	6-2-6	1.80	5-1-4	0.58
10	3-1-4	1.45	6-2-2-6	1.47	4-1-1-6	0.83
11	X-2-Y	2.02	6-2-4	1.85	6-2-4	1.29
12	3-1-2	1.25	6-2-4	1.72	5-4-6	3.14
13	X-2-Y	2.22	6-2-6	1.71	4-3-5	2.47
14	5-1-1-3	0.86	5-1-1-5	0.99	***	1.32
15	4-2-3	1.15	5-1-1-5	0.75	4-2-4	2.02
16	4-1-1-5	1.27	5-1-1-5	0.61	4-1-2	1.00
17	4-1-1-4	0.88	6-2-6	1.66	4-3-7	2.34
18	2-1-4	1.63	6-2-6	1.72	4-1-2	1.14
19	3-1-3	1.35	6-2-6	1.82	8-3-5	1.47
20	4-2-6	2.20	6-2-6	1.75	X-3-Y	1.72

Table 5.4: Conductance values from Table 5.3 grouped according to the classification shown in Table 5.2. "H" refers to high coordination and "L", to low. Mean values and standard deviations are shown. Rows containing "H" values are shown in boldfaced-type for ease of reference.

Type	Mon or dim	Coord	Au	Ag	Cu
Single	Mon.	L	1.4 ± 0.3	0.85 ± 0.12	0.99 ± 0.15
		H	1.26	1.14	0.8 ± 0.3
	Dim.	L	0.88		
		H	1.0 ± 0.2	0.78 ± 0.19	0.83
Double	Mon.	L	1.15		2.02
		H	2.21 ± 0.02	1.73 ± 0.08	1.29
	Dim.	L			
		H		1.47	
Triple	Mon.	L			
		H	2.5 ± 0.4		2.2 ± 0.6

Finally, we compare, see Fig. 5.3, the calculated conductance values collected in Table 5.4 with the experimental first-contact conductance values shown in Fig. 5.1, but with the latter projected onto the vertical G_b axis. The agreement is reasonably good given the simplicity of the interatomic potentials used to generate first-contact structures in our CMD simulations. However, the values calculated from the CMD snapshots, i.e., the blue, red and black markers in Fig. 5.3, with vertical bars denoting the uncertainty, only allows discerning between, on one hand, monomers and vertical dimers (red and black markers), and, on the other, double (or higher) contacts (blue markers). Again, this results from the limitations of CMD simulations as well as the reduced statistics in our theoretical calculations.

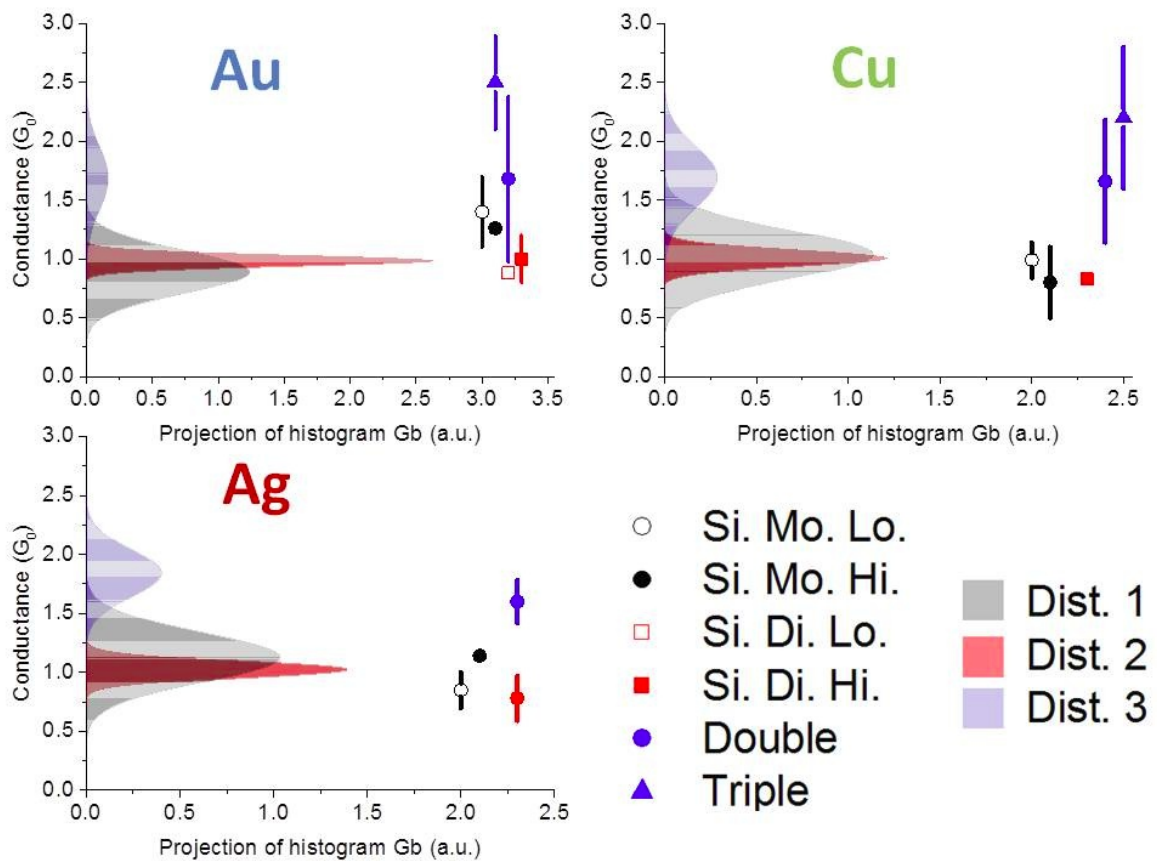


Fig. 5.3: Experimental and theoretical distributions of first-contact conductance values from Fig. 5.1 (shaded areas), and Table 5.4 (markers and vertical bars), respectively, for Au, Ag or Cu nanocontacts at 4.2 K. In the case of the experiments the distributions in Fig. 5.1 have been projected onto the vertical G_b axis. Distributions 1 (grey shading) correspond to monomers, distributions 2 (red shading), given how narrow they are, correspond to vertical dimers, and distributions 3 (blue shading), to double (or higher) contacts. The overall agreement is good, but the simulations only allow us to discern between monomers and vertical dimers, on the one hand, and double (or higher) contacts, on the other. The vertical bars correspond to the standard deviations shown in Table 5.4

Rather surprisingly, in the case of Au, the centre of the experimental distribution of G_b conductance values for the monomers (grey-shaded area), lies slightly below the corresponding centre of the distribution for the vertical dimers (red-shaded area). This contradicts the logic by which a monomer, by virtue of being more “compact”, should exhibit a higher conductance than a vertical dimer, which essentially represents a two-atom monatomic chain. Such a trend can only be explained if the stronger relativistic interactions in Au are also considered, which is the subject of the next section.

5.2. The role of scalar-relativistic effects in Au

The G_a data in Fig. 5.1 have been plotted on a logarithmic axis (the horizontal axis) because, in the tunnelling regime, the distance between the STM/MCBJ electrodes, d , is proportional to the common logarithm (to the base 10) of the conductance $G \propto \exp\left[-\frac{\sqrt{2m\phi}}{\hbar}d\right]$, where m is the mass of the electron, and ϕ is the metal’s work function.

The positions of the centres of the three distributions for Au (shown in blue on Fig. 5.1), along the G_a axis, appears to suggest that Au undergoes a jump to contact about 1 Å earlier than either Ag or Cu, based on the aforementioned relationship between the conductance and interelectrode separation. This is very unexpected, since based solely on the position of the three noble metals in the same group (11) of the periodic table of the elements, bonding between atoms of the same element would be expected to be very similar.

Since differences between these metals, such as the formation of long monatomic chains or surface reconstructions [67], have most recently been attributed to relativistic effects [17], and the approach taken in the last section has in our past work failed to explain the offset in G_a values [24], plane-wave DFT calculations of the force-extension characteristics of monatomic wires, made of Au and Ag, are contrasted in this work to explain the difference.

Qualitatively, the importance of relativity in heavy-element atoms such as 5d Au can be

illustrated in the following way [80]:

The relativistic mass increase $m = m_0 / (1 - (v/c))^2$, where m_0 is the electron rest mass, v is its speed and c is the speed of light, causes the Bohr radius $a_0 = (4\pi\epsilon_0)\hbar^2 / (me^2)$ of the inner electrons to decrease because of their large average speeds. At the non-relativistic limit, we can express this average speed in terms of Z , the atomic number, by combining, on the one hand, the equality of centripetal and electrostatic forces, and, on the other, the Heisenberg uncertainty principle. Doing so, yields $v = Z\alpha c$, where $\alpha \approx 1/137$ is the fine structure constant. Therefore, for a heavy element such as Au, the decrease in the inner $1s$ shell radius will be more than 20% since $v/c = 78/137 \approx 0.57$. Then, firstly, because all the s shells have to be orthogonal to each other, they will contract by a similar amount. In reality, the outer $6s$ shell contracts even more because of interacting shell-structure and relativistic effects [80]. Secondly, non-zero orbital angular momentum electrons, with $l > 0$, i.e., the p, d, f , etc. electrons, undergo spin-orbit splitting, $j = l \pm 1/2$. Finally, the effective potential experienced by especially the d and f electrons, is very well screened by the relativistically contracted s orbitals, since the former never come close to the nucleus as a result of the centrifugal potential $l(l+1)/r^2$. The screening of the outer d and f electrons has the effect of radially expanding their orbitals, since they go up in energy.

All three of the above effects have similar orders of magnitude that increase as Z^2 , and demonstrate the importance of treating heavier elements, such as Au, relativistically.

5.2.1. To what extent do CMD simulations get it right?

Since the interatomic potentials used in CMD simulations in this work have been fitted to experimental data and, typically, by means of scalar-relativistic DFT calculations [44,85], one would expect the simulations to reproduce, at least to some extent, the behavior of Au that can be attributed to relativistic corrections. This is indeed the case, where in our past work [23,24], Au has been prone to undergoing JCs to a greater extent than either copper or silver, but, unlike in the experiments, not in absolutely *all* cases.

Moreover, conductance calculations on CMD snapshots immediately before and after first

contact of Au nancontacts, are unable to reproduce the JC that occurs $\sim 1 \text{ \AA}$ earlier, as compared to Ag or Cu, in the experiments. Then, there are the limitations discussed in Section 5.1.2, where it was shown that conductance calculations on snapshots from CMD simulations permit us to identify two classes of first-contact types, monomers and vertical dimers, i.e., single-atom contacts, on one hand, and double (or higher), i.e., multiple-atom contacts, on the other. The experiments, guided by theoretical results, and our intuition that vertical dimers should produce very narrow conductance distributions centred on a conductance of exactly $1 G_0$ –because a monatomic chain of noble-metal atoms contributes exactly one channel of electronic transmission if spin degeneracy is accounted for [11]– allows for the clear identification of three types of contact. That is, the vertical dimers and monomers can also be distinguished from each other.

But, in order to more rigorously gauge the effect of including or excluding scalar relativistic effects, it is necessary to calculate the relative strength of interaction between the atoms in infinite monatomic chains of Ag or Au. To that end, plane-wave DFT calculations of the force-extension characteristics of the monatomic wires, explicitly including or excluding relativistic and other effects, are carried out in this work.

5.2.2. Relativistic plane-wave density functional theory

To give a definitive explanation as to why Au jumps much earlier into contact (approximately 1 \AA earlier) than Ag or Cu, it is necessary to take recourse to plane-wave DFT calculations. (It is noted that even when plane-wave DFT calculations are performed, the quantum transport problem is still considered in terms of LCAO DFT, for ease of use in the NEGF formalism of transport [124].)

Using the popular plane-wave DFT code CASTEP [64], which permits including or excluding relativistic effects, we calculated the total energy of infinite monatomic wires of Ag and Au atoms (see Fig. 5.4), as a function of their interatomic separation. CASTEP employs high-quality on-the-fly-generated (OTFG) pseudopotentials [178] that are benchmarked against all-electron calculations to within an error of 0.5 meV/atom by the approach discussed in Ref. [172],

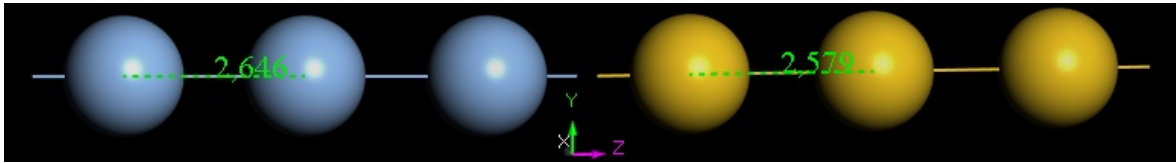


Fig. 5.4: (Left) An infinite monatomic chain of Ag atoms spaced at an equilibrium chain length of 2.646 Å. (Right) An infinite monatomic chain of Au atoms spaced an equilibrium separation of 2.579 Å apart.

The Koelling-Harmon approximation of the Dirac equation [216], which includes all scalar-relativistic effects such as mass-velocity, Darwin and terms of higher order, but excludes spin-orbit coupling (SOC), has been used in the scalar-relativistic total energy calculations within CASTEP. The generalised gradient approximation (GGA) of the electron density, of the Perdew-Burke-Ernzerhof (PBE) flavour, was used as exchange-correlation function.

Although vdWs corrections are considered to play a minor quantitative role in the force-extension characteristics of the bonds between the metal atoms in the infinite monatomic chains considered here [29], the Tkatchenko-Scheffler dispersion-correction scheme [87] has been included in the calculations to assess whether or not vdW interactions contribute to the observed JC behaviour of Au (as discussed in Chapter 2, Sec 2.1).

The plane-wave cutoff used for Au, 400 eV, was taken from Ref. [86]. Silver required the larger value of 600 eV. Convergence with respect to plane-wave cutoff was checked by converging total energies to 5.0×10^{-7} eV/atom. Reciprocal space was sampled by using a $1 \times 1 \times 48$ k-mesh, with 24 k-points in the irreducible wedge of the Brillouin zone, for which convergence of the total energy as a function of the number of these k points was also verified.

As shown in Fig. 5.4, the unit cell of the infinite monatomic chains contained one atom, spaced apart along the z -axis by the equilibrium chain length of each metal, and with ~ 10 Å in the x and y directions, so as to prevent interactions between periodic images in these directions. The equilibrium interatomic spacing in the non- and scalar-relativistic chains, four values in total, was determined by optimising the size of the unit cell in the z direction, using the TPSD algorithm for constrained relaxations [217], until the force fell below 10^{-2} eV/Å. The other dimensions of the cell were held fixed.

Subsequently, the total energy of the infinite monatomic chains was calculated at increments of 0.1 Å, starting from the equilibrium total energy and interatomic separation as the origin in each case (see Fig. 5.5 a)). The equilibrium separations with and without scalar-relativistic corrections are, respectively: Ag (2.65 and 2.74 Å) and Au (2.58 and 2.86 Å). Thus, the scalar-relativistic value for Au (2.58 Å) is in very good agreement with the experimentally established range of 2.5 ± 0.2 Å [129]. The derivative curves in Fig. 5.5 b), i.e., the force-extension characteristics of the monatomic chains, were then calculated from a fit of the total energy data in a) to 6th order polynomials.

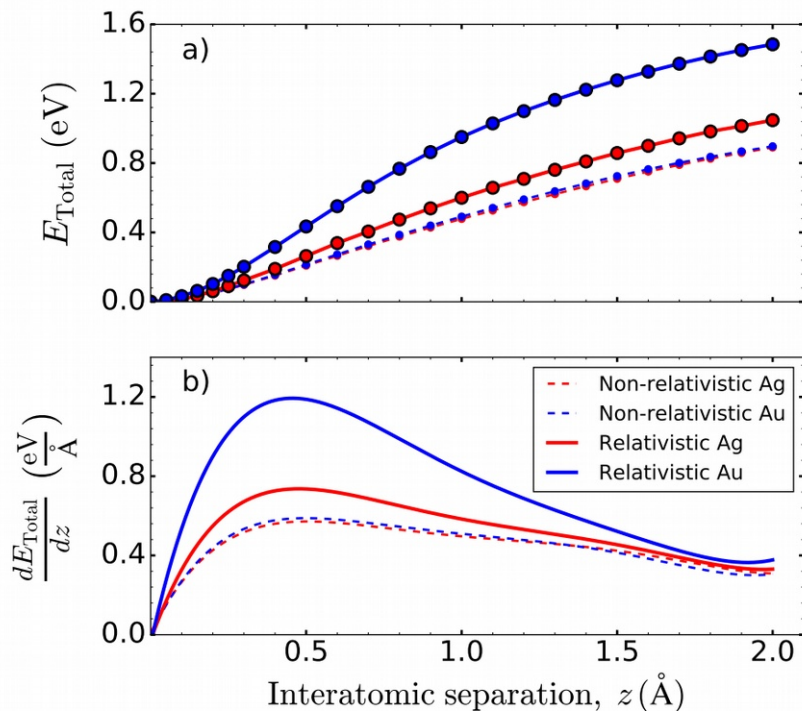


Fig. 5.5: a) Total energy versus interatomic separation of infinite monatomic chains of non-relativistic Ag and Au, and scalar-relativistic Ag and Au. Both the vertical and horizontal axes have been rescaled so that the equilibrium total energies and interatomic separations of each chain coincide with the origin of the plot. b) Derivatives obtained from the total energy data in a), fitted to 6th order polynomials (the solid and broken lines passing through the data points). Clearly, the force-extension characteristics of scalar-relativistic Au stand out compared to the other three cases.

For Ag, as can be seen in Fig. 5.5 b), there is a non-negligible difference between the two types of treatment, non-relativistic or scalar-relativistic, but it pales in comparison with the energy and force as a function of interatomic separation in scalar- and non-relativistic monatomic chains made of Au. The fact that the non-relativistic total energy and force-extension curves, zeroed at their respective equilibrium total energies and interatomic

separations, are virtually identical for Au and Ag, attests to the relative importance played by scalar-relativistic interactions in these metals. In fact, as the separation between the atoms decreases from large values, $\sim 2.0 \text{ \AA}$ above their equilibrium values, the tension in the scalar-relativistic Au chain rises to a value greater than the maximum tension in the scalar-relativistic Ag chain, at a separation 0.7 \AA greater than the separation at which the Ag chain achieves its maximum tension. This agrees surprisingly well with the $\sim 1 \text{ \AA}$ discrepancy between the mean G_a conductance values of Au and Ag observed experimentally (see Fig. 5.1).

Furthermore, we now are in a position to explain why the mean of the distribution in G_b values for Au monomers in Fig 5.3, occurs at a lower value than that of the dimers, first mentioned at the end of Section 5.1.2.

Ag has a very similar bulk FCC lattice constant (4.09 vs 4.08 \AA) and bulk Young's modulus (83 vs 79 Gpa) to Au, so the two metals are expected to adopt very similar geometries as nanocontacts. Therefore, since the interaction between Au atoms on opposing electrodes in a STM/MCBJ setup are very strong as compared to Ag, gold is expected to form highly strained structures upon making first contact (or breaking last contact, when in fact it forms 5-6 atom long chains [26,67]). Additionally, because of the axial symmetry of a vertical dimer and resulting good overlap between wavefunctions of the two members of the dimer, even in strained structures, the mean conductance will be quantised at exactly $1 G_0$, as observed experimentally. However, strained monomers will not be expected to exhibit such good wavefunction overlap because of the disorder in these contact-types as compared to the dimers. Hence, it is not surprising that the mean G_b value for the Au monomers is slightly lower than that of the dimers. This phenomenon, in addition to the much sooner jump to contact exhibited by Au, represents another emergent property, arising from relativistic effects, which influences the quantum transport of Au nanocontacts.

5.2.3. The effects of dispersion interactions and spin-orbit coupling

Considering the converged total energy with and without dispersion corrections, a fit of the total energy data as a function of interatomic separation for non- and scalar-relativistic Au and Ag, produces the force-extension characteristics shown in Fig. 5.6. As pointed out in Ref. [29], it is not surprising that the effect of van der Waal's forces is only quantitatively minor. Therefore, the larger jump to contact in conductance of Au vs Ag or Cu does not arise from van der Waals interactions in these metals.

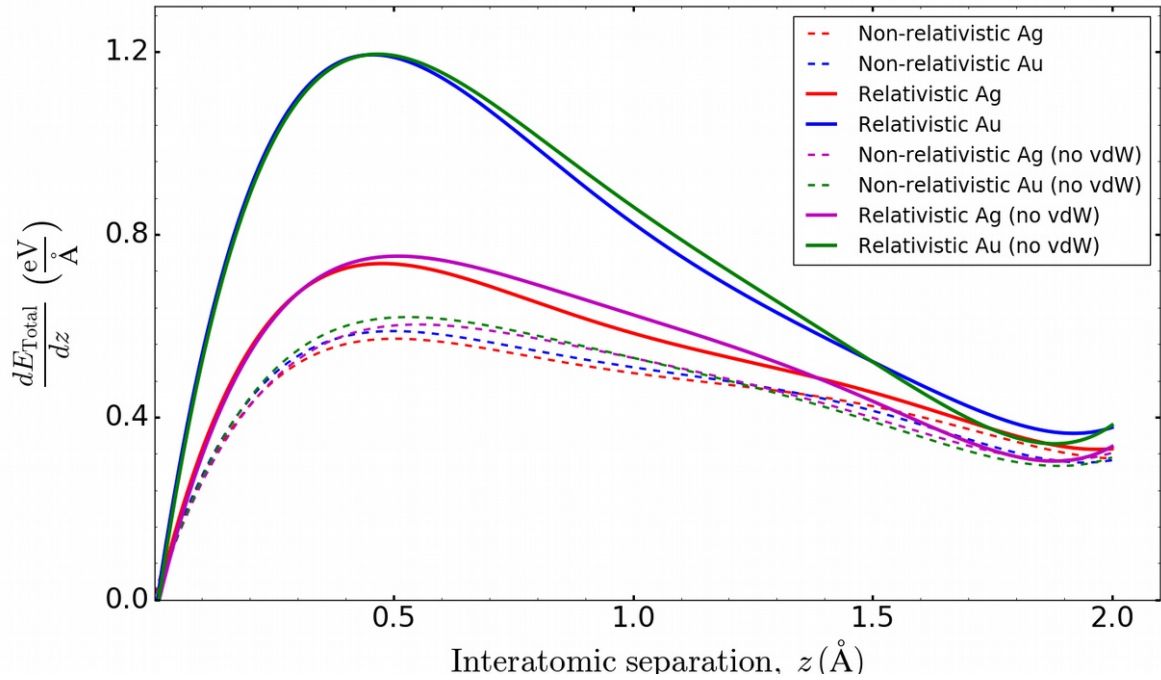


Fig. 5.6: Derivatives obtained from the total energy data in Fig. 5.5 a), fitted to 6th order polynomials, with and without dispersion corrections. The results are virtually identical to those in Fig 5.5 b), showing that, as pointed out in Ref. [29], dispersion corrections only play a minor role in force-extension characteristics of bonding between Ag or Au atoms in an infinite monatomic wire.

Finally, to ensure that the pseudopotential results are robust, all-electron calculations in Wien2K [65] have also been also performed. These results are shown in Fig. 5.7. As exchange-correlation functional, the Perdew-Burke-Ernzhof (PBE) [218] functional was again used. A converged value of 8.0 for the parameter RKMAX, which determines the

total number of wavefunctions in the supercell in Wien2K, was used. Also, a total 700 k points in the irreducible Brillouin zone was enough to ensure smooth total energy versus separation curves (see Fig 5.7), following the same approach as in the pseudopotential calculations reported above. The equilibrium chain length was first determined by optimising the size of the supercell along the z -direction. The obtained equilibrium interatomic separations were virtually identical to those obtained by CASTEP, differing only slightly in the second decimal place at most. Then, starting from the interatomic separation at equilibrium, it was increased by 0.1 \AA at a time, and the total energy was calculated at each separation.

In addition, the all-electron plane-wave calculations permitted an exploration of the effect of (collinear) spin-orbit coupling on the interaction between the atoms in the chains. Using the Wien2k all-electron method, it is possible to determine SOC via a second-variational approach. The scalar-relativistic orbitals from the ordinary spin-polarised calculation in a previous step are employed to that end. The result was a slightly stronger change in energy with interatomic separation than in the scalar relativistic case, but not markedly so (see the broken green curve in Fig. 4.7):

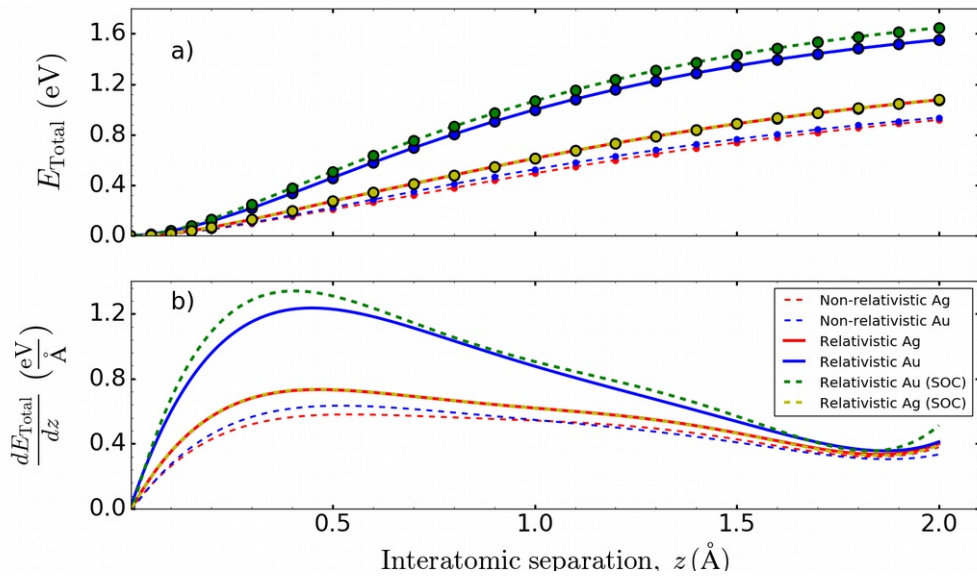


Fig. 5.7: a) Total energy versus interatomic separation of infinite monatomic chains of non-relativistic Ag and Au, and scalar-relativistic Ag and Au obtained in Wien2K. Both the vertical and horizontal axes have been rescaled so that the equilibrium total energies and interatomic separations of each chain coincide with the origin of the plot. b) Derivatives obtained from the total energy data in a), fitted to 6th order polynomials (the solid and broken lines passing through the data points). Clearly, the force-extension characteristics of scalar-relativistic Au stand out compared to the other three cases, in excellent agreement with the results obtained by CASTEP in Fig. 5.5. The addition of SOC makes virtually no difference at all.

It is therefore concluded, based on the results presented in this chapter, that scalar-relativistic effects are responsible for the greater jump to contact in measured conductance observed for Au compared to Ag and Cu. This phenomenon cannot be explained by the effects of vdWs forces, SOC or elasticity only. Scalar-relativistic effects thus have a decisive influence on the emergent transport properties of Au nanocontacts.

6. THE ATOMIC CONFIGURATIONS OF NI AND FE BEFORE RUPTURE

In this Chapter, the types of structures formed by BCC Fe and FCC Ni nanocontacts, near the moment they are about to rupture, are explored.

Section 6.1.1 looks at how the modified embedded-atom method (MEAM) formalism can be used in CMD rupture simulations to generate last-contact structures for Fe nanocontacts that exhibit higher-than-expected atomic coordination in the constriction.

Then, in Sec 6.1.2, the conductance of the most frequent last-contact structures of Fe from CMD simulations, is calculated in scalar-relativistic DFT quantum transport calculations.

Section 6.2.1 provides a comparison with an FCC metal, Ni, using a MEAM potential from the same source as the one used for Fe in Sec 6.1.1.

Finally, Sec 6.2.2 presents conductance results on Ni last-contact structures, calculated in the same manner as for Fe.

6.1. Why theoretical conductance values for BCC Fe nanocontacts are so low

Recall from Chapter 2 that one remaining discrepancy between experiments and previous state-of-the-art simulations is the observed vs predicted position of the first (and essentially only), peak in the conductance histogram of Fe [30] (See Fig. 6.1). Here, to explain this discrepancy, the MEAM formalism is employed to describe interatomic interactions with directional bonding, in an ensemble of CMD simulations of nanocontact rupture in LAMMPS at 4.2 K. For comparison, the simulations are repeated with the best available EAM potential for Fe, developed by Malerba *et al.* in 2010 [43], which does not include directional bonding. The purpose of this comparison is to establish the role of directional bonding in the properties of the nanocontacts and their associated conductance values.

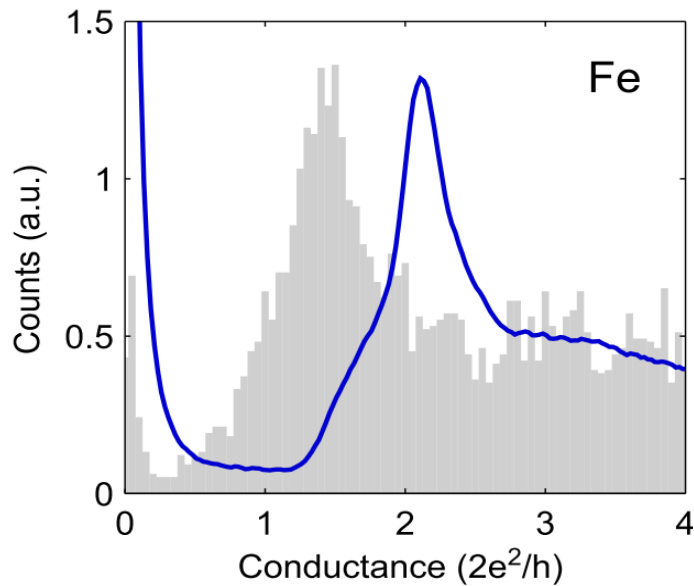


Fig. 6.1: Experimental (thick blue line) and theoretical (grey shaded area) conductance histogram for Fe, extracted from Vardimon *et al.* [30], obtained using EAM potentials, which neglect directional bonding between the Fe atoms in CMD simulations. Although the qualitative agreement between the experimental and theoretical peaks is good, there is an offset of $0.6 G_0$ between them, with the theoretical peak position at about $1.4 G_0$ and that of the experiments at about $2 G_0$.

In Ref. [30], Vardimon *et al.* used a combination of a Slater-Koster tight-binding (TB) approach and the NEGF formalism described in Sect 3.4, to calculate the conductance of small nanocontacts made of ferromagnetic metals (Fe, Ni and Co) and one noble metal (Cu), at the same time as the contacts were being ruptured in CMD simulations with EAM potentials. After performing 100 rupture simulations in LAMMPS [169] at 4 K on each metal, all oriented in the (001) crystallographic direction along the direction of stretching, they obtained enough data to construct conductance histograms with conductance values of up to $4 G_0$ (see Fig. 6.1). The theoretical histograms were directly compared with those recorded during experiments at the same temperature. Very good agreement between experiment and theory was obtained for the FCC metals, Ni and Cu. However, that was not the case for Fe, as previously discussed. The authors attributed the discrepancy to the inability of the EAM potential to correctly reproduce the last contact structures in the case of Fe.

Given that the bonding between atoms is isotropic in the EAM formalism, it seems reasonable that it would be a reliable model for FCC metals, such as Ni, since there are a maximum of 12 first-nearest neighbors about each atom and thus the bonding is highly isotropic. In body-centred cubic (BCC) metals such as Fe, on the other hand, the coordination about each atom falls to 8 first-nearest neighbors, and thus the bonding has greater covalent character relative to FCC or HCP metals.

6.1.1. CMD simulations of Fe nanocontacts: EAM vs MEAM

Figure 6.2 shows histograms of the minimum cross-section, calculated by the Bratkovsky algorithm described in Sec 4.1, for two ensembles of 100 rupture simulations, performed using the initial BCC Fe nanocontact shown in the inset. This initial Fe input structure is oriented along the (001) crystallographic direction. In a given rupture simulation, the minimum cross-section and simulation trajectory are both recorded every picosecond. The simulation time step is 1 fs, as in all previous CMD simulations discussed in this work.

The histogram in Fig 6.2 a) has been constructed by using the most recent MEAM interatomic potential, fitted to the melting point of BCC Fe as well as its near-melting point elastic constants [45]. This particular potential is suitable for simulations of Fe nanocontact rupture because the (001), (110) and (111) exposed surface energies it produces for BCC Fe agrees very well with experiment and DFT calculations [45]. For comparison with an EAM potential, see the minimum cross-section histogram in Fig. 6.2 b). The rupture simulations used to obtain the histogram in b), were performed on the same initial input structure shown in the inset in a), using the best available EAM potential, whose exposed (001), (110) and (111) surface energies also compare well with experiment and DFT calculations [43].

The minimum cross-section data used in Fig. 6.2 was recorded starting 100 ps *before* the moment of rupture in each individual simulation. Rupture was deemed to have occurred when the last two atoms to make contact with each other in the thinning nanocontact, exceeded an interatomic separation equal to halfway between second- and third-nearest neighbors in a perfect BCC lattice of iron, or ~ 2.67 Å. Minimum cross-section data after the moment of rupture was also discarded in constructing the histograms.

The absolute highest maximum in both histograms occurs at nanocontact minimum cross-sections of about 1.5 “atoms”. Both also have a lower maximum below about 1 “atom”. However, in the case of the MEAM potential, there are several peaks at up to even 5 “atoms”, which suggests that more stable structures, i.e., with higher coordination about the few-atom contact, tend to form that are not seen when the EAM potential is used.

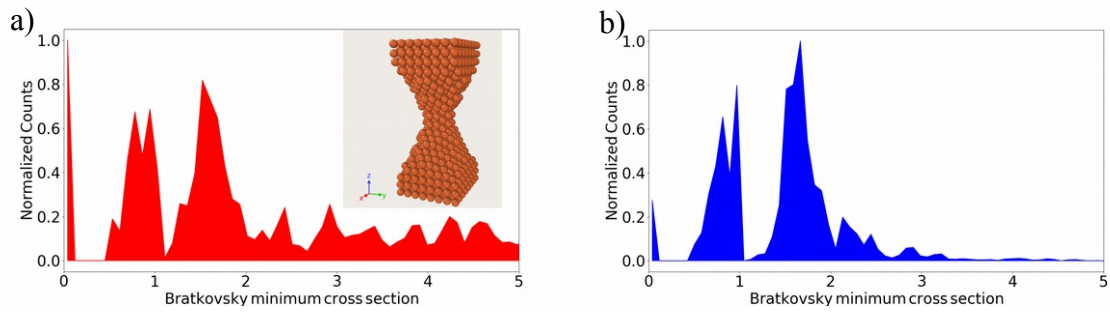


Fig. 6.2: Minimum cross-section histogram obtained after 100 rupture simulations using a) the Etesami and Asadi MEAM potential [45] and b) the Malerba *et al.* EAM potential [43]. 10000 data points have been used to construct each histogram from a larger set that has been truncated 100 ps before rupture and immediately after rupture. The same initial input structure, shown in the inset, was used in both simulations.

Given the good agreement between the two potentials in Fig. 6.2 at minimum cross-sections below ~ 1 “atom” and centred near ~ 1.5 “atoms”, it seems reasonable that the potentials would generate similar structures at those minimum cross-section values, which, in turn, would lead to conductance values contributing to the theoretical peak at $1.4 G_0$ in Ref. [30]. The question remains as to what last-contact structures would be responsible for the experimentally observed peak at $\sim 2 G_0$?

To provide an answer to the aforementioned question, Fig. 6.3 shows a representative sample of the last-contact structures that, according to the Bratkovsky method, have a minimum cross-section above 2.5 “atoms”. Out of the 100 rupture simulations performed, 20 structures broke in this fashion. These structures typically arise when (110) close-packed planes, most favoured in energy in the BCC lattice, form perpendicular to the length of the (001)-oriented Fe nanocontact as it is stretched (see Fig. 6.4. a)). Then, instead of thinning down to a few-atom contact before breaking, the (110)-oriented planes snap or slip apart over the course of a few picoseconds, giving rise to higher than 2.5 “atom” minimum cross-sections in the 100 ps prior to rupture. It is interesting to note that only in 3 out of the 100 simulations with the EAM potential, does rupture take place in this way. Therefore, the MEAM potential, which unlike the EAM potential takes directional bonding into account, produces stable structures in the lead up to rupture that, as we will see in the next section, contributes more to calculated conductance values at and above $2 G_0$ than can be obtained using the EAM formalism.

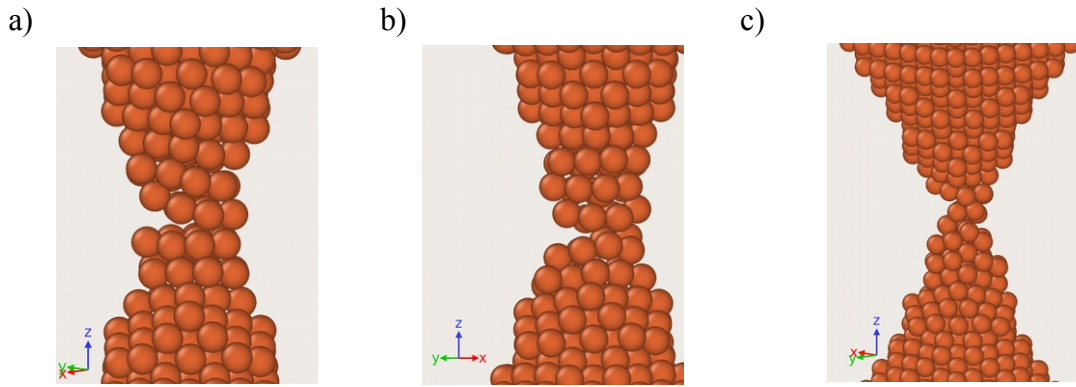


Fig. 6.3: Representative last-contact atomic structures from ruptures in which (110)-planes snap or slip apart over a few picoseconds. With the MEAM potential, in 20 of the 100 rupture simulations, the break occurs in such or a very similar way.

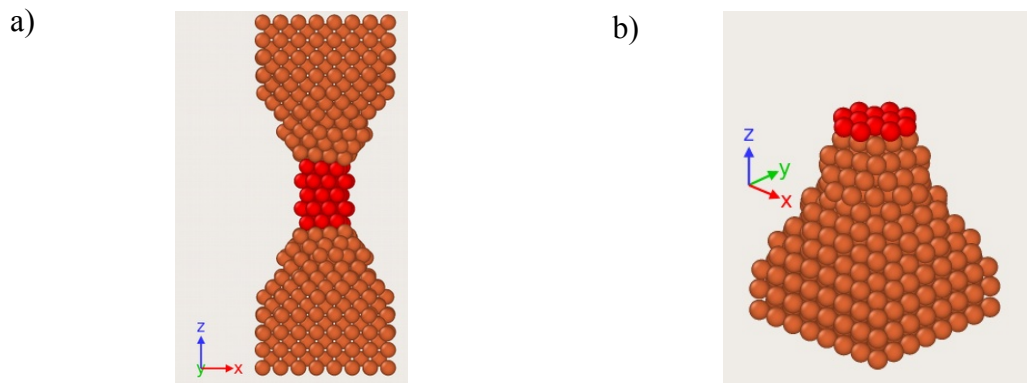


Fig. 6.4: Rupture via (110)-planes snapping apart. a) The BCC nanocontact goes through a phase change under tension, from having (001) to (110) planes (in red) perpendicular to the length of the contact. b) Cut-away of the contact in a), with its top half removed, showing the characteristic 5-atom structure (in red) in the (110) surface of a BCC lattice.

6.1.2. *Scalar-relativistic quantum transport of Fe CMD snapshots*

Table 6.1 below shows the conductance of selected snapshots from the 100 rupture simulations with the MEAM potential, calculated with ANT.Gaussian as explained in Section 3.4. The values have been obtained for a selection of representative CMD snapshots right before rupture. Note that SOC is not included in these calculations and that the magnetism is collinear.

The contact types marked with asterisks(*) were difficult to identify visually and correspond to the type of last-contact structures shown in Fig. 6.3. Note that these structures lead to conductance values at or above $\sim 2 G_0$. Contacts with Bratkovsky minimum cross-sections close to 1.5 “atoms” give conductance values in the range 1.1–1.9 G_0 . Finally, contacts corresponding to the peak at or below 1 “atom” in Fig. 6.2, generally give conductance values in the range 1.0–1.2 G_0 . There are one or two exceptions that do not follow these trends.

Table. 6.1: Contact type, Bratkovsky minimum cross-section and conductance of selected snapshots from 100 CMD rupture simulations with the MEAM potential for (001)-oriented Fe.

Rupture	Type	Min. cross-section	Conductance (G_0)
2	5-3-4	1.6	1.2
5	9-7-8*	4.7	2.4
8	8-6-9*	3.4	2.3
11	2-1-2	0.6	1.0
12	6-6-7*	4.7	2.1
15	5-3-5	1.5	1.4
17	9-6-8*	3.8	2.1
18	5-2-2-5	1.7	1.4
19	7-4-8*	3.2	1.9
34	3-2-2-2	0.8	1.1
40	8-6-9*	4.3	2.1
46	4-2-4	1.5	1.5
49	3-2-5	1.6	1.2
51	4-2-4	1.6	1.3
54	6-3-6*	3.0	2.3
55	4-2-2-5	1.2	1.3
56	5-2-4	1.5	1.3
58	3-2-4	1.4	1.1
60	3-2-4	1.6	1.6
63	4-2-2-5	1.4	1.3
64	5-2-2-5	1.7	1.9
67	5-3-3-5	1.3	1.3
70	3-1-3	0.8	1.2
72	5-2-3	0.8	1.5
73	5-2-3	1.4	1.1
74	3-1-3	0.9	1.0
75	5-2-2-5	1.6	2.0
77	8-7-8*	4.0	2.3
85	8-4-5*	2.8	1.9
88	5-3-3-5	1.5	1.6
91	7-6-10*	4.2	2.5
97	2-1-2	1.0	1.2
99	4-2-3	1.2	1.7

It is important to point out that, unlike in the work of Vardimon *et al.* [30], where a TB model was used to calculate the conductance, *ab initio* methods have been used here. This imposes a much greater computational overhead, since the all-electron basis set for Fe discussed in Sec 4.2 has been assigned to 10-15 atoms in the minimum cross-section, and it is therefore very difficult to obtain enough statistics to reconstruct a full histogram to

compare directly with the experimental one. However, the advantage of the DFT over the TB approach is that the former handles charge transfer and disorder more accurately than the latter [180]. As with the noble-metal nanocontacts in Chapter 5, the CMD last-contact Fe structures have also been trimmed down before being used as inputs in the conductance calculations. The trimmed-down structures are centred on the constriction and contain ~ 200 atoms, in order to make a reasonably large number of DFT transport calculations attainable.

Then, Table 6.2 shows the conductance values for a selection of snapshots from the 100 CMD rupture simulations carried out with the Malerba *et al.* EAM potential. Bratkovsky minimum cross-sections below and at around 1 “atom”, corresponding to the first peak in the histogram in Fig. 6.2 b), lead to conductance values in the range $0.7 - 1.2 G_0$, while cross-sections corresponding to the main peak at around 1.6 “atoms” yield conductance values in the range $1.0-1.6 G_0$.

Table. 6.2: Contact type, Bratkovsky minimum cross-section and conductance of selected snapshots from 100 CMD rupture simulations with the Malerba EAM potential for (001)-oriented Fe.

Rupture	Type	Min. cross-section	Conductance (G_0)
1	4-3-4	2.5	1.2
8	5-2-5	1.6	1.6
10	3-2-2-3	1.5	1.0
13	5-3-3-5	1.7	1.4
16	4-2-3	1.7	1.4
21	3-2-3	1.5	1.4
23	3-2-3	1.7	1.5
24	4-3-6	1.6	2.0
42	4-1-3	0.8	0.9
53	2-1-3	0.7	1.0
69	3-1-2	0.7	0.8
74	2-1-2	0.7	0.7
77	3-1-2	0.7	0.8
80	2-1-2	0.8	1.1
87	2-1-2	0.6	0.7
94	4-2-3	1.3	1.4
98	2-1-2	0.5	0.7

In order to more rigorously assess the conductance values in Tables 6.1 and 6.2, we calculate their so-called Fano factors. In experiments at low temperatures and in the (zero-frequency) linear regime, the Fano factor F provides a measure of noise suppression relative to the maximum Poissonian value of $2eI$ [186]. Therefore, the shot noise from

ballistic transport of electrons through a nanocontact is given by $S_I = 2eIF$, where I is the bias current and e the electron's charge.

On the other hand, in one-component (collinear) DFT quantum transport, the spin-polarised conductance can be expressed as [186]

$$G = \frac{G_0}{2} \sum_{n,\sigma} T_{n,\sigma}, \quad (6.1)$$

where G_0 is the usual spin-degenerate quantum of conductance and $T_{n,\sigma}$ are the individual spin-resolved ($\sigma = \uparrow$ or \downarrow) eigenchannels, indexed by integer n . Since not only the geometry but also the number of atoms in the constriction of a nanocontact determines the overall conductance through the valence orbitals of the atoms, the individual spin-resolved transmission channels can convey information about the atomic structure of the contacts via the Fano-factor (a measure of the number of partially open transmission channels in the nanocontact):

$$F = \frac{\sum_{n,\sigma} T_{n,\sigma} [1 - T_{n,\sigma}]}{\sum_{n,\sigma} T_{n,\sigma}}, \quad (6.2)$$

Figure 6.5 a) shows the Fano factor calculated for CMD snapshots corresponding to the conductance values in Tables 6.1 (red markers) and 6.2 (blue markers). The dark grey areas correspond to forbidden values of F for magnetic nanocontacts, while light grey areas correspond to forbidden values for non-magnetic nanocontacts.

Because the Fano factor is a measure of the number of partially open transmission channels in a nanocontact, the more channels contribute to the overall conductance, the more atoms are likely to be involved. The experimental Fano factors for Fe, taken from Ref. [30], are shown in Fig. 6.3 b).

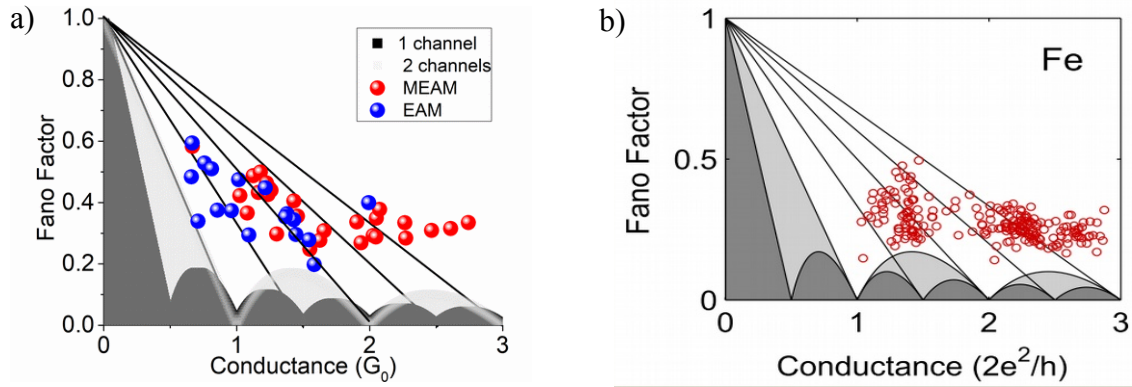


Fig. 6.3: a) Calculated conductance values from Tables 6.1 and 6.2 plotted on a Fano Diagram. The diagonal lines each correspond to the number of spin-resolved transmission channels, in this case from 1 to 6, in units of $1/2 G_0$. The agreement with the experimental values extracted from Ref. [30] in b) is quite remarkable, especially for the CMD simulations with the MEAM potential. The light-grey areas correspond to forbidden values of F for non-magnetic materials, while the dark-grey areas correspond to forbidden values for magnetic materials. Note that more significant figures have been included in a) than are shown in Tables 6.1 and 6.2.

For the MEAM potential, the calculated conductance values in Fig. 6.5 a) agree remarkably well with those in the experimental Fano diagram in Fig. 6.5 b). Experimentally, Fe prefers to form last-contact structures with around 6 spin-resolved transmission channels (in units of $1/2 G_0$), which from the values of the Bratkovsky minimum cross-sections in Table 6.1, indicate last-contact structures that are 3 or more atoms across. The MEAM potential, with more covalent character, therefore seems to outperform the EAM potential in reproducing realistic stable last-contact structures for Fe.

In fact, based solely on the low density of states of Fe at the Fermi level [145], in comparison with Ni or Co, one would expect Fe to have a first highest maximum conductance peak at a lower conductance value than either of the other two metals (see Fig. 6.6). The experimental Fano diagram in Fig. 6.5 b) exhibits a significant number of conductance values at this expected low value, but in a histogram, they are subsumed by the broad peak at $\sim 2 G_0$ (see the experimental histogram for Fe in Fig. 6.6, taken from Ref. [144]), because BCC Fe nanocontacts tend to become much more disordered than, say, the more crystalline FCC Ni contacts, as will be shown in the next section. The resulting measured conductance values are very smeared out by the disorder.

Therefore, we postulate that the discrepancy between the experiments and the simulations in the work of Vardimon et al [30], for the case of Fe, is the lack of CMD structures of

large enough minimum cross-sections at rupture (above 2.5 “atoms”), when using an EAM potential, in combination with a tight-binding model to calculate the conductance. If the calculations using the Etesami and Asadi MEAM potential used in this work were to be repeated at a later date, it is expected that the result in Ref. [30] would be markedly improved.

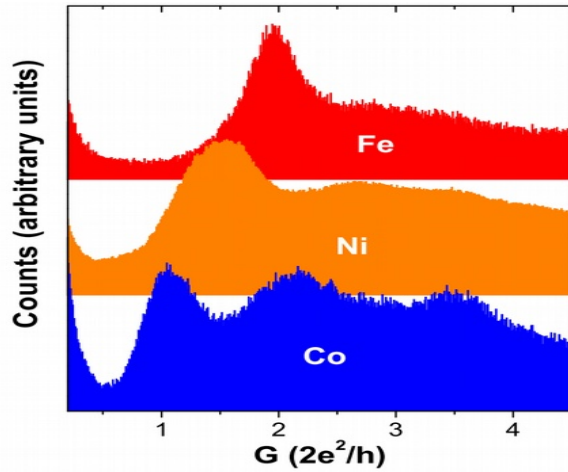


Fig. 6.6: Experimental conductance histograms recorded for Fe, Ni and Co, taken from Ref. [144]. Fe exhibits an unusually high first peak at around $2 G_0$ and no other apparent peaks. Based solely on its density of states at the Fermi level, its first peak should occur at a lower conductance value than either Ni or Co, if it also formed single-atom atomic contacts such as monomers or vertical dimers at last-contact like the other two metals. Instead, last contacts with more than three atoms in the minimum cross-section are preferred, see the histogram in Fig. 6.2 a) and Table 6.1, which explains the unusually high position of the conductance maximum of Fe.

In conclusion, conductance calculations on stable last-contact structures generated in CMD simulations of Fe rupture, using an interatomic potential that accounts for covalent bonding, yield values that agree with the peak in Fig 6.6 at $\sim 2 G_0$. Covalent bonding thus plays a decisive role in the type of atomic configurations adopted by Fe before rupture.

In the following section, the results of MEAM and EAM CMD simulations of Ni nanocontact rupture, along two different crystallographic orientations, are presented. It is interesting to compare this FCC metal with BCC Fe that was the subject of the present section.

6.2. Comparison with an FCC ferromagnetic metal: nickel

EAM potentials very much favour first- or last-contact structures consisting of single-atom contacts such as vertical dimers and monomers [40–42,75] (see also Table 5.2). In the case of a monovalent FCC metal such as Cu, the outer $4s$ valence orbital in the single atom bridging the contacts in these most-probable structures, gives rise to conductance

quantisation at exactly $1 G_0$ [7], the first maximum in the conductance histogram. While, for a multi-valent FCC metal such as Ni, which, in addition to the $4s$ valence orbital, also possesses $3d$ orbitals that cross the Fermi energy and contribute to transport slightly above $1 G_0$, a first maximum peak at around $1.5 G_0$ occurs in the conductance histogram. The last-contact structures that supposedly give rise to this peak in Ni correspond to monomers and vertical dimers. However, the peak is very broad in the case of Ni, and, as explained in Chapter 2, vary between experiments, with some histograms exhibiting a double peak. As also described above, there could be many contributing factors to this: zero-bias anomalies such as the Kondo effect [36,37], the formation and pinning of magnetic domain walls at the constriction [15,32,101,104], the localised spin-minority spd bands which are very sensitive to the precise geometry of the contacts [15], etc.

To address the role of the geometry of the contacts in the appearance of disparate conductance histograms for Ni, referred to above and in Chapter 2, we consider the type of atomic configurations adopted by this metal before rupture in CMD simulations (Sec 6.2.1). As in Sec 6.1.1, we contrast results produced by MEAM and EAM potentials. In addition, the simulations have been performed in two different crystallographic orientations: along (001) and (111).

In Sec 6.2.2, the conductance of selected (001)- and (111)-oriented structures, generated with the MEAM potential, are presented. Conductance values calculated from EAM CMD structures are reported in the next chapter, since SLD simulations carried out in SPILADY are limited to EAM potentials.

6.2.1. CMD simulations of Ni nanocontacts: EAM vs MEAM

In Chapter 2, we saw that Ni nanocontacts usually exhibit only a single broad low-conductance maximum in experiments (see Figs. 2.2 a) or 6.6), or more rarely, two peaks (see Fig 2.2 b)). Previously, the origin of the twin peaks in the latter case had not been explained to a satisfactory extent. Here, as in Ref. [40], we consider the possibility of two different crystallographic orientations for Ni nanocontacts (along (001) or (111)), but also evaluate the ability of the EAM potential (which does not include directional bonding) vs

the more advanced MEAM potential (which includes directionality) in generating atomic configurations before rupture that can be used to distinguish the two types of histogram.

Moreover, in this section, it re-emphasized that the type of bonding in the metal, and the ability of the potential to accurately reproduce this bonding, is responsible for the discrepancy between theory and experiment in the case of Fe. To that end, the simulations described in Sec 6.1.1 have been repeated for Ni using the MEAM potential from the same source, Ref. [45], and the EAM potential developed by Zhou *et al.* [85], which was used for Au, Ag and Cu in Chapter 5.

Figures 6.7 a) and b) show the minimum cross-section histograms obtained from two sets of 100 rupture simulations, one generated with a MEAM potential and the other with an EAM potential, using the (001)-oriented initial Ni nanocontact shown in the inset of a).

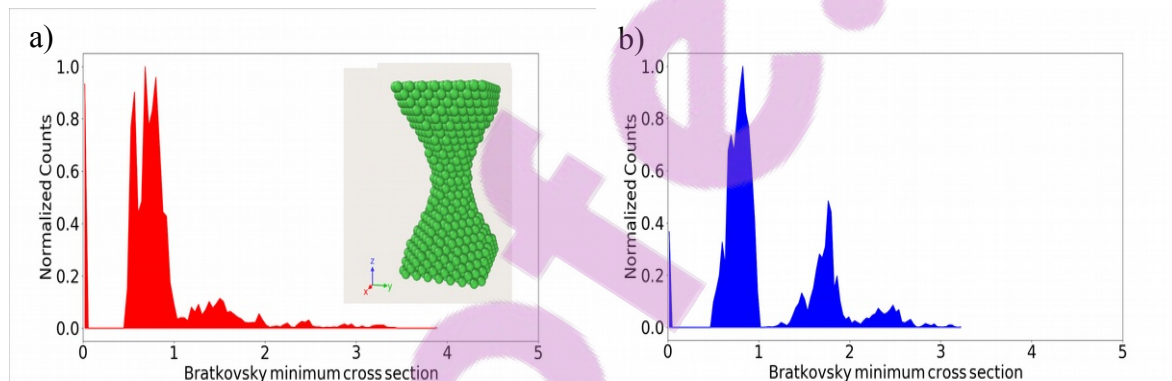


Fig. 6.7: Minimum cross-section histogram obtained after 100 rupture simulations using a) the Etesami and Asadi MEAM potential [45] and b) the Zhou *et al.* [44] EAM potential. 10000 data points have been used to construct each histogram from a larger set that has been truncated 100 ps before rupture and immediately after rupture. The same initial input structure, shown in the inset, was used in both simulations.

If we compare these histograms with those of Fe shown in Fig. 6.2, the most striking difference is the occurrence of a first highest maximum peak slightly below one “atom” in both cases. Clearly, both the MEAM and EAM potentials generate single-atom structures for the FCC metal Ni with a much higher probability than in the case of BCC Fe. This supports the contention in this work that the parent crystal structure of the metal, which in turn is determined by the degree of covalency of bonding between the metal atoms in the lattice, has a decisive influence on the type of structures adopted by the daughter nanocontacts when they are about to break. The greater covalent nature of the bonding in

BCC iron appears to favour the formation of more compact structures, whereas single-atom contacts such as monomers are the exception. This is most accurately reflected by the MEAM potential which is able to take directional bonding into account, as opposed to the EAM potential, which does not.

Having established that monomers and dimers are the most favoured last-contact structures in FCC Ni, we now attempt to explain the twin-peak conductance histogram sometimes exhibited by this metal. To that end, 100 rupture simulations were also performed for a (111)-oriented initial Ni nanocontact (see the inset in Fig. 6.8 a)). Only the MEAM potential was used in this case. In Fig. 6.8 a), there is no longer just a single prominent peak, but more, at almost integer values of the number of “atoms”.

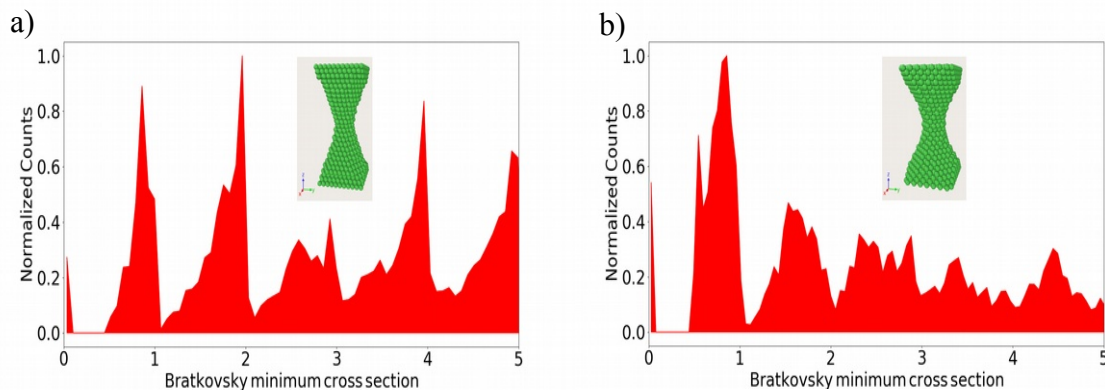


Fig. 6.8: Minimum cross-section histogram obtained after 100 rupture simulations using the Etesami and Asadi [45] MEAM potential for a) a (111)-oriented nanocontact (inset) and b) the (001)-oriented nanocontact from before. 85000 data points have been used to construct each histogram.

Comparing the histogram in Fig. 6.8 a) for a (111)-oriented nanocontact, with the one in b) for a (001)-oriented nanocontact, further underlines that (001)-oriented nanocontacts are favoured in the majority of experiments, since most experimental histograms for Ni only exhibit a single broad and prominent peak at $1.5 G_0$ as in Fig. 6.6 (see also Fig. 6.9 below). In this case, the data has not been truncated 100 time steps before rupture as in the Sec 6.1.1, but only immediately after rupture. That is why peaks at higher cross-sections are observed. The reason for doing so becomes clear when the histograms in Fig. 6.8 are compared with the two experimental histograms in Fig. 6.9.

The orange histogram in Fig 6.9 below, with a single prominent peak, is obtained most often (see also Fig. 6.6), while the grey one, with many peaks at almost integer values of the conductance, is a rare exception.

The shapes of the minimum cross-section histograms in Fig. 6.8 imply that the grey experimental histogram in Fig. 6.9 corresponds to the minimum cross-section histogram in Fig. 6.8 a), for a (111)-oriented nanocontact, whilst the orange histogram corresponds to the one for the (001)-oriented nanocontact in Fig. 6.8 b).

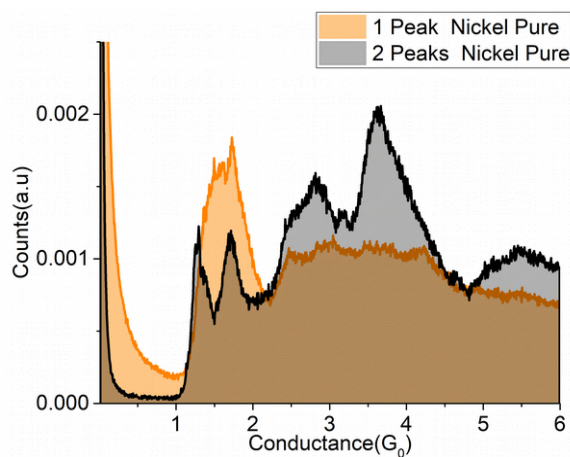


Fig. 6.9: Experimental conductance histograms recorded for the rupture of Ni nanocontacts at 4.2 K by Carlos Sabater at the Weizmann Institute of Science in Israel.⁸ Notice how the grey histogram, exhibiting the twin peaks at low-conductance values, also has peaks at higher conductance values, and compare this with Fig. 6.8 a) for the (111)-oriented Ni nanocontact, ruptured 100 times in CMD simulations with the MEAM potential. Likewise, compare the orange experimental histogram with the one constructed from 100 rupture simulations of a (001)-oriented Ni nanocontact in Fig. 6.8 b).

In contrast, when using an EAM potential to simulate rupture of a (111)-oriented nanocontact, the agreement with experiment is no longer as good, as Fig. 6.10 below shows. The EAM potential (Fig. 6.10 b)) does not reproduce the clear peaks at integer minimum cross-section in Fig. 6.10 a). In fact, the histogram in Fig 6.10 b) resembles more that of the (001) orientation in Fig 6.8 b). Here, again, the data has not been truncated 100 time steps before rupture, but only immediately after rupture. That is why peaks at higher cross-sections are observed.

⁸ Private communication with Dr. Carlos Sabater.

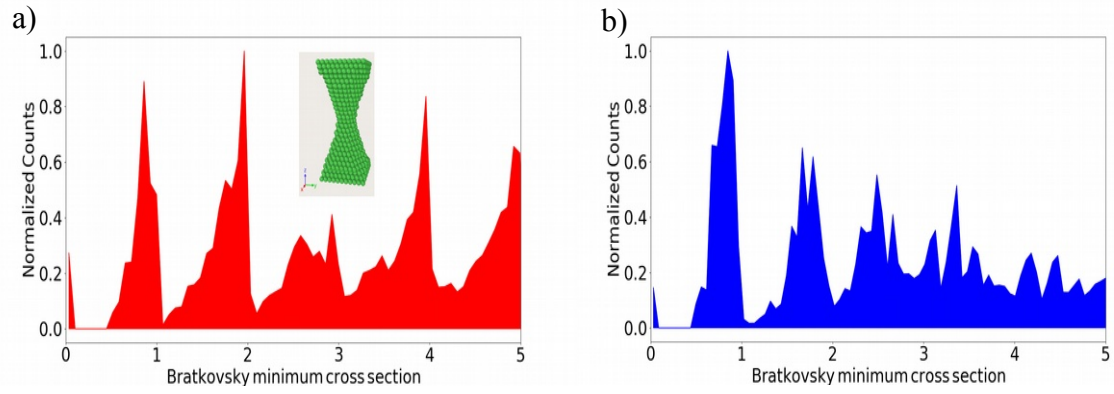


Fig. 6.10: Minimum cross-section histogram obtained after 100 rupture simulations using a) the Etesami and Asadi MEAM [45] potential and b) the Zhou *et al.* [44] EAM for the (111)-oriented Ni nanocontact in the inset. 85000 data points have been used to construct each histogram. The EAM potential in b) does not exhibit the clear peaks at integer values of Bratkovsky “atoms” which the MEAM potential has produced in a).

Therefore, even when covalent bonding is expected to play a minor role, as in FCC metals such as Ni, an interatomic potential that takes directional bonding into account produces better agreement with experimental results, at least in terms of a comparison of the shapes of the minimum cross-section and experimental conductance histograms, than an EAM potential in which the bonding is isotropic.

6.2.2. Scalar-relativistic quantum transport of Ni CMD snapshots

In this section, DFT quantum transport results are reported for selected stable (001)- and (111)-oriented Ni last-contact structures, extracted from 100 CMD rupture simulations of each orientation, performed using the MEAM potential. Table 6.3 shows the results for the simulations performed on the (001)-oriented nanocontact shown in the insets of Figs. 6.7 a) and 6.8 b).

Table. 6.3: Contact type, Bratkovsky minimum cross-section and conductance of selected snapshots from 100 CMD rupture simulations with the MEAM potential for (001)-oriented Ni.

Rupture	Type	Min. cross-section	Conductance (G_0)
6	4-1-3	0.5	1.3
21	4-1-1-2	0.6	1.3
46	5-1-1-2	0.5	1.5
54	5-1-1-2	0.5	1.5
61	4-1-2	0.6	1.6
68	4-1-2	0.7	1.5
72	4-1-2	0.6	1.8
90	4-1-3	0.5	1.5
96	3-2-3	1.0	2.0

Table 6.4, on the other hand, shows the results for the simulations performed on the (111)-oriented nanocontact shown in the insets of Figs. 6.8 a) and 6.10 a).

Table. 6.4: Contact type, Bratkovsky minimum cross-section and conductance of selected snapshots from 100 CMD rupture simulations with the MEAM potential for (111)-oriented Ni.

Rupture	Type	Min. cross-section	Conductance (G_0)
3	3-1-1-3	0.8	1.6
14	3-1-1-3	0.8	1.6
15	3-1-1-3	0.8	1.5
16	4-1-1-3	0.8	1.0
18	4-1-2	0.9	1.4
51	4-1-1-4	0.8	1.4
62	5-1-1-4	0.9	1.5
85	4-1-2	0.7	1.6
91	2-1-2	0.8	1.8

The conductance results for the (001) orientation ($\sim 1.55 \pm 0.23 G_0$) and for the (111) orientation ($\sim 1.49 \pm 0.21 G_0$) both give values that are higher than the peak at lowest conductance in the (grey) experimental histogram in Fig. 6.9. This is likely the result of not having performed cyclic loading to stable structures in the Ni simulations described here (see Chapter 7). It is therefore not possible, at this stage, to draw a sharp conclusion about the origin of the grey histogram in Fig. 6.9 with peaks at 1.2 and 1.5 G_0 , respectively, being attributable to the (111) crystallographic orientation of the nanocontacts, vs the orange histogram with the single peak corresponding to the (001) crystallographic orientation.

Nevertheless, comparing the results for Fe and Ni in this chapter proves conclusively that covalent bonding, and not necessarily the type of interatomic potential used in CMD simulations, leads to the unexpectedly high position of the conductance maximum in histograms for Fe.

In Chapter 7, the effect of non-collinear magnetism on the electronic transport properties of Ni and Fe last-contact structures, generated in SLD simulations, is explored. The contribution of magnetic domain walls to the low-conductance features of experimental histograms of these metals are assessed, while SLD simulations of cyclic loading are used to clarify that (111)-oriented Ni nanocontacts correspond to the grey histogram, and (001)-oriented Ni nanocontacts, to the orange histogram, in Fig. 6.9.

7. THE ROLE OF FERROMAGNETISM AND UNIAXIAL MAGNETIC ANISOTROPY IN FE AND NI NANCONTACTS

The extension of the spin-lattice dynamics model that has been implemented in this work and is described in Chapter 4, allows a study of not only the evolution of the atomic structure during rupture, but also of the evolution of the spins. In this chapter we extend the classical molecular dynamics simulations of Ni and Fe nanocontacts in Chapter 6, by also including the evolution of spins, in order to evaluate the effect of domain-wall magnetoresistance (DWMR) on the low-conductance features of the metals' experimental conductance histograms.

The results of SLD simulations of the cyclic loading of (001)- and (111)-oriented Ni, and (001)-oriented Fe nanocontacts, at 4.2 K, are presented in Sections 7.1.1 and 7.2.1, respectively. Nanocontacts with a (001) crystallographic orientation are mainly considered because they are the most favourable, in energy terms, for FCC and BCC metals in experiments where cyclic loading is performed to large contact cross-sections. However, to contrast the results in this chapter with those from the last, (111)-oriented Ni nanocontacts are also considered.

Thereafter, the results of conductance calculations on selected snapshots of atoms and spins from the SLD simulations, are presented in Sections 7.1.2 for Ni, and Sec 7.2.2 for Fe. The purpose of these calculations is to explore the influence of magnetic domain walls on the conductance of the nanocontacts at last-contact, compared to uniformly magnetised, or fully saturated, structures. The conductance results for Ni along the (001) and (111) crystallographic orientations are additionally assessed in terms of whether they clearly assign the grey double-peak histogram in Fig. 6.9 to (111)-oriented Ni nanocontacts.

7.1. Magnetic domain walls in (001)- and (111)-oriented Ni nanocontacts

If very abrupt (planar) domain walls make a significant contribution to magnetoresistance of Ni nanocontacts at last contact, even in the absence of an externally applied magnetic field, as speculated in Ref. [32], then clear evidence of the formation of DWs should be seen in SLD simulations performed in this work.

In the present SLD simulations, only magnetisation directions consistent with a ferromagnetic arrangement of the spins are considered in the frozen layers, at both far (bulk) ends of the nanocontacts. The spins are most likely nearly fully ferromagnetically ordered in bulk samples of the metals at very low temperatures such as 4.2 K, which is the temperature regime in which STM/MCBJ experiments are conducted.

Furthermore, only results for “small” Ni and Fe nanocontacts (~400 atoms) are reported. The purpose of this is to avoid artificially introduced domain walls near the frozen ends of the contacts when the SLD structures are trimmed down to fewer atoms for DFT quantum transport calculations, as explained in previous chapters.

7.1.1. Cyclic loading of (001) Ni nanocontacts

For the SLD calculations presented in this section, C_2 has been made negative in Eq. (4.2) for Ni ($C_2 = -0.5$ eV), which makes DWs much more likely to form than experimentally. The reason for making $C_2 < 0$ is to determine the maximum possible extent of DWMR. When $C_2 < 0$, the spins tend to align perpendicularly to the length of the nanocontact during SLD simulations, creating artificial domain walls pinned at the constriction of the nanocontacts. The magnitude of C_2 is chosen so that, with the exchange parameters of Ni ($J_0 = 832.72789$ meV and $r_c = 4.33$ Å)⁹, the spin temperature does not exceed the lattice

⁹ Obtained from a fitting to Eq. (3.17) of *ab-initio* data of pairwise exchange energies between a central Ni atom and atoms in successive nearest-neighbour shells of FCC Ni. The *ab initio* data was very generously shared by Dr. Leo Ma, one of the developers of SPILADY, in a private communication.

temperature as occurs when too large a value of C_2 was used for Fe during thermalisation at 800 K (see Fig. 4.6).

Figure 7.1 shows last-contact snapshots of representative atomic and spin configurations out of 13 ruptures performed in cyclic loading simulations of a 380-atom (001)-oriented Ni nanocontact. The structures are arranged in order of decreasing magnitude of the calculated magnetoresistance (see Sec 7.1.3), with the vertical dimer in Fig. 7.1. a) exhibiting the maximum DWMR (about -12% , see Table 7.1) among all the simulations.

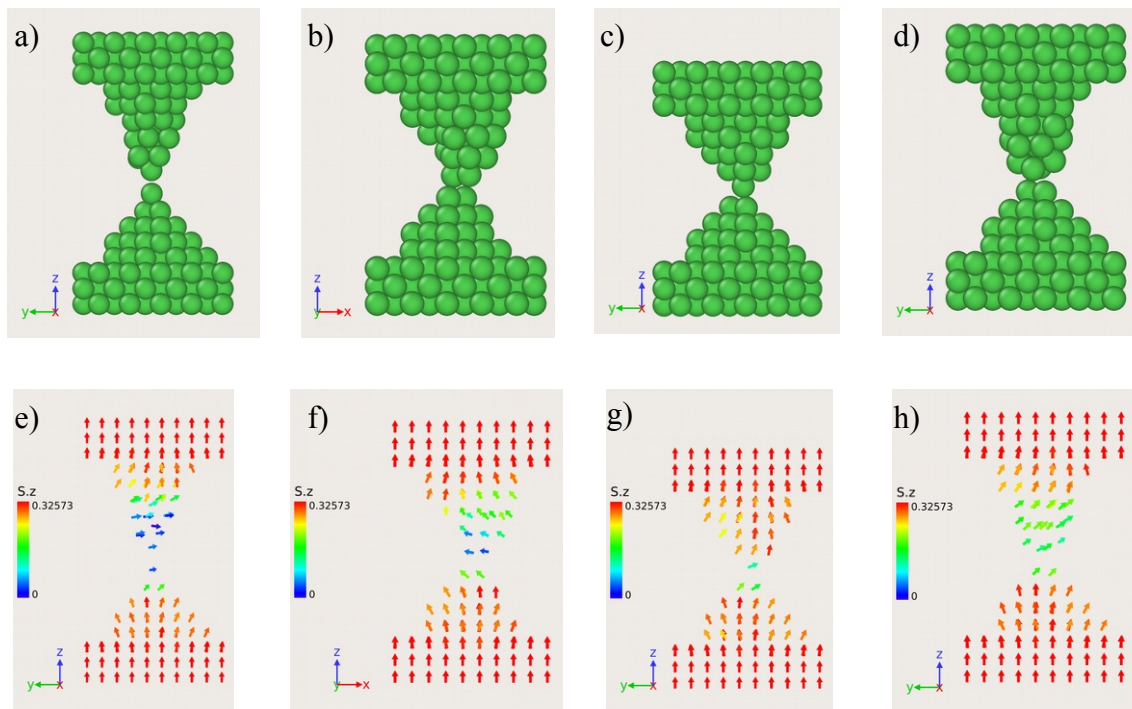


Fig. 7.1: Representative last-contact atomic and spin structures from ruptures after 13 cycles of cyclic loading of a 380-atom (001)-oriented Ni nanocontact: a) vertical dimer, b) double contact, c) monomer and d) another double contact. The double-contact structures only occurred once each. Monomers occurred predominantly. The structures are ordered in decreasing magnitude of DWMR: e) -12% , f) -7% , g) $+4\%$ and h) $+1\%$. The color legend corresponds to the projection of the spins (in μ_B) on the positive z -axis, the direction of saturation magnetisation of Ni, $0.65 \mu_B$ divided by the electron's gyromagnetic factor: 2.002319 .

It is seen that the DWMR increases as the spin angles deviate more from the spin quantisation axis along z , and that it is maximum for the vertical dimer in Fig. 7.1 a), a two-atom chain, in agreement with the preliminary results for the three-atom Fe chain (trimer) in Fig. 4.13. This is expected because the magnetic domain wall is more abrupt. The role of atomic disorder on the extent of abruptness of DWs and magnitudes of their

associated DWMR is also illustrated by comparing Figs. 7.1 b) and d), or for the spins, f) and h). There is relatively greater disorder in the structure in Fig. 7.1 d) compared to b), and thus the spins in Fig. 7.1 h) vary more gradually than in f), and hence the DWMR of h) is smaller.

7.1.2. Cyclic loading of (111) Ni nanocontacts

We now consider (111)-oriented Ni nanocontacts. As before, the magnetisation is set along the long axis of the nanocontacts. Figure 7.2 again shows representative atomic and spin configurations of 12 ruptures in cyclic loading SLD simulations of a 417-atom (111)-oriented Ni nanocontact.

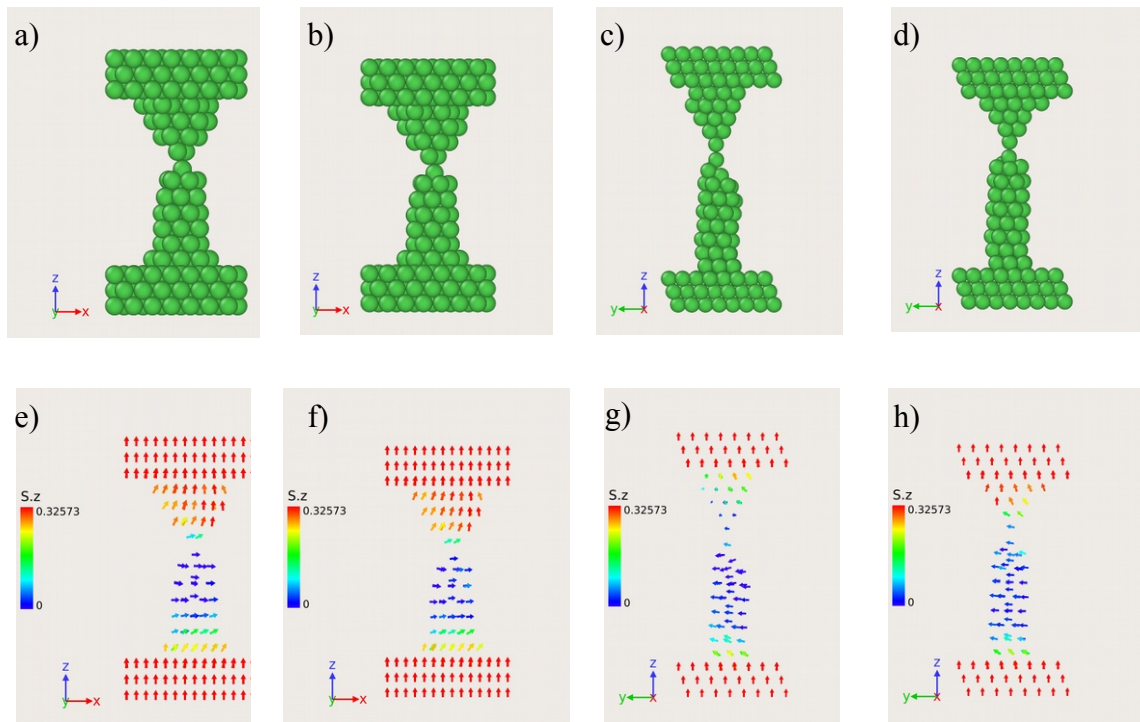


Fig. 7.2: Representative last-contact atomic and spin structures from ruptures after 12 cycles of cyclic loading of a 417-atom (111)-oriented Ni nanocontact: a) monomer, b) monomer, c) vertical dimer and d) vertical dimer. No double contacts occurred and roughly equal numbers of dimers and monomers occurred in the 12 cycles. Note the elongated pentagonal structures that form during rupture of (111)-oriented contacts in agreement with Refs. [40,41]. The structures are ordered in decreasing magnitude of DWMR: e) +30%, f) -17%, g) -12% and h) -8%. The color legend corresponds to the projection of the spins (in μ_B) on the positive z -axis, the direction of the saturation magnetisation of Ni, $0.65 \mu_B$ divided by the electron's gyromagnetic factor: 2.002319.

The structures in Figs. 7.2 a) and b) are shown from a different perspective than the structures in c) and d), as indicated by the coordinate tripods in each figure. Once more, the structures are arranged in decreasing order of the magnitude of DWMR (see Sec 7.1.3), with Fig. 7.2 a) exhibiting the maximum DWMR ($\sim 30\%$).

On comparison with the results from Chapter 6 for (001)- and (111)-oriented Ni nanocontacts, it is again evident here that the (111)-oriented nanocontacts exhibit more ordered structures which allow for greater DWMR since disorder tends to prevent domain walls from forming.

It is highly unlikely that the extended domain walls in Fig. 7.2 would form in reality since C_2 in Eq. (4.2) has deliberately been chosen to lead to the formation of domain walls at the constriction. A negative value favours spins aligning perpendicularly to the length of the nanocontact. Most ferromagnetic materials with uniaxial magnetocrystalline anisotropy have positive values of this constant [195]. The deviation of the spins from the z -axis is thus expected to be rather less when this constant is positive. Nevertheless, these calculations confirm that the DWMR is low and we obtain values in agreement with those measured experimentally (no higher than 30% in the best-case scenario), as described in Chapter 2. Therefore, DWMR on its own cannot account for the grey conductance experimental histogram, with the twin-peak structure, shown in Fig 6.9.

The next section presents the conductance results, used to calculate the DWMR reported in Figs 7.1 and 7.2, of snapshots from SLD simulations at last-contact, with spin-orbit coupling and collinear and non-collinear spin orientations taken into account as discussed in Chapter 4, Section 4.2.

7.1.3. Vector-relativistic quantum transport of Ni SLD snapshots

In this chapter, the role of non-collinear magnetism in Ni and Fe nanocontacts is explored in the absence of an external magnetic field. The purpose of this is to establish whether DWs might contribute to the unexpected features observed in conductance histograms of these metals.

Table 7.1 records the conductance, with spin-orbit coupling, as implemented in Chapter 4, of 13 last-contact structures obtained in SLD simulations of cyclic loading of a 380-atom Ni(001) nanocontact. The values are consistent with the results from the previous chapter for the type of last-contact structure also shown in the table. Again, single-atom contacts dominate as is expected when an EAM potential is being used as in the last chapter.

Table. 7.1: Contact type, Conductance (G_0) with collinear and non-collinear SOC, and domain-wall magnetoresistance (%) of snapshots from SLD simulations with the Zhou *et al.* EAM potential for Ni (001).

Rupture	Type	SOC-COLL (G_0)	SOC-NC (G_0)	DWMR (%)
1	3-1-1-4	1.19	1.27	7.31
2	2-1-1-4	1.65	1.62	-1.43
3	2-1-3	1.77	1.79	1.15
4	4-2-6	2.50	2.53	1.08
5	2-1-1-4	1.72	1.51	-12.16
6	4-2-2-5	2.20	2.0	-7.44
7	2-1-4	1.97	1.99	1.11
8	2-1-4	2.00	2.05	2.64
9	2-1-4	1.83	1.86	1.66
10	2-1-4	1.86	1.92	3.57
11	2-1-4	1.99	2.02	1.83
12	2-1-4	1.97	1.99	1.39
13	2-1-4	1.94	1.98	2.14

Then, in Table 7.2, the conductance results for a 417-atom Ni(111) nancontact are shown after cyclic loading for a total of 12 cycles. Once more, single-atom contacts dominate and the conductance values are consistent with the type of contact.

Table. 7.2: Contact type, Conductance (G_0) with collinear and non-collinear SOC, and domain-wall magnetoresistance (%) of snapshots from SLD simulations with the Zhou *et al.* EAM potential for Ni (111).

Rupture	Type	SOC-COLL (G_0)	SOC-NC (G_0)	DWMR (%)
1	2-1-2	1.55	1.56	0.32
2	2-1-1-3	0.92	0.89	-4.12
3	2-1-1-3	1.24	1.09	-12.06
4	2-1-1-3	1.09	1.11	1.61
5	2-1-1-5	1.36	1.24	-8.09
6	2-1-1-3	0.90	0.89	-1.11
7	2-1-5	1.36	1.41	3.99
8	2-1-5	1.59	1.32	-17.36
9	2-1-5	1.60	1.79	12.45
10	2-1-5	1.28	1.65	29.19
11	2-1-5	1.36	1.57	14.92
12	2-1-5	1.64	1.70	3.78

Here, the conductance of (111)-oriented Ni nanocontacts are clearly lower than their (001)-oriented counterparts. Under cyclic loading, the EAM potential used here favours the formation of longer and narrower stable last-contact structures in the case of (111)-oriented nanocontacts, i.e., the pentagonal wires observed in Refs. [40,41]. Longer and narrower nanocontacts give rise to lower conductance values on average at last contact. However, in contrast to Refs. [40,41], where pentagonal wires formed preferentially in (001)- and (110)-oriented Ni nanocontacts, the cyclic loading performed in our SLD simulations favours the formation of pyramid-shaped tips in the (001)-orientation. The reason for this is that (111)-oriented close-packed facets form on the sides of the pyramids during cyclic loading, which are highly favoured in energy terms.

Even though the shapes of the minimum cross-section histograms obtained with the MEAM potential in Chapter 6 allowed us to tentatively assign the grey histogram in Fig. 6.9 to (111)-oriented Ni nanocontacts, and the orange histogram to the (001)-oriented nanocontacts, the conductance values of selected snapshots from those simulations were essentially the same.

Unlike the SLD simulations discussed in this chapter, the nanocontacts in Chapter 6 were not subjected to cyclic loading in the CMD simulations, which might explain the difference between the last-contact conductance results presented in Tables 7.1 and 7.2, on one hand, and Tables 6.3 and 6.4, on the other. But the fact that the conductance values reported in this chapter for the (111)-oriented nanocontacts are lower than their (001)-oriented counterparts, also implies assignment of the grey conductance histogram in Fig 6.9 to (111)-oriented Ni nanocontacts.

What role does DWMR then play in all of this, one may ask? From the results reported in Tables 7.1 and 7.2 for Ni(001) and Ni(111), respectively, it appears that even when $C_2 < 0$ in Eq. (4.2), favouring the formation of transverse domain walls, only modest values of DWMR are obtained, in agreement with previous work [18]. Also, the fact that the sign of the DWMR is not always in the same direction, agrees with the behaviour observed for the Kondo resonance in ferromagnetic Fe, Ni and Co nanocontacts [37].

Briefly, the Kondo resonance arises in Ni nanocontacts at first- or last-contact, where the coordination about atoms is low, because the spin-minority electrons in a localised d orbital that is hybridised with sp orbitals, become anti-ferromagnetically coupled to the itinerant electrons in the sp orbitals. The dynamic screening of the magnetic moment on the localised d orbital by the itinerant electrons in the sp channels, modifies the conductance of the few-atom nanocontacts as described in Ref. [144], which contains a comprehensive discussion of the Kondo resonance.

Consequently, disentangling the various factors that contribute to the sign of the DWMR is no simple matter. For both DWMR and the Kondo resonance, described previously, the spd hybridised minority spin channel is very sensitive to the precise geometry of the contacts. The overall effect is that DWMR will on average tend to cancel out and only contribute to broadening of conductance peaks, much as what happens in the case of the Kondo resonance. Therefore, in contrast to toy models, such as infinite monatomic chains of Ni, for which up to 250% DWMR has been calculated (see references in Ref. [15]), in realistic Ni nanocontacts, DWMR can be excluded from making a dominant contribution to the low-conductance twin-peak structure exhibited in the grey histogram in Fig. 6.9.

7.2. Magnetic domain walls in (001)-oriented Fe nanocontacts

In this section, the results of cyclic loading of a 308-atom Fe(001) nanocontact is presented. It is clear from Chapter 6 that DWMR is not the cause of the unexpectedly high position of the conductance peak of Fe in experimental histograms. Nevertheless, it remains interesting to explore the effects of DWMR on the calculated conductance values, since the low-conductance features of Fe and Ni conductance histograms, until now not fully explained, are one of the main objectives of this work. These features correspond to the types of stable last-contact structures adopted by nanocontacts made of these metals.

7.2.1. Cyclic loading of (001) Fe nanocontacts

Figure 7.3 shows four last-contact structures in order of decreasing magnitude of the DWMR (see Sec 7.2.2). They have been generated with $C_2=0.1$ eV in Eq. (4.2). This value has been chosen to avoid the spin temperature exceeding that of the lattice as in Fig. 4.6 a). As expected, when $C_2>0$ in Eq. (4.2), the spins deviate rather little from the z -axis in highly disordered nanocontacts near the moment of rupture.

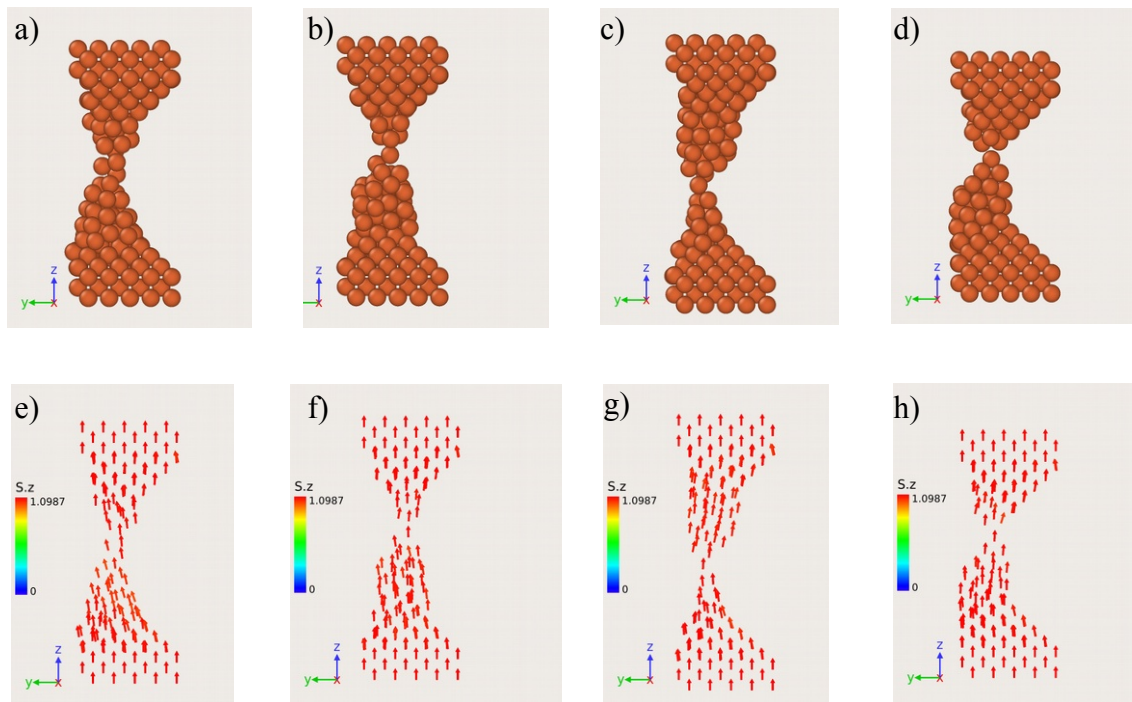


Fig. 7.3: Representative last-contact atomic and spin structures from ruptures after 10 cycles of cyclic loading of a 308-atom (001)-oriented Fe nanocontact: a) double contact, b) monomer, c) monomer and d) another monomer. Double contact structures only occurred twice. Monomers occurred 8 times. The structures are ordered in decreasing value of DWMR: e) +1.9%, f) +1.9%, g) +1.2% and h) +1.2%. The color legend corresponds to the projection of the spins (in μ_B) on the positive z -axis, the direction of the saturation magnetisation of Fe, $2.2 \mu_B$ divided by the electron's gyromagnetic factor: 2.002319.

It is not generally the case that DWs do not form in Fe or Ni nanocontacts during the evolution of their structure and cross-sections during cyclic loading in SLD simulations. In fact, at larger cross-sections when nanocontacts are still highly crystalline, DWs sometimes nucleate at the constriction even when $C_2>0$.

For instance, when Fe nanocontacts undergo a phase change from (001) layers to (110) layers as in Fig. 6.1 a), the spins briefly align in-plane in the (110) layers to form a transverse domain wall in SLD simulations. It has been found experimentally that the magnetisation tends to align in-plane in (110) Fe layers on W(110) surfaces [209]. However, the behaviour of the nanocontacts at wider cross-sections is not reported here, since we are interested in the stable last-contact structures these metals adopt before rupture.

As reported in the previous literature, Fe is expected to exhibit very low DWMR because the ratio of majority to minority spin density of states at the Fermi level is lower than in Ni or Co, and hence the extent of spin-polarisation is limited [145]. Therefore, spin-lattice coupling is not expected to systematically affect the type of stable last-contact structures adopted by Fe nanocontacts. The next section presents the conductance values of 10 ruptures from cyclic loading of the 308-atom Fe(001) nanocontact shown in Fig. 7.3 above, confirming the aforementioned assertion regarding the influence of spin-lattice coupling on the low-conductance features of Fe nanocontacts.

7.2.2. Vector-relativistic quantum transport of Fe SLD snapshots

In order to show that DWMR makes a negligible contribution to the low-conductance features of Fe conductance histograms, Table 7.3 on the next page shows the values obtained for last-contact structures generated with the Malerba *et al.* EAM potential, since the MEAM potential has not been implemented in SPILADY and magnetic anisotropy parameters are, at present, not available for either Fe or Ni in LAMMPS.

The conductance values in Table 7.3 are consistent with the type of last-contact structure generated by the Malerba *et al.* EAM potential. As can be seen in the far-right column, DWMR is small in Fe nanocontacts when only a few atoms remain in the minimum cross-section before rupture. The main conductance peak at $2 G_0$ of Fe can thus only be explained by the extent of covalent bonding between its atoms, at or close to last contact, and not by DWMR, which, as for Ni, can also be enhanced (positive) or reduced

(negative). DWMR is thus again seen to lead to broadening of the peak in the conductance histogram of Fe, but not to determining its position.

Table. 7.3: Contact type, Conductance (G_0) with collinear and non-collinear SOC, and domain-wall magnetoresistance (%) of snapshots from SLD simulations with the Malerba *et al.* EAM potential for Fe.

Rupture	Type	SOC-COLL (G_0)	SOC-NC (G_0)	DWMR (%)
1	4-2-2-4	1.734	1.733	-0.075
2	2-1-1-2	0.674	0.667	-0.94
3	4-1-3	0.778	0.792	1.88
4	2-1-3	0.845	0.855	1.19
5	3-2-3	0.940	0.944	0.39
6	3-2-2-3	1.005	1.024	1.88
7	2-1-3	1.140	1.153	1.16
8	4-2-2-4	1.767	1.743	-1.36
9	5-2-2-4	1.267	1.277	0.63
10	4-2-3	1.542	1.529	-0.85

In conclusion, DWMR will, at the very most, contribute to broadening peaks in conductance histograms of Ni and Fe nanocontacts, and thus cannot explain their low-conductance features. The DWMR results reported in this chapter for snapshots from SLD simulations of cyclic loading Fe and Ni nanocontacts, however, underline the suitability of the methods developed and extended in Chapter 4 to model these structures, since they agree with the consensus estimates of DWMR reported for these metals in previous works.

8. CONCLUDING REMARKS

In order to tackle the study of both ferromagnetic and non-magnetic metallic nanocontacts, the following models have been applied and extended:

- The spin-lattice dynamics (SPILADY) developed by Ma *et al.* [48] has been extended to include magnetic anisotropy and non-collinear magnetism for nanostructures. This model has been parameterised for Fe and Ni.
- Spin-orbit coupling has been implemented in the electronic transport code ANT.Gaussian. The method has been validated by comparison to vector-relativistic self-consistent calculations done in OpenMX.

These calculations and implementations required making use of different simulation packages such as ANT.Gaussian, OpenMX, CRYSTAL14, CASTEP and Wien2K for DFT, as well as LAMMPS and SPILADY for classical molecular dynamics and spin-lattice dynamics.

The extended methods have been applied to study metallic nanocontacts, ultimately providing new insight into the two research questions that were posed. Concerning the first research question, about the much larger jump to contact measured in the conductance for Au, than in either Ag or Cu, we have seen that:

- A study of the stability of atomic contacts in the three metals, Au, Ag and Cu, via a combination of DFT and CMD, reveals that electronic transport across these structures depends crucially on the number of first neighbours.
- Relativistic effects explain the enhanced bonding in Au compared to Ag or Cu and consequently the experimental observations in jump to contact behaviour, which cannot be explained by any other proposed factors such as van der Waal's forces, spin-orbit coupling, or elastic constants along different crystallographic orientations.

Concerning the second research question regarding the extent to which spin-orbit coupling or covalent bonding may explain the anomalous peaks observed for iron and nickel, we have seen that:

- The discrepancy between experimental histograms of conductance for Fe nanocontacts and previous calculations, has been studied in detail. After exploring different contributions, from magnetic effects to electronic structure, the calculations carried out in this work indicate that the difference is related to the BCC structure and the formation of very stable contacts before rupture that are several atoms across. These structures are produced during rupture due to a transformation from (001)-oriented BCC layers to (110)-oriented ones perpendicular to the direction of stretching. Such structures give rise to a conductance value, obtained from DFT electronic transport calculations of $\sim 2 G_0$, in good agreement with experimental measurements, unlike previous calculations.
- Experimental Ni histograms of conductance also exhibit some unexplained behaviour. They can vary from one experiment to another, exhibiting in most cases a broad peak at $1.5 G_0$, while in others, which are less frequent, two peaks are observed. The presence of domain walls at the nanocontact influencing the conductance in this material had been proposed as a possible explanation for this behaviour. However, our simulations, using spin-lattice dynamics, which have been applied to these systems for the first time, show that, like in previous DFT calculations, domain walls make a very small contribution to the conductance in these systems when no external magnetic field is applied. On the other hand, our classical molecular dynamics calculations show that there is a difference in the most stable atomic structure before rupture depending on the orientation of the lattice, in particular for (111) and (001). Moreover, the spin-lattice dynamics also show a stronger influence of the presence of domain walls in the (111) than (001) orientation, although we should note that these calculations have been set up so that MR is maximised, in order to determine the maximum possible effect of DWMR. Therefore, we propose that a combination of the lattice orientation together with the influence of domain walls, to a lesser degree, could explain the variability observed experimentally, especially when (111)-oriented structures occur, since cyclic

loading in these structures lead to elongated nanocontacts and the formation of domain walls are also most favoured in them. Further studies will have to be undertaken to confirm this hypothesis.

Besides the results obtained for nanocontacts, the models developed in this thesis can be used in many other applications to study phenomena such as defects in magnetic materials, magnetic surface effects or Skyrmions, interaction among magnetised islands (quantum dots) on non-magnetic surfaces, among others.

BIBLIOGRAPHY

- [1] Joshi V K 2016 Spintronics: A contemporary review of emerging electronics devices *Int. J. Eng. Sci.* **19** 1503–13
- [2] Landman U, Barnett R N, Cleveland C L and Cheng H-P 1992 Small is different *Int. J. Mod. Phys. B* **06** 3623
- [3] Landman U and Luedtke W D 2004 Small is different: energetic, structural, thermal, and mechanical properties of passivated nanocluster assemblies *Faraday Discuss.* **125** 1–22
- [4] Yoon B, Luedtke W D, Barnett R N, Gao J, Desireddy A, Conn B E, Bigioni T and Landman U 2014 Hydrogen-bonded structure and mechanical chiral response of a silver nanoparticle superlattice *Nat. Mater.* **13** 807–11
- [5] Cheng C, McGonigal P R, Schneebeli S T, Li H, Vermeulen N A, Ke C and Stoddart J F 2015 An artificial molecular pump *Nat. Nanotechnol.* **10** 547–53
- [6] Cui L, Jeong W, Hur S, Matt M, Klöckner J C, Pauly F, Nielaba P, Cuevas J C, Meyhofer E and Reddy P 2017 Quantized thermal transport in single-atom junctions *Science (80-.).* **355** 1192–5
- [7] Agraït N, Rodrigo J G and Vieira S 1993 Conductance steps and quantization in atomic-size contacts *Phys. Rev. B* **47** 12345–8
- [8] Muller C J, van Ruitenbeek J M and de Jongh L J 1992 Conductance and supercurrent discontinuities in atomic-scale metallic constrictions of variable width *Phys. Rev. Lett.* **69** 140–3
- [9] Landman U, Luedtke W D, Burnham N A and Colton R J 1990 Atomistic mechanisms and dynamics of adhesion, nanoindentation, and fracture. *Science* **248** 454–61
- [10] Brandbyge M, Schiøtz J, Sørensen M R, Stoltze P, Jacobsen K W, Nørskov J K, Olesen L, Laegsgaard E, Stensgaard I and Besenbacher F 1995 Quantized conductance in atom-sized wires between two metals *Phys. Rev. B* **52** 8499–514
- [11] Agraït N, Yeyati A L and van Ruitenbeek J M 2003 Quantum properties of atomic-sized conductors *Phys. Rep.* **377** 81–279
- [12] Untiedt C, Rubio G, Vieira S and Agraït N 1997 Fabrication and characterization of metallic nanowires *Phys. Rev. B* **56** 2154–60
- [13] Smith J R, Bozzolo G, Banerjee A and Ferrante J 1989 Avalanche in adhesion *Phys. Rev. Lett.* **63** 1269–72

- [14] Strigl F, Espy C, Bückle M, Scheer E and Pietsch T 2015 Emerging magnetic order in platinum atomic contacts and chains. *Nat. Commun.* **6** 6172
- [15] Jacob D, Fernández-Rossier J and Palacios J J 2005 Magnetic and orbital blocking in Ni nanocontacts *Phys. Rev. B* **71** 1–4
- [16] Von Bieren A, Patra A K, Krzyk S, Rhensius J, Reeve R M, Heyderman L J, Hoffmann-Vogel R and Kläui M 2013 Domain-wall induced large magnetoresistance effects at zero applied field in ballistic nanocontacts *Phys. Rev. Lett.* **110** 1–5
- [17] Requist R, Baruselli P P, Smogunov A, Fabrizio M, Modesti S and Tosatti E 2016 Metallic, magnetic and molecular nanocontacts *Nat. Nanotechnol.* **11** 499–508
- [18] Reeve R M, Loescher A, Kazemi H, Dupé B, Mawass M-A, Winkler T, Schönke D, Miao J, Litzius K, Sedlmayr N, Schneider I, Sinova J, Eggert S and Kläui M 2019 Scaling of intrinsic domain wall magnetoresistance with confinement in electromigrated nanocontacts *Phys. Rev. B* **99** 214437
- [19] Landman U, Luedtke W D and Ringer E M 1992 Atomistic mechanisms of adhesive contact formation and interfacial processes *Wear* **153** 3–30
- [20] Pecchia A and Carlo A Di 2004 Atomistic theory of transport in organic and inorganic nanostructures *Reports Prog. Phys.* **67** 1497
- [21] Untiedt C, Caturla M J, Calvo M R, Palacios J J, Segers R C and Van Ruitenbeek J M 2007 Formation of a metallic contact: Jump to contact revisited *Phys. Rev. Lett.* **98** 206801
- [22] Kröger J, Néel N, Sperl A, Wang Y F and Berndt R 2009 Single-atom contacts with a scanning tunnelling microscope *New J. Phys.* **11** 125006
- [23] Fernández M A, Sabater C, Dednam W, Palacios J J, Calvo M R, Untiedt C and Caturla M J 2016 Dynamic bonding of metallic nanocontacts: insights from experiments and atomistic simulations *Phys. Rev. B* **93** 085437
- [24] Dednam W 2016 *Molecular Dynamics simulations of contacts between two metals at the atomic scale* (Masters dissertation, University of South Africa)
- [25] Bahn S R and Jacobsen K W 2001 Chain formation of metal atoms *Phys. Rev. Lett.* **87** 266101
- [26] Thiess A, Mokrousov Y, Blügel S and Heinze S 2008 Theory and application of chain formation in break junctions *Nano Lett.* **8** 2144–9
- [27] Thiess A, Mokrousov Y, Heinze S and Blügel S 2009 Magnetically hindered chain formation in transition-metal break junctions *Phys. Rev. Lett.* **103** 217201
- [28] Aradhya S V., Frei M, Hybertsen M S and Venkataraman L 2012 Van der Waals

- interactions at metal/organic interfaces at the single-molecule level *Nat. Mater.* **11** 872–6
- [29] Hybertsen M S 2017 Modeling single molecule junction mechanics as a probe of interface bonding *J. Chem. Phys.* **146** 092323
- [30] Vardimon R, Matt M, Nielaba P, Cuevas J C and Tal O 2016 Orbital origin of the electrical conduction in ferromagnetic atomic-size contacts: Insights from shot noise measurements and theoretical simulations *Phys. Rev. B* **93** 085439
- [31] Daw M S and Baskes M I 1983 Semiempirical, quantum mechanical calculation of hydrogen embrittlement in metals *Phys. Rev. Lett.* **50** 1285–8
- [32] Calvo M R, Caturla M J, Jacob D, Untiedt C and Palacios J J 2008 Mechanical, electrical, and magnetic properties of Ni nanocontacts *IEEE Trans. Nanotechnol.* **7** 165–8
- [33] Costa-Krämer J L 1997 Conductance quantization at room temperature in magnetic and nonmagnetic metallic nanowires *Phys. Rev. B* **55** R4875–8
- [34] Kumar M, Sethu K K V and Van Ruitenbeek J M 2015 Molecule-assisted ferromagnetic atomic chain formation *Phys. Rev. B* **91** 245404
- [35] Untiedt C, Dekker D M T, Djukic D and van Ruitenbeek J M 2004 Absence of magnetically induced fractional quantization in atomic contacts *Phys. Rev. B* **69** 081401
- [36] Calvo M R, Fernández-Rossier J, Palacios J J, Jacob D, Natelson D and Untiedt C 2009 The Kondo effect in ferromagnetic atomic contacts *Nature* **458** 1150–3
- [37] Calvo M R, Jacob D and Untiedt C 2012 Analysis of the Kondo effect in ferromagnetic atomic-sized contacts *Phys. Rev. B* **86** 075447
- [38] Vardimon R, Klionsky M and Tal O 2015 Indication of complete spin filtering in atomic-scale nickel oxide. *Nano Lett.* **15** 3894–8
- [39] Bruno P 1999 Geometrically constrained magnetic wall *Phys. Rev. Lett.* **83** 2425–8
- [40] García-Mochales P, Paredes R, Peláez S and Serena P A 2008 Statistical analysis of the breaking processes of Ni nanowires *Nanotechnology* **19**
- [41] García-Mochales P, Paredes R, Peláez S and Serena P A 2008 Statistical molecular dynamics study of (111) and (100) Ni nanocontacts: Evidences of pentagonal nanowires *J. Nanomater.* **2008** 361464
- [42] Sabater C, Caturla M J, Palacios J J and Untiedt C 2013 Understanding the structure of the first atomic contact in gold. *Nanoscale Res. Lett.* **8** 257
- [43] Malerba L, Marinica M C, Anento N, Björkas C, Nguyen H, Domain C, Djurabekova F, Olsson P, Nordlund K, Serra A, Terentyev D, Willaime F and

- Becquart C S 2010 Comparison of empirical interatomic potentials for iron applied to radiation damage studies *J. Nucl. Mater.* **406** 19–38
- [44] Zhou X W, Wadley H N G, Johnson R A, Larson D J, Tabat N, Cerezo A, Petford-Long A K, Smith G D W, Clifton P H, Martens R L and Kelly T F 2001 Atomic scale structure of sputtered metal multilayers *Acta Mater.* **49** 4005–15
- [45] Etesami S A and Asadi E 2018 Molecular dynamics for near melting temperatures simulations of metals using modified embedded-atom method *J. Phys. Chem. Solids* **112** 61–72
- [46] Ibach H 2006 *Physics of Surfaces and Interfaces* (Berlin: Springer Science & Business Media)
- [47] Sørensen M, Brandbyge M and Jacobsen K 1998 Mechanical deformation of atomic-scale metallic contacts: Structure and mechanisms *Phys. Rev. B* **57** 3283–94
- [48] Ma P-W, Woo C H and Dudarev S L 2008 Large-scale simulation of the spin-lattice dynamics in ferromagnetic iron *Phys. Rev. B* **78** 024434
- [49] Beaujouan D, Thibaudeau P and Barreteau C 2012 Anisotropic magnetic molecular dynamics of cobalt nanowires *Phys. Rev. B* **86** 174409
- [50] Tranchida J, Plimpton S J, Thibaudeau P and Thompson A P 2018 Massively parallel symplectic algorithm for coupled magnetic spin dynamics and molecular dynamics *J. Comput. Phys.* **372** 406–25
- [51] Assmann M 2009 *Atomistic simulation of spin-lattice dynamics* (Ph.D. thesis, Konstanz)
- [52] Sabiryanov R F and Jaswal S S 1999 Magnons and magnon-phonon interactions in iron *Phys. Rev. Lett.* **83** 2062
- [53] Wang H, Ma P W and Woo C H 2010 Exchange interaction function for spin-lattice coupling in bcc iron *Phys. Rev. B* **82** 1–8
- [54] Hellsvik J, Thonig D, Modin K, Iuşan D, Bergman A, Eriksson O, Bergqvist L and Delin A 2018 General method for atomistic spin-lattice dynamics with first principles accuracy *Phys. Rev. B* **99** 104302
- [55] Perera D, Eisenbach M, Nicholson D M, Stocks G M and Landau D P 2016 Reinventing atomistic magnetic simulations with spin-orbit coupling *Phys. Rev. B* **93** 060402
- [56] Eisenbach M, Perera D, Landau D P, Nicholson D M, Yin J and Brown G 2015 Magnetic materials at finite temperatures: Thermodynamics and combined spin and molecular dynamics derived from first principles calculations *J. Phys. Conf. Ser.* **640** 012019

- [57] Pakdel S, Pourfath M and Palacios J J 2018 An implementation of spin-orbit coupling for band structure calculations with Gaussian basis sets: Two-dimensional topological crystals of Sb and Bi *Beilstein J. Nanotechnol.* **9** 1015–23
- [58] Schena T 2010 *Tight-Binding Treatment of Complex Magnetic Structures in Low-Dimensional Systems* (Final year project, RWTH Aachen University)
- [59] Czerner M, Yavorsky B and Mertig I 2010 The role of noncollinear magnetic order and magnetic anisotropy for the transport properties through nanowires *Phys. Status Solidi B* **247** 2594–602
- [60] Barreateau C, Spanjaard D and Desjonquères M 2016 An efficient magnetic tight-binding method for transition metals and alloys *Comptes Rendus Phys.* **17** 406–29
- [61] Nguyen-Manh D, Ma P W, Lavrentiev M Y and Dudarev S L 2015 Constrained non-collinear magnetism in disordered Fe and Fe-Cr alloys *Ann. Nucl. Energy* **77** 246–51
- [62] Ozaki T, Kino H, Yu J, Han M J, Ohfuchi M, Ishii F, Sawada K, Kubota Y, Mizuta Y P, Ohwaki T, Duy T V T, Weng H, Shiihara Y, Toyoda M, Okuno Y, Perez R, Bell P P, Ellner M, Xiao Y, Ito A M, Kawamura M, Yoshimi K, Lee C-C and Terakura K 2017 OpenMX (Open source package for Material eXplorer) ver. 3.8 (<http://www.openmx-square.org/>) accessed: 2019-06-11
- [63] Bihlmayer G 2007 Density-functional theory of magnetism *Handbook of Magnetism and Advanced Magnetic Materials* vol 1, ed H Kronmüller and S Parkin (New Jersey: Wiley) pp 1–26
- [64] Clark S J, Segall M D, Pickard C J, Hasnip P J, Probert M I J, Refson K and Payne M C 2005 First principles methods using CASTEP *Zeitschrift für Krist. - Cryst. Mater.* **220** 567–570
- [65] Blaha P, Schwarz K, Madsen G, Kvasnicka D and Luitz J 2001 *Wien2k: An augmented plane wave+ local orbitals program for calculating crystal properties* (Karlheinz Schwarz, Techn. Universität Wien, Austria)
- [66] Takeuchi N, Chan C T and Ho K M 1989 First-principles calculations of equilibrium ground-state properties of Au and Ag *Phys. Rev. B* **40** 1565–70
- [67] Smit R H M, Untiedt C, Yanson A I and van Ruitenbeek J M 2001 Common origin for surface reconstruction and the formation of chains of metal atoms *Phys. Rev. Lett.* **87** 266102
- [68] Palacios J J, Jacob D, Soriano M, Perez-Jimenez A J, Louis E, SanFabian E and Verges J A 2000 ANT.Gaussian: Alicante atomistic computation applied to nanotransport (<https://www.simuneatomistics.com/siesta/ant/>) accessed: 2019-06-11
- [69] Chappert C, Fert A and Van Dau F N 2007 The emergence of spin electronics in

- data storage. *Nat. Mater.* **6** 813–23
- [70] Fert A, Cros V and Sampaio J 2013 Skyrmions on the track *Nat. Nanotechnol.* **8** 152–6
- [71] Goolaup S, Ramu M, Murapaka C and Lew W S 2015 Transverse domain wall profile for spin logic applications *Sci. Rep.* **5** 1–8
- [72] Agraït N, Rodrigo J G, Sirvent C and Vieira S 1993 Atomic-scale connective neck formation and characterization *Phys. Rev. B* **48** 8499–501
- [73] Hasmy A, Medina E and Serena P A 2001 From favorable atomic configurations to supershell structures: A new interpretation of conductance histograms *Phys. Rev. Lett.* **86** 5574–7
- [74] Dreher M, Pauly F, Heurich J, Cuevas J C, Scheer E and Nielaba P 2005 Structure and conductance histogram of atomic-sized Au contacts *Phys. Rev. B* **72** 075435
- [75] Pauly F, Dreher M, Viljas J K, Häfner M, Cuevas J C and Nielaba P 2006 Theoretical analysis of the conductance histograms and structural properties of Ag, Pt, and Ni nanocontacts *Phys. Rev. B* **74** 235106
- [76] Dednam W, Sabater C, Fernandez M A, Untiedt C, Palacios J J and Caturla M J 2015 Modeling contact formation between atomic-sized gold tips via molecular dynamics *J. Phys. Conf. Ser.* **574** 012045
- [77] Scheer E, Agraït N, Cuevas J C, Yeyati A L, Ludoph B, Martín-Rodero A, Bollinger G R, van Ruitenbeek J M and Urbina C 1998 The signature of chemical valence in the electrical conduction through a single-atom contact *Nature* **394** 154–7
- [78] Daw M S and Baskes M I 1984 Embedded-atom method: Derivation and application to impurities, surfaces, and other defects in metals *Phys. Rev. B* **29** 6443
- [79] Harrison J A, Schall J D, Maskey S, Mikulski P T, Knippenberg M T and Morrow B H 2018 Review of force fields and intermolecular potentials used in atomistic computational materials research *Appl. Phys. Rev.* **5** 031104
- [80] Pyykko P 1988 Relativistic effects in structural chemistry *Chem. Rev.* **88** 563–94
- [81] Ho K-M and Bohnen K P 1987 Stability of the missing-row reconstruction on fcc (110) transition-metal surfaces *Phys. Rev. Lett.* **59** 1833–6
- [82] Häkkinen H, Barnett R N, Scherbakov A G and Landman U 2000 Nanowire gold chains: Formation mechanisms and conductance *J. Phys. Chem. B* **104** 9063–6
- [83] Hasmy A, Rincón L, Hernández R, Mujica V, Márquez M and González C 2008 On the formation of suspended noble-metal monatomic chains *Phys. Rev. B* **78** 115409
- [84] Wierzbowska M, Delin A and Tosatti E 2005 Effect of electron correlations in Pd, Ni, and Co monowires *Phys. Rev. B* **72** 035439

- [85] Wadley H N G, Zhou X, Johnson R A and Neurock M 2001 Mechanisms, models and methods of vapor deposition *Prog. Mater. Sci.* **46** 329–77
- [86] Ambrosetti A and Silvestrelli P L 2016 Cohesive properties of noble metals by van der Waals-corrected density functional theory: Au, Ag, and Cu as case studies *Phys. Rev. B* **94** 045124
- [87] Tkatchenko A and Scheffler M 2009 Accurate molecular van der Waals interactions from ground-state electron density and free-atom reference data *Phys. Rev. Lett.* **102** 073005
- [88] Mokrousov Y, Bihlmayer G and Blügel S 2005 Full-potential linearized augmented plane-wave method for one-dimensional systems: Gold nanowire and iron monowires in a gold tube *Phys. Rev. B* **72** 1–15
- [89] Viret M, Berger S, Gabureac M, Ott F, Olligs D, Petej I, Gregg J F, Fermon C, Francinet G and Goff G Le 2002 Magnetoresistance through a single nickel atom *Phys. Rev. B* **66** 220401
- [90] Ruediger U, Yu J, Zhang S and Kent A D 1998 Negative domain wall contribution to the resistivity of microfabricated Fe wires *Phys. Rev. Lett.* **80** 5639–42
- [91] Oshima H and Miyano K 1998 Spin-dependent conductance quantization in nickel point contacts *Appl. Phys. Lett.* **73** 2203–5
- [92] Kronmüller H and Parkin S 2007 *Handbook of Magnetism and Advanced Magnetic Materials* (New Jersey: Wiley)
- [93] Giordano N and Monnier J D 1994 Magnetization reversal and domain wall motion in thin Ni wires *Phys. B* **194–196** 1009–10
- [94] Hong K and Giordano N 1995 Mesoscopic magnetic measurements *Phys. Rev. B* **51** 9855
- [95] Velev J, Sabirianov R F, Jaswal S S and Tsymbal E Y 2005 Ballistic anisotropic magnetoresistance. *Phys. Rev. Lett.* **94** 127203
- [96] Tataru G and Fukuyama H 1997 Resistivity due to a domain wall in ferromagnetic metal *Phys. Rev. Lett.* **78** 3773–6
- [97] Kent A D and et al. 1998 Magnetoresistance due to domain walls in micron scale Fe with stripe domains *IEEE Trans. Magn.* **34** 1–3
- [98] Otani Y, Kim S G, Fukamichi K, Kitakami O and Szymada Y 1998 Magnetic transport of sub-micron ferromagnetic wires *IEEE Trans. Magn.* **34** 1096–8
- [99] Levy P M and Zhang S 1997 Resistivity due to domain wall scattering *Phys. Rev. Lett.* **79** 5110–3
- [100] van Hoof J B A N and et al. 1999 Ballistic electron transport through magnetic

domain walls *Phys. Rev. B* **59** 138–41

- [101] García N, Muñoz M and Zhao Y-W 1999 Magnetoresistance in excess of 200 % in ballistic Ni nanocontacts at room temperature and 100 Oe *Phys. Rev. Lett.* **82** 2923–6
- [102] Egelhoff W F, Gan L, Etedgui H, Kadmon Y, Powell C J, Chen P J, Shapiro A J, McMichael R D, Mallett J J, Moffat T P, Stiles M D and Svedberg E B 2005 Artifacts that mimic ballistic magnetoresistance *J. Magn. Magn. Mater.* **287** 496–500
- [103] Tataru G, Zhao Y W, Muñoz M and García N 1999 Domain wall scattering explains 300% ballistic magnetoconductance of nanocontacts *Phys. Rev. Lett.* **83** 2030–3
- [104] Ono T, Ooka Y, Miyajima H and Otani Y 1999 $2e^2/h$ to e^2/h switching of quantum conductance associated with a change in nanoscale ferromagnetic domain structure *Appl. Phys. Lett.* **75** 1622
- [105] Komori F and Nakatsuji K 1999 Quantized conductance through atomic-sized iron contacts at 4.2 K *J. Phys. Soc. Japan* **68** 3786–9
- [106] Komori F and Nakatsuji K 2001 Quantized conductance through iron point contacts *Mater. Sci. Eng. B* **84** 102–6
- [107] Sullivan M R, Boehm D A, Ateya D A, Hua S Z and Chopra H D 2005 Ballistic magnetoresistance in nickel single-atom conductors without magnetostriction *Phys. Rev. B* **71** 1–8
- [108] Shi S-F and Ralph D C 2007 Atomic motion in ferromagnetic break junctions. *Nat. Nanotechnol.* **2** Correspondence 522-3
- [109] Chopra H D and Hua S Z 2002 Ballistic magnetoresistance over 3000% in Ni nanocontacts at room temperature *Phys. Rev. B* **66** 1–3
- [110] Elhoussine F, Mátéfi-Tempfli S, Encinas A and Piraux L 2002 Conductance quantization in magnetic nanowires electrodeposited in nanopores *Appl. Phys. Lett.* **81** 1681
- [111] Yang C-S, Zhang C, Redepenning J and Doudin B 2004 In situ magnetoresistance of Ni nanocontacts *Appl. Phys. Lett.* **84** 2865
- [112] Shu C, Li C, He H, Bogozzi A, Bunch J and Tao N 2000 Fractional conductance quantization in metallic nanoconstrictions under electrochemical potential control *Phys. Rev. Lett.* **84** 5196–9
- [113] Gillingham D M, Linington I, Müller C and Bland J A C 2003 e^2/h quantization of the conduction in Cu nanowires *J. Appl. Phys.* **93** 7388

- [114] Papanikolaou N 2003 Magnetoresistance through spin-polarized p states *J. Phys. Condens. Matter* **15** 5049
- [115] Costa-Krämer J L, Díaz M and Serena P A 2005 Magnetic field effects on total and partial conductance histograms in Cu and Ni nanowires *Appl. Phys. A* **81** 1539–43
- [116] Lepadatu S and Xu Y B 2004 Direct observation of domain wall scattering in patterned Ni₈₀Fe₂₀ and Ni nanowires by current-voltage measurements *Phys. Rev. Lett.* **92** 10–3
- [117] Bolotin K I, Kuemmeth F, Pasupathy A N and Ralph D C 2006 From ballistic transport to tunneling in electromigrated ferromagnetic breakjunctions. *Nano Lett.* **6** 123–7
- [118] Autès G, Barreteau C, Desjonquères M C, Spanjaard D and Viret M 2008 Giant orbital moments are responsible for the anisotropic magnetoresistance of atomic contacts *EPL* **83** 17010
- [119] Czerner M, Yavorsky B Y, Mertig I, Czerner M, Yavorsky Y and Mertig I 2008 Magnetic order in geometrically constrained domain walls *J. Appl. Phys.* **103** 07F304
- [120] Achilles S, Czerner M and Mertig I 2011 Tailoring magnetoresistance through rotating Ni particles *Phys. Rev. B* **84** 1–9
- [121] Hardrat B, Freimuth F, Heinze S and Mokrousov Y 2012 Conductance fingerprints of noncollinear magnetic states in single-atom contacts: A first-principles Wannier-functions study *Phys. Rev. B* **86** 165449
- [122] Imamura H, Kobayashi N, Takahashi S and Maekawa S 2000 Conductance quantization and magnetoresistance in magnetic point contacts *Phys. Rev. Lett.* **84** 1003–6
- [123] Bagrets A, Papanikolaou N and Mertig I 2004 Magnetoresistance of atomic-sized contacts: An ab initio study *Phys. Rev. B* **70** 064410
- [124] Jacob D 2007 *Spin transport in nanocontacts and nanowires* (Ph.D. thesis, University of Alicante)
- [125] Smogunov A, Dal Corso A and Tosatti E 2004 Ballistic conductance of magnetic Co and Ni nanowires with ultrasoft pseudopotentials *Phys. Rev. B* **70** 045417
- [126] Smogunov A, Dal Corso A and Tosatti E 2006 Ballistic conductance and magnetism in short tip suspended Ni nanowires *Phys. Rev. B* **73** 075418
- [127] Smogunov A, Dal Corso A and Tosatti E 2008 Magnetic phenomena, spin-orbit effects, and Landauer conductance in Pt nanowire contacts: Density-functional theory calculations *Phys. Rev. B* **78** 014423

- [128] Li G D, Zhai Y, Wong P K J, Niu D X, Lu Y X, Lepadatu S and Xu Y B 2007 Magnetic domain wall formation in ferromagnetic wires with a nanoconstriction *IEEE Trans. Magn.* **43** 2830–2
- [129] Untiedt C, Yanson A I, Grande R, Rubio-Bollinger G, Agraït N, Vieira S and van Ruitenbeek J M 2002 Calibration of the length of a chain of single gold atoms *Phys. Rev. B* **66** 085418
- [130] Sabater C, Untiedt C, Palacios J J and Caturla M J 2012 Mechanical annealing of metallic electrodes at the atomic scale *Phys. Rev. Lett.* **108** 205502
- [131] Jacob D and Palacios J J 2006 Orbital eigenchannel analysis for ab-initio quantum transport calculations *Phys. Rev. B* **73** 075429
- [132] Labaye Y, Berger L and Coey J M D 2002 Domain walls in ferromagnetic nanoconstriction *J. Appl. Phys.* **91** 5341–6
- [133] Kazantseva N, Wieser R and Nowak U 2005 Transition to linear domain walls in nanoconstrictions *Phys. Rev. Lett.* **94** 037206
- [134] Ma P-W, Dudarev S L and Woo C H 2016 SPILADY: A parallel CPU and GPU code for spin–lattice magnetic molecular dynamics simulations *Comput. Phys. Commun.* **207** 350–61
- [135] Inoue J I 2013 GMR, TMR, BMR, and Related Phenomena *Nanomagnetism and Spintronics: Second Edition* (Amsterdam: Elsevier B.V.) pp 15–106
- [136] Doudin B and Viret M 2008 Ballistic magnetoresistance? *J. Phys. Condens. Matter* **20** 083201
- [137] Wang H and Leng Y 2011 Molecular dynamics simulations of the stable structures of single atomic contacts in gold nanojunctions *Phys. Rev. B* **84** 245422
- [138] Baskes M I 1992 Modified embedded-atom potentials for cubic materials and impurities *Phys. Rev. B* **46** 2727–42
- [139] Huang D, Zhang Q and Qiao P 2011 Molecular dynamics evaluation of strain rate and size effects on mechanical properties of FCC nickel nanowires *Comput. Mater. Sci.* **50** 903–10
- [140] Muralles M, Choi D and Lee B 2017 A comparative study of mechanical properties of Ni <001> nanowires from atomistic calculations *J. Mech. Sci. Technol.* **31** 4887–93
- [141] Soldano G and Mariscal M M 2009 On the structural and mechanical properties of Fe-filled carbon nanotubes - A computer simulation approach *Nanotechnology* **20** 165705
- [142] Munizaga V, García G, Bringa E, Weissmann M, Ramírez R and Kiwi M 2014

- Atomistic simulation of soldering iron filled carbon nanotubes *Comput. Mater. Sci.* **92** 457–63
- [143] Munizaga V, Ramírez R, Kiwi M and García G 2017 Mechanical properties of iron filled carbon nanotubes: Numerical simulations *J. Appl. Phys.* **121**
- [144] Calvo M R 2009 *Structure, magnetism and transport in atomic contacts* (Ph.D. thesis, University of Alicante)
- [145] García N, Muñoz M and Zhao Y W 2000 Ballistic magnetoresistance in transition-metal nanocontacts: The case of iron *Appl. Phys. Lett.* **76** 2586–7
- [146] Frenkel D and Smit B 2002 *Understanding Molecular Simulation: From Algorithms to Applications (Second Edition)* (San Diego: Academic Press)
- [147] Kohn W and Sham L J 1965 Self-Consistent equations including exchange and correlation effects *Phys. Rev.* **140** A1133–8
- [148] Kadanoff L P and Baym G 1962 *Quantum Statistical Mechanics: Green's Function Methods in Equilibrium and Nonequilibrium Problems* ed D Pines (New York: W. A. Benjamin, INC.)
- [149] Keldysh L V 1964 Diagram technique for nonequilibrium processes *J. Exp. Theor. Phys.* **20** 1018
- [150] Rapaport D C 2004 *The Art of Molecular Dynamics Simulation* (New York: Cambridge University Press)
- [151] van Duin A C T, Dasgupta S, Lorant F and Goddard III W A 2001 ReaxFF: A reactive force field for hydrocarbons *J. Phys. Chem. A* **105** 9396–409
- [152] Daw M S, Foiles S M and Baskes M I 1993 The embedded-atom method: a review of theory and applications *Mater. Sci. Reports* **9** 251–310
- [153] Dudarev S L and Derlet P M 2005 A ‘magnetic’ interatomic potential for molecular dynamics simulations *J. Phys. Condens. Matter* **17** 7097–118
- [154] Derlet P and Dudarev S L 2007 Million-atom molecular dynamics simulations of magnetic iron *Prog. Mater. Sci.* **52** 299–318
- [155] Stoner E C 1938 Collective electron ferromagnetism *Proc. R. Soc. A Math. Phys. Eng. Sci.* **165** 372–414
- [156] Ruban A V., Khmelevskiy S, Mohn P and Johansson B 2007 Temperature-induced longitudinal spin fluctuations in Fe and Ni *Phys. Rev. B* **75** 1–7
- [157] Körmann F, Grabowski B, Dutta B, Hickel T, Mauger L, Fultz B and Neugebauer J 2014 Temperature dependent magnon-phonon coupling in bcc Fe from theory and experiment *Phys. Rev. Lett.* **113** 165503

- [158] Körmann F, Ma P W, Dudarev S L and Neugebauer J 2016 Impact of magnetic fluctuations on lattice excitations in fcc nickel *J. Phys. Condens. Matter* **28** 076002
- [159] Liechtenstein A I, Katsnelson M I and Gubanov V A 1984 Exchange interactions and spin-wave stiffness in ferromagnetic metals *J. Phys. F Met. Phys.* **14** 3–7
- [160] Liechtenstein A I, Katsnelson M I, Antropov V . and Gubanov V A 1987 Local spin density functional approach to exchange interactions in ferromagnetic metals and alloys *J. Magn. Magn. Mater.* **67** 65–74
- [161] Kvashnin Y O, Grånäs O, Di Marco I, Katsnelson M I, Lichtenstein A I and Eriksson O 2015 Exchange parameters of strongly correlated materials: Extraction from spin-polarized density functional theory plus dynamical mean-field theory *Phys. Rev. B* **91** 1–10
- [162] Morán S, Ederer C and Fähnle M 2003 Ab initio electron theory for magnetism in Fe: Pressure dependence of spin-wave energies, exchange parameters, and Curie temperature *Phys. Rev. B* **67** 012407
- [163] Richardson O W 1908 A mechanical effect accompanying magnetization *Phys. Rev. (Series I)* **26** 248
- [164] Wen H, Ma P W and Woo C H 2013 Spin-lattice dynamics study of vacancy formation and migration in ferromagnetic BCC iron *J. Nucl. Mater.* **440** 428–34
- [165] Ma P-W and Dudarev S L 2011 Langevin spin dynamics *Phys. Rev. B* **83** 134418
- [166] Ma P-W and Woo C H 2009 Parallel algorithm for spin and spin-lattice dynamics simulations *Phys. Rev. E* **79** 046703
- [167] Krech M, Bunker A and Landau D P 1998 Fast spin dynamics algorithms for classical spin systems *Comput. Phys. Commun.* **111** 1–13
- [168] Landau D P, Shan-Ho T, Krech M and Bunker A 1999 Improved spin dynamics simulations of magnetic excitations *Int. J. Mod. Phys. C* **10** 1541–51
- [169] Plimpton S, Thompson A, Crozier P and Kohlmeyer A LAMMPS: Large-scale Atomic/Molecular Massively Parallel Simulator (<http://lammps.sandia.gov/index.html>) accessed: 2019-06-11
- [170] Kohn W 2002 Nobel Lecture: Electronic structure of matter—wave functions and density functionals *Rev. Mod. Phys.* **71** 1253–66
- [171] Cramer C J and Truhlar D G 2009 Density functional theory for transition metals and transition metal chemistry *Phys. Chem. Chem. Phys.* **11** 10757
- [172] Lejaeghere K, Van Speybroeck V, Van Oost G and Cottenier S 2014 Error estimates for solid-state density-functional theory predictions: An overview by means of the ground-state elemental crystals *Crit. Rev. Solid State Mater. Sci.* **39** 1–

- [173] Dovesi R, Orlando R, Erba A, Zicovich-Wilson C M, Civalieri B, Casassa S, Maschio L, Ferrabone M, De La Pierre M, D'Arco P, Noël Y, Causà M, Rérat M and Kirtman B 2014 CRYSTAL14: A program for the ab initio investigation of crystalline solids *Int. J. Quantum Chem.* **114** 1287–317
- [174] Ozaki T 2003 Variationally optimized atomic orbitals for large-scale electronic structures *Phys. Rev. B* **67** 155108
- [175] Ozaki T and Kino H 2004 Numerical atomic basis orbitals from H to Kr *Phys. Rev. B* **69** 195113
- [176] Zotti L A and Pérez R 2017 Platinum atomic contacts: From tunneling to contact *Phys. Rev. B* **95** 1–7
- [177] Frisch M J and et al. 2009 Gaussian 09 revision C.1, Gaussian Inc.. Wallingford, CT
- [178] Vanderbilt D 1990 Soft self-consistent pseudopotentials in a generalized eigenvalue formalism *Phys. Rev. B* **41** 7892–5
- [179] Haas P, Tran F and Blaha P 2009 Erratum: Calculation of the lattice constant of solids with semilocal functionals [Phys. Rev. B 79 , 085104 (2009)] *Phys. Rev. B* **79** 209902
- [180] Jacob D and Palacios J J 2011 Critical comparison of electrode models in density functional theory based quantum transport calculations *J. Chem. Phys.* **134** 044118
- [181] Joon Choi H and Ihm J 1999 Ab initio pseudopotential method for the calculation of conductance in quantum wires *Phys. Rev. B* **59** 2267–75
- [182] Giannozzi P and et al. 2009 Quantum ESPRESSO: a modular and open-source software project for quantum simulations of materials *J. Phys. Condens. Matter* **21** 395502
- [183] Datta S 2000 Nanoscale device modeling: the Green's function method *Superlattices Microstruct.* **28** 253–78
- [184] Ozaki T, Nishio K and Kino H 2010 Efficient implementation of the nonequilibrium Green function method for electronic transport calculations *Phys. Rev. B* **81** 035116
- [185] Merzbacher E 1998 *Quantum Mechanics (Third Edition)* (New York: Wiley)
- [186] Cuevas J C and Scheer E 2010 *Molecular Electronics* (Singapore: World Scientific)
- [187] Palacios J J, Pérez-Jiménez A J, Louis E and Vergés J A 2001 Fullerene-based molecular nanobridges: A first-principles study *Phys. Rev. B* **64** 115411

- [188] Palacios J J, Perez-Jimenez A J, Louis E, SanFabian E and Verges J A 2002 A first-principles approach to electrical transport in atomic-scale nanostructures *Phys. Rev. B* **66** 035322
- [189] Papaconstantopoulos D A and Mehl M J 2003 The Slater Koster tight-binding method: a computationally efficient and accurate approach *J. Phys. Condens. Matter* **15** R413–40
- [190] Landauer R 1970 Electrical resistance of disordered one-dimensional lattices *Philos. Mag.* **21** 863–7
- [191] Louis E, Vergés J A, Palacios J J, Pérez-Jiménez A J and SanFabián E 2003 Implementing the Keldysh formalism into ab initio methods for the calculation of quantum transport: Application to metallic nanocontacts *Phys. Rev. B* **67** 155321
- [192] Dednam W, Sabater C, Fernandez M A, Untiedt C, Palacios J J and Caturla M J 2016 Simulating cyclic loading of atomic-sized gold tips on gold surfaces via classical molecular dynamics and density functional theory transport calculations *Proceedings of the 60th annual conference of the South African Institute of Physics (SAIP)* (Port Elizabeth) pp 487–92
- [193] Bratkovsky A M, Sutton A P and Todorov T N 1995 Conditions for conductance quantization in realistic models of atomic-scale metallic contacts *Phys. Rev. B* **52** 5036–51
- [194] Perera D 2015 *Atomistic simulations of magnetic models with coupled translational and spin degrees of freedom* (Ph.D. thesis, University of Georgia)
- [195] Cullity B D and Graham C D 2009 *Introduction to magnetic materials* (New Jersey: Wiley)
- [196] Nurdin W B and Schotte K D 2000 Dynamical temperature for spin systems *Phys. Rev. E* **61** 3579–89
- [197] Garcin T, Rivoirard S, Elgoyhen C and Beaunon E 2010 Experimental evidence and thermodynamics analysis of high magnetic field effects on the austenite to ferrite transformation temperature in Fe–C–Mn alloys *Acta Mater.* **58** 2026–32
- [198] Perera D, Landau D P, Nicholson D M, Malcolm Stocks G, Eisenbach M, Yin J and Brown G 2014 Phonon-magnon interactions in body centered cubic iron: A combined molecular and spin dynamics study *J. Appl. Phys.* **115** 17D124
- [199] Autès G, Barreateau C, Spanjaard D and Desjonquères M C 2006 Magnetism of iron: From the bulk to the monatomic wire *J. Phys. Condens. Matter* **18** 6785–813
- [200] Desjonquères M C, Barreateau C, Autès G and Spanjaard D 2007 Orbital contribution to the magnetic properties of iron as a function of dimensionality *Phys. Rev. B* **76** 1–12

- [201] Soler J M, Artacho E, Gale J D, García A, Junquera J, Ordejón P and Sánchez-Portal D 2002 The SIESTA method for ab initio order-N materials simulation *J. Phys. Condens. Matter* **14** 2745–79
- [202] Ma P-W and Dudarev S L 2015 Constrained density functional for noncollinear magnetism *Phys. Rev. B* **91** 054420
- [203] Sabater C, Gosálbez-Martínez D, Fernández-Rossier J, Rodrigo J G, Untiedt C and Palacios J J 2013 Topologically protected quantum transport in locally exfoliated bismuth at room temperature *Phys. Rev. Lett.* **110** 1–5
- [204] Ross R B, Powers J M, Atashroo T, Ermler W C, LaJohn L A and Christiansen P A 1990 Ab initio relativistic effective potentials with spin-orbit operators. IV. Cs through Rn *J. Chem. Phys.* **93** 6654
- [205] Fernández-Rossier J, Jacob D, Untiedt C and Palacios J J 2005 Transport in magnetically ordered Pt nanocontacts *Phys. Rev. B* **72** 224418
- [206] Peterson K A, Figgen D, Goll E, Stoll H and Dolg M 2003 Systematically convergent basis sets with relativistic pseudopotentials. II. Small-core pseudopotentials and correlation consistent basis sets for the post-d group 16-18 elements *J. Chem. Phys.* **119** 11113–23
- [207] Canal Neto A and Jorge F E 2013 All-electron double zeta basis sets for the most fifth-row atoms: Application in DFT spectroscopic constant calculations *Chem. Phys. Lett.* **582** 158–62
- [208] Doll K 2003 Density functional study of Ni bulk, surfaces and the adsorbate systems Ni(1 1 1)(3×3)R30°-Cl, and Ni(1 1 1)(2 × 2)-K *Surf. Sci.* **544** 103–20
- [209] Sander D, Skomski R, Schmidhals C, Enders A and Kirschner J 1996 Film stress and domain wall pinning in sesquilayer iron films on W(110) *Phys. Rev. Lett.* **77** 2566–9
- [210] Kröger J, Néel N and Limot L 2008 Contact to single atoms and molecules with the tip of a scanning tunnelling microscope *J. Phys. Condens. Matter* **20** 223001
- [211] Néel N, Kröger J, Limot L and Berndt R 2006 Conductance of single atoms and molecules studied with a scanning tunnelling microscope *Nanotechnology* **18** 044027
- [212] Nosé S 2006 A molecular dynamics method for simulations in the canonical ensemble *Mol. Phys.* **52** 255–68
- [213] Hoover W 1985 Canonical dynamics: Equilibrium phase-space distributions *Phys. Rev. A* **31** 1695–7
- [214] Swope W C 1982 A computer simulation method for the calculation of equilibrium constants for the formation of physical clusters of molecules: Application to small

- water clusters *J. Chem. Phys.* **76** 637
- [215] Verlet L 1967 Computer “experiments” on classical fluids. I. Thermodynamical properties of Lennard-Jones molecules *Phys. Rev.* **159** 98–103
- [216] Koelling D D and Harmon B N 1977 A technique for relativistic spin-polarised calculations *J. Phys. C Solid State Phys.* **10** 3107–14
- [217] Barzilai J and Borwein J M 1988 Two-point step size gradient methods *IMA J. Numer. Anal.* **8** 141–8
- [218] Perdew J P, Burke K and Ernzerhof M 1996 Generalized gradient approximation made simple *Phys. Rev. Lett.* **77** 3865–8